

# University of St Andrews



Full metadata for this thesis is available in  
St Andrews Research Repository  
at:

<http://research-repository.st-andrews.ac.uk/>

This thesis is protected by original copyright

V  
85

**A NUCLEAR MAGNETIC RESONANCE  
STUDY OF THE  
HIGH TEMPERATURE SUPERCONDUCTOR  
(Tl<sub>0.5</sub>Pb<sub>0.5</sub>)Sr<sub>2</sub>(Ca<sub>1-y</sub>Y<sub>y</sub>)Cu<sub>2</sub>O<sub>7-δ</sub> SYSTEM**



A thesis presented  
by  
**Guangping Dai**  
to  
The University of St. Andrews  
in Application for the  
**Degree of Doctor of Philosophy**

January 1994

TR B554

*This thesis is dedicated to my wife*

*YHI YAN*



## **Career**

I first matriculated in Physics Department of Xuzhou Normal University, P.R. China, in September 1982. In July 1986, I graduated with a degree of Bachelor of Science in Physics. In the following three years, I was appointed as an assistant lecturer at the same department.

In December 1989, following the ORS (Oversea Research Student) Award and the University Scholarship, I was enrolled as a research student reading for the degree of Doctor of Philosophy under the resolution of the University Court, 1967, No. 1.

## **Declaration**

I, Guangping Dai, hereby certify that this thesis has been composed by myself, that it is a record of my own work and that it has not been accepted in partial or complete fulfilment of any other degree or professional qualification.

In submitting this thesis to the University of St Andrews, I understand that I am giving permission for it to be made available for use in accordance with the regulations of the university library for the time being enforced, subject to any copyright vested in the work not being affected thereby. I also understand that the title and abstract will be published, and that a copy of the work may be made and supplied to any bona fide library or research worker.

9.6.94

## **Certificate**

I hereby certify that Guangping Dai has spent nine terms undertaking research work in the J. F. Allen Physical Sciences Laboratory of St Salvator's College, at the University of St Andrews, under my direction. He has fulfilled the conditions of Ordinance No. 16 (St Andrews) and he is qualified to submit the following thesis in application for the degree of Doctor of Philosophy.

Dr D.P.Tunstall  
Research Supervisor

## **Acknowledgements**

First of all, I would like to thank my supervisor Dr. David P. Tunstall for his invaluable insights, experience and guidance throughout this research and to the technical and academic staff of the Department of Physics and Astronomy for providing the excellent facilities.

I would like to thank Dr. Ru-Shi Liu and Professor Peter P. Edwards for supplying the samples and information about the samples.

I wish to thank the committee of Vice-Chancellors and Principals of the Universities of the United Kingdom for an ORS Award and the University of St. Andrews for a University Scholarship. Their financial support enabled me to undertake the work for this project.

I am indebted to my colleagues, especially to Dr. Wendy J. Webster, Dr. Philip Mason, Dr. Sam Arumugam for their assistance and helpful discussions and wish to extend my appreciation to Heather Booth, Geoff Stockham, and Bernd Ctortecka. I also wish to thank Angus Calder and Donald Herd (Department of Geology) for their assistance with the X-ray diffraction measurements and scanning electron microscopy, respectively.

Finally, I must give my hearty thanks to my wife for her understanding, encouragement and love.

## Abstract

This study reports measurements of nuclear magnetic resonance (NMR) in the  $(\text{Tl}_{0.5}\text{Pb}_{0.5})\text{Sr}_2(\text{Y}_y\text{Ca}_{1-y})\text{Cu}_2\text{O}_{7-\delta}$  system as a function of  $y$ , the yttrium concentration, over the stoichiometry range encompassing the metal-superconductor-(antiferromagnetic) semiconductor transition. The powder samples were partially aligned, and the measurements included a systematic study of yttrium-89 shifts, and some relaxation data, in the temperature range 160 K to 300 K, room temperature copper-63 NMR and NQR and lead-207 NMR, as well as thallium NMR at 1.5 K. We have also carried out AC susceptibility and X-ray measurements to provide information on the electric structure, phase purity and degree of alignment of the cuprates.

We report  $^{63}\text{Cu}$  NMR spin echo experiments on both random and partially aligned powder samples. We establish a deconvoluting method in which the random fraction is subtracted from the partially aligned spectra. We then obtain the Knight shift components as well as the quadrupole resonance frequency as functions of yttrium concentration by using a theory to fit the experimental data.

Through yttrium NMR measurements, we learn that the yttrium is coupled more weakly to the copper oxide planes in this system than it is in YBCO. Thallium resonance measurements provide some demagnetization and penetration depth information. Correlations between the  $^{89}\text{Y}$ ,  $^{207}\text{Pb}$  and  $^{63}\text{Cu}$  Knight shifts provide strong evidence in favour of a single quantum spin fluid (one component model). Finally, we develop a model of local defects associated with the yttrium doping to explain the reduction of the observability of copper, lead and thallium resonances.

## Table of Contents

<b>Chapter 1 Introduction</b> .....	<b>1</b>
§ 1.1 Historical Superconductivity.....	1
§ 1.2 Introduction to High Temperature Superconductivity.....	7
§ 1.3 Introduction to Nuclear Magnetic Resonance.....	14
§ 1.4 Outline of This Work.....	16
References.....	17
<b>Chapter 2 The Nuclear Magnetic Resonance</b> .....	<b>20</b>
§ 2.1 Introduction.....	20
§ 2.2 The Nuclear Spins.....	20
§ 2.3 The Basic Theory of Nuclear Resonance.....	21
§ 2.4 The Nuclear Interactions.....	22
§ 2.4.1 The Nuclear Magnetic Dipole Interaction.....	23
§ 2.4.2 The Nuclear Spin Interaction With Closed Shell Electron Orbits.....	24
§ 2.4.3 The Interaction Between Nucleus and Conduction Electron.....	25
§ 2.4.4 The Exchange Interaction.....	26
§ 2.4.5 The Quadrupole Interaction.....	26
§ 2.4.5.1 The First-order Quadrupole Effects.....	28
§ 2.4.5.2 The Second-order Quadrupole Effects.....	29
§ 2.5 The Knight Shift.....	30
§ 2.5.1 Introduction.....	30
§ 2.5.2 Knight Shift in Normal State.....	31
§ 2.5.3 Orientation Dependence of Knight Shift.....	32

§ 2.5.4 Knight Shift and Quadrupole Effects Present Simultaneously .....	34
§ 2.5.5 Knight Shift in Superconducting State.....	36
§ 2.6 NMR in Type-II Superconductors.....	37
§ 2.7 Nuclear Relaxation.....	38
§ 2.7.1 Spin-lattice Relaxation .....	38
§ 2.7.2 Spin-Spin relaxation ( T2 ).....	40
References.....	41

### **Chapter 3 Experimental Techniques .....43**

§ 3.1 Introduction .....	43
§ 3.2 Pulsed NMR and Fourier Transform.....	43
§ 3.2.1 Introduction .....	43
§ 3.2.2 Introduction to Fourier Transform (FT) .....	46
§ 3.2.3 The Spin Echo Technique .....	47
§ 3.3 The NMR Spectrometer.....	48
§ 3.3.1 General Spectrometer .....	48
§ 3.3.2 The Bruker MSL-500 spectrometer .....	50
§ 3.3.3 The Low Temperature Spectrometer .....	51
§ 3.4 NMR and NQR Measurements.....	51
§ 3.4.1 Yttrium-89 NMR .....	51
§ 3.4.1.1 Magnetic Shift Measurement .....	51
§ 3.4.1.2 Spin-lattice Relaxation Time (T1) Measurements.....	52
§ 3.4.2 Copper-63 and Lead-207 NMR and Copper-63 NQR.....	53
§ 3.4.2.1 Frequency Spectra Measurements .....	53
§ 3.4.2.2 T1 Measurements .....	55
§ 3.4.2.3 T2 Measurements .....	55
§ 3.4.2.4 Difference Between NMR and NQR Measurements.....	56
§ 3.4.3 Thallium NMR Measurements .....	57
§ 3.5 Sample Preparation and Alignment Procedure .....	57

§ 3.6	Characterisation of Alignment by X-ray Diffraction.....	58
§ 3.7	A.C. Susceptibility Measurements .....	59
§ 3.7.1	A.C. Susceptibility Measurements .....	59
§ 3.7.2	Temperature Controller and Measurement.....	60
	References.....	63
<b>Chapter 4</b>	<b>The <math>(\text{Tl}_{0.5}\text{Pb}_{0.5})\text{Sr}_2(\text{Y}_y\text{Ca}_{1-y})\text{Cu}_2\text{O}_{7-\delta}</math> System.....</b>	<b>64</b>
§ 4.1	Introduction .....	64
§ 4.2	Introduction to the Tl-1212 System.....	64
§ 4.2.1	General Introduction .....	64
§ 4.2.2	Metal-Superconductor-Insulator Transition in $(\text{Tl}_{1-x}\text{Pb}_x)\text{Sr}_2(\text{Y}_y\text{Ca}_{1-y})\text{Cu}_2\text{O}_{7-\delta}$ system.....	65
§ 4.3	The Structure of $(\text{Tl}_{0.5}\text{Pb}_{0.5})\text{Sr}_2(\text{Y}_y\text{Ca}_{1-y})\text{Cu}_2\text{O}_{7-\delta}$ .....	66
§ 4.4	Physical Properties of $(\text{Tl}_{0.5}\text{Pb}_{0.5})\text{Sr}_2(\text{Y}_y\text{Ca}_{1-y})\text{Cu}_2\text{O}_{7-\delta}$ .....	74
§ 4.4.1	Resistivity .....	74
§ 4.4.2	Meissner Effect .....	74
§ 4.4.3	Hall Effect.....	77
	References.....	79
<b>Chapter 5</b>	<b>Experimental Results.....</b>	<b>82</b>
§ 5.1	Alignment.....	82
§ 5.2	A.C. Susceptibility .....	89
§ 5.3	Thallium NMR at 1.5 K.....	94
§ 5.4	Yttrium-89 NMR.....	97
§ 5.5	Copper NMR and NQR.....	105
§ 5.5.1	NMR on CAY* Series .....	105
§ 5.5.2	NMR on NCA Y* Series.....	105
§ 5.5.3	$T_1$ and $T_2$ of Cu NMR.....	107

§ 5.5.4 Copper NQR .....	108
§ 5.6 Lead NMR .....	109
§ 5.6.1 NMR Spectra.....	109
§ 5.6.2 $T_1$ and $T_2$ of Lead NMR.....	110
References.....	125
<b>Chapter 6 Data Analysis &amp; Discussion.....</b>	<b>126</b>
§ 6.1 Introduction .....	126
§ 6.2 Alignment.....	126
§ 6.3 Thallium NMR .....	128
§ 6.4 Yttrium NMR.....	130
§ 6.5 Analysis of The Copper NMR Results .....	134
§ 6.5.1 Theoretical Curve Fitting .....	134
§ 6.5.2 Knight Shift Components .....	140
§ 6.5.3 Quadrupole Coupling Constant .....	144
§ 6.5.4 Checking the deconvoluting Method on $YBa_2Cu_3O_{7-\delta}$ .....	144
§ 6.5.5 A Comparison Between TI-1212 System and YBCO System.....	147
§ 6.5.6 Conclusions.....	148
§ 6.6 The Valence State of Lead.....	149
§ 6.7 One Component Model .....	151
§ 6.8 Spin-spin Relaxation time $T_2$ .....	154
§ 6.9 Defect Model.....	156
References.....	159
<b>Chapter 7 Conclusions.....</b>	<b>163</b>
§ 7.1 Summary and Conclusions .....	163
§ 7.2 Suggestions for Further Work.....	169

# Chapter 1

## Introduction

### § 1.1 Historical Superconductivity

Superconductivity was first discovered by Kamerlingh Onnes<sup>1</sup> in 1911, just three years after he had successfully liquefied helium. He found that the electrical resistance of mercury disappeared completely when it is cooled below 4.2K, (the boiling point of liquid helium at atmospheric pressure.)

Subsequently, a number of other metals such as lead, tin etc., were discovered also to be superconducting when they were cooled down to a transition (critical) temperature,  $T_c$  characteristic of the material.

Superconductivity was thought of as perfect conductivity, consisting only of a vanishing of all electrical resistance below  $T_c$ , until the discovery of the Meissner effect in 1933. Meissner and Ochsenfeld<sup>2</sup> found that a superconductor is a perfect diamagnet; magnetic flux is excluded from all but a thin penetration region near the surface. Two years later (1935), based on the "two fluid model", (namely; the conduction electrons (below  $T_c$ ) separate into two groups, with some behaving as superfluid electrons, *i.e.* such electrons pass through the superconductor without resistance, the rest of conduction electrons still retaining the normal conduction electron's behaviour), the brothers F. and H. London<sup>3</sup> proposed a phenomenological theoretical basis of the

electrodynamics properties. Pippard<sup>4</sup> modified the London equations, introducing a coherence distance,  $\xi_0$ ,

$$\xi_0 = a \frac{\hbar v_f}{kT_c} \quad (1.1)$$

where  $v_f$  is the Fermi velocity,  $a$  is a numerical constant.

In 1950, Ginzburg and Landau<sup>5</sup> proposed a different phenomenological theory, in which they had introduced a complex pseudowave function  $\Psi$  as an order parameter for the superconducting electrons. Therefore the local density of superconducting electrons was given by  $|\Psi|^2$ . They then derived a differential equation for  $\Psi$ , which is very analogous to the Schrodinger equation for a free particle, but with a nonlinear term<sup>6</sup>. In the GL theory, they had also introduced a temperature dependent coherence length,  $\xi_{GL}(T)$ , and the GL parameter,  $\kappa$ . The GL coherence length  $\xi_{GL}(T)$ , is related to, but distinct from, the Pippard coherence length,  $\xi_0$ . In a pure superconductor, *i.e.*  $T \ll T_c$ ,  $\xi_{GL}(T) \approx \xi_0$ . Near  $T_c$  however,  $\xi_{GL}(T)$  diverges as  $(T_c - T)^{-1/2}$ . The GL parameter  $\kappa$  is defined as

$$\kappa = \frac{\lambda(T)}{\xi_{GL}(T)} \quad (1.2)$$

where  $\lambda(T)$  is the penetration depth, since  $\lambda(T)$  and  $\xi_{GL}(T)$  diverge in the same way at  $T_c$ ,  $\kappa$  is a dimensionless ratio and approximately independent of temperature.

In 1957, Abrikosov<sup>7</sup> published a remarkably significant paper, in which he used the GL parameter  $\kappa$  to classify superconductors into two types:

$$\kappa = \frac{\lambda(T)}{\xi_{GL}(T)} \begin{cases} < \frac{1}{\sqrt{2}} & \text{type I} \\ > \frac{1}{\sqrt{2}} & \text{type II} \end{cases} \quad (1.3)$$

In type I superconductors, superconductivity can be destroyed by either a large enough magnetic field  $H > H_c$ , called a critical magnetic field, or a large enough current density  $J > J_c$ , called a critical current density. Figure 1.1 shows the relations between  $T_c$ ,  $H_c$ ,  $J_c$ . In type II superconductors, there is a continuous increase in flux penetration, starting at a first critical field  $H_{c1}$  and reaching  $B \approx H$  at a second critical field  $H_{c2}$ , as shown schematically in Figure 1.2 and Figure 1.3.

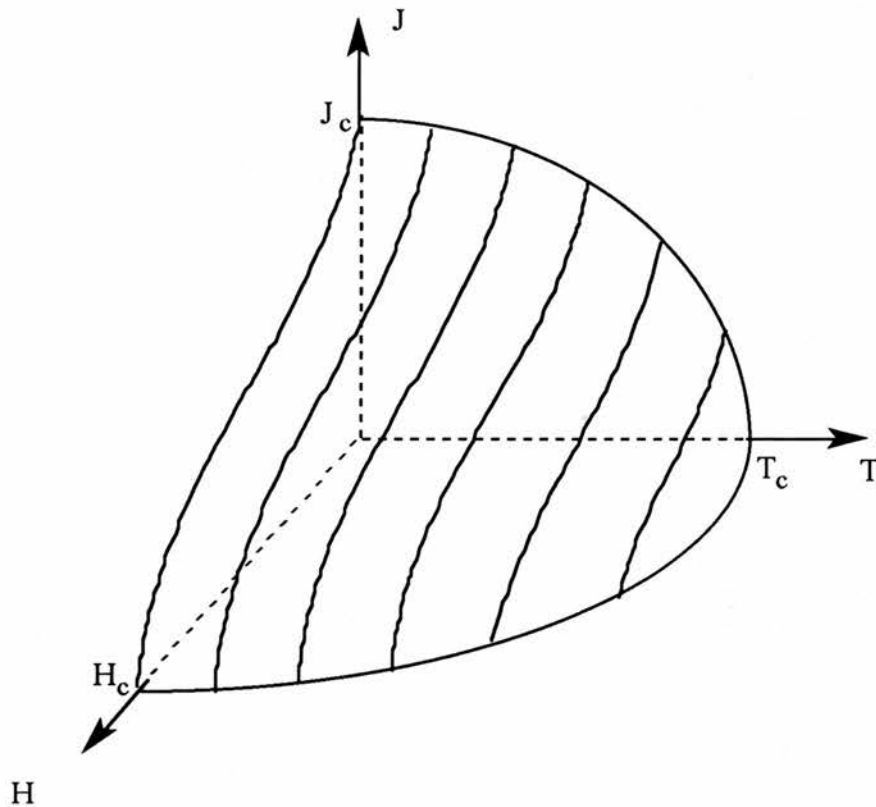


Figure 1.1 The critical surface separates normal from superconducting states in type I materials.

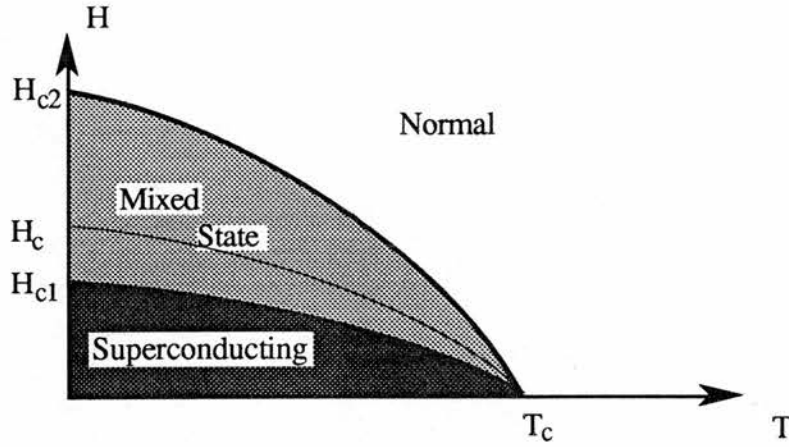


Figure 1.2 Flux penetration occurs in the mixed state in Type II superconductors. Below  $H_{c1}$  the material is superconducting and above  $H_{c2}$  it is in the normal state.

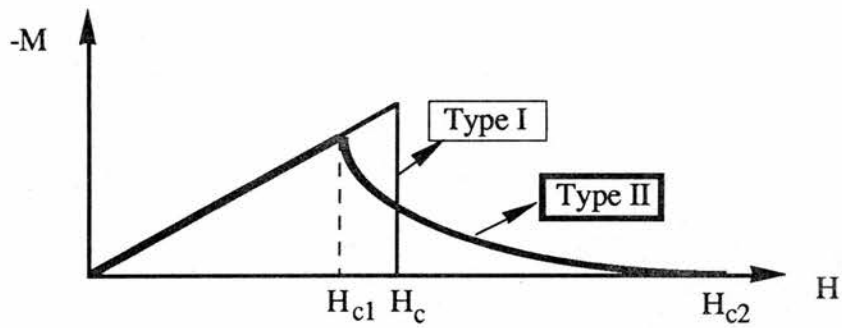


Figure 1.3 Comparison of magnetization curves for the Type I and Type II superconductors.

In the same year (1957), the microscopic theory of superconductivity was established by Bardeen, Cooper and Schrieffer.<sup>8</sup> It is one of the most famous theories, and is now called BCS theory. Before the BCS theory was published, Frohlich<sup>9</sup> had suggested that the interaction between electrons and lattice vibrations, or phonons, could lead to an effective interaction between the electrons themselves.

In BCS theory, it was shown that even a weak attractive interaction between electrons, via the lattice, could cause an instability of the ordinary Fermi-sea ground state of the electron gas, and bind pairs of electrons into a bound state. The pairs of electrons are called Cooper pairs<sup>10</sup>. The two electrons of the pair have equal and opposite spin momentum.

The existence of an energy gap between the ground state and the quasi-particle excitations of the system was first suggested by Daunt and Mendelssohn<sup>11</sup> to explain the observed absence of thermoelectric effects. Afterwards, a number of experiments have proved the existence of an energy gap, which has a value of about  $1.5 kT_c$  per particle.

One of the most important verifications of the BCS theory was that the microscopic theory predicted that a minimum energy  $E_g(T) = 2\Delta(T)$  should be required to break a pair, creating two quasi-particle excitations. This  $E_g(T)$  was predicted to increase from zero at  $T_c$  to a limiting value at  $T = 0$  K such that

$$E_g(0) = 2\Delta(0) = 3.528k_B T_c = 4\hbar\omega_D \exp\left(\frac{-1}{N(0)V}\right) \quad (1.4)$$

where  $\omega_D$  is the Debye energy for phonons in the lattice,  $N(0)$  is the density of states in energy at the Fermi surface, and  $V$  is the electron-electron attractive potential.

Table 1.1 shows experimental values of  $E_g(0)/k_B T_c$  for various superconducting elements<sup>12</sup>. As we can see from the table, clearly, the BCS theory agrees quite well with most of the examples. Nonetheless, for some of them ( *e.g.* Hg, Pb ), it does not apply precisely. This is because that the BCS theory only holds in the weak coupling limit, *i.e.*

$N(0) V \ll 1$ . Normally, for  $N(0) V \leq 0.3$ , using equation (1.4) to estimate  $T_c$ , it can provide correct results. However, if  $N(0) V > 0.3$ , then, the error from equation (1.2) increases quickly.

**Table 1.1** Results of tunnelling measurements of  $E_g(0)/k_B T_c$  for some superconducting elements. From ref.(12) the chapter by Meservey and Schwarz

Superconductor	$E_g(0)/k_B T_c$
Al	3.37±0.1
Cd	3.20±0.1
Hg	4.60±0.1
In	3.63±0.1
Nb	3.84±0.06
Pb	4.29±0.04
Sn	3.46±0.1
Ta	3.60±0.1

Eliashberg<sup>13</sup> (1960) has proposed a strong coupling limit model to modify the BCS theory. However, because this theory was too complicated to compute, McMillian<sup>14</sup> derived approximate numerical solutions by using a computer.

One should mention here that in 1959 Gor'kov<sup>15</sup> was able to show that the GL theory was in fact a limiting form of the microscopic theory of BCS (suitably generalized to deal with spatially varying situations), valid near  $T_c$ , in which  $\Psi$  is directly proportional to the gap parameter  $\Delta$ . More physically,  $\Psi$  can be thought of as the wavefunction of the centre-of-mass motion of the Cooper pairs.

Since the discovery of superconductivity, a total of 27 pure metals<sup>16</sup> (elements) have been found to be superconductors, and 12 other elements<sup>15</sup> have been found to become superconducting under particular circumstances of high pressure (*e.g.* Ge) or structural disorder (*e.g.* Bi). A number of alloys have also been found to be superconductors. Furthermore, it has even been found that metallic oxides and organic materials can be superconductors. Although the critical temperature  $T_c$  of these materials was lower than the highest  $T_c$  in metal alloys, the major significance of these discoveries is that it broke the initial train of thought, in which the superconducting state only existed in elements or simple alloys, and opened up the new ways in searching for superconducting material.

The special physical properties of superconductors imply that they possess great value in applications. In particular, the discovery of the Josephson effect<sup>17</sup> opened vast vistas in the application of superconductors. However, because superconducting devices have to work at temperatures below  $T_c$ , and before 1986 the highest  $T_c$  recorded was only 23.2 K (for  $Nb_3Ge$ <sup>18</sup>), under such conditions, the application was greatly restricted. Therefore, naturally, people hoped to discover new materials whose  $T_c$  is high enough to work above 77K (nitrogen boiling point) even at room temperature.

## §1.2 Introduction to High Temperature Superconductivity

Prior to 1986 'high-temperature' superconductivity implied a  $T_c$  in the interval of 15 to 23K. In fact, between the discovery of superconductivity in 1911 and the year 1973 the average rate of increase of  $T_c$ , in the persistent attempt to find new and better materials, was 0.3 K per annum, and by 1975 the rate had become virtually zero. The general consensus of opinion was that, as far as ordinary metals and alloys were concerned, the limit had been reached.

However, in 1986, the discovery of a superconducting copper oxide Ba-La-Cu-O with a  $T_c$  of about 30K by J.G. Bednorz and K.A. Muller<sup>19</sup> ushered in a new epoch in the study of superconductivity. There are three major aspects of this discovery, namely, i) it was the first time that a  $T_c$  over 25 K had been discovered, the limiting critical temperature from the BCS theory, ii) it opened up a search for new domains of high  $T_c$  materials. Although the first oxide superconductor was discovered by J.K. Hulm and coworkers<sup>20</sup> in 1964, the highest  $T_c$  found in subsequent work was to be only about 13.7 K in  $\text{LiTi}_2\text{O}_4$  (Johnson *et al* <sup>21</sup> in 1973), which was well below the highest  $T_c$  in alloys material (23.2 K)<sup>18</sup>. iii) it led to the significant discovery of YBCO, with a  $T_c$  above 77 K, the boiling point of liquid nitrogen. Thus, it greatly enhanced the potential value of applications of superconductors.

Not long after Bednorz and Muller's discovery, Chu *et al* <sup>22</sup> observed superconductivity in a  $\text{Y}_{1.2}\text{Ba}_{0.8}\text{CuO}_{4-\delta}$  composition at temperatures as high as 92 K. Within a few days these results had been repeated and verified by a number of groups around the world, and the phase responsible for superconductivity identified as  $\text{YBa}_2\text{Cu}_3\text{O}_{7-\delta}$ .

Several months later, Maede *et al* <sup>23</sup> announced a  $T_c$  of 85 K ~ 110 K in the multiphase compound of nominal composition  $\text{BiSrCaCu}_2\text{O}_{5-\delta}$ . Soon afterwards Sheng and Hermann discovered superconductivity around 90 K and 120 K in the Tl-Ba-Cu-O<sup>24</sup> and Tl-Ba-Ca-Cu-O<sup>25</sup> system, respectively. Recently, the highest  $T_c$  is 250 K for BiSrCaCuO family with eight adjacent  $\text{CuO}_2$  layers in each building block which was deposited on a single crystal of  $\text{SrTiO}_3$  by sequentially imposed layer epitaxy by Laguès *et. al.*<sup>26</sup>.

We now know of at least six different classes of superconductors<sup>27</sup>. These are,

- i) Free-electron-like (s-p and lower d-band) metals, of which typical examples are elemental superconductors such as Hg, Al.
- ii) Strong-coupling, the old-fashioned 'high- $T_c$ ' materials, such as  $\text{Nb}_3\text{Sn}$ .

- iii) Heavy-electron superconductors, such as  $\text{UPt}_3$ .
- iv) Organic superconductors, such as  $\kappa\text{-(ET)}_2\text{Cu}[\text{N}(\text{CN})_2]\text{Cl}_3$ ,  $\text{KC}_{60}$ ,  $\text{Cs}_2\text{RbC}_{60}$ .
- v)  $\text{BaBiO}_3$  - based superconductors, such as  $\text{Ba}_{1-x}\text{K}_x\text{BiO}_3$ .
- vi) High- $T_c$  cuprates, such as  $\text{YBa}_2\text{Cu}_3\text{O}_{7-\delta}$ .

Now, the so-called 'high temperature superconductors' (HTSC, high- $T_c$ , or  $\text{HiT}_c$ ) are normally based on copper oxide. Although some  $\text{BaBiO}_3$ -based and some organic superconductors are also considered as high- $T_c$  superconductors, mainly because their highest  $T_c$  can also exceed the BCS limit, they are out of the scope of this work. We will not discuss these two classes.

All the copper oxide superconductors have perovskite-like structures with the existence of  $\text{CuO}_2$  planes, which we now know are the locus of superconductivity. In Figure 1.4 and 1.5, we show the typical systems structures for  $\text{La}_{2-x}\text{Sr}_x\text{CuO}_4$  and  $\text{YBa}_2\text{Cu}_3\text{O}_{6+\delta}$  system, respectively. However, not all of the cuprates containing  $\text{CuO}_2$  planes are superconductors. In fact, each superconductive cuprate family is derived from an insulating antiferromagnetic (AF) phase either via chemical substitution (*e.g.* substitution of  $\text{La}^{3+}$  by  $\text{Sr}^{2+}$  in  $\text{La}_{2-x}\text{Sr}_x\text{CuO}_4$  system) or varying O-stoichiometry (*e.g.* in  $\text{YBa}_2\text{Cu}_3\text{O}_{6+\delta}$  system). In Figure 1.6, we show a phase diagram of the  $\text{La}_{2-x}\text{Sr}_x\text{CuO}_4$  system. It starts from an AF phase ( $\text{La}_2\text{CuO}_4$ ). Doping with Sr for La, at first lowers the Neel temperature to zero, then a superconducting phase is reached with an abnormal metal state above  $T_c$ . The superconductivity reaches a maximum  $T_c$ , then drops again, and finally enters a metal state. Here we use the word 'abnormal' to describe the metal state above  $T_c$ , because the materials have unusual properties above  $T_c$ , in their normal-state, for example, highly anisotropic electrical resistance. In single crystal cuprates, the resistance in the  $\text{CuO}_2$  plane is metal-like, decreasing linearly with temperature from well above room temperature to  $T_c$ . The study of the resistivity in-plane has suggested that the resistance due to scattering of the charge carriers is not by

lattice vibrations but by interaction with the charge and / or magnetic fluctuations<sup>28</sup>. The resistance perpendicular to the CuO<sub>2</sub> planes is much larger than the in-plane resistance and generally exhibits a semiconductor-like temperature dependence. The difference between in-plane and out-of-plane resistance varies greatly among the cuprates, ranging from a factor of about 10 in the best YBa<sub>2</sub>Cu<sub>3</sub>O<sub>7</sub> samples to greater than 10<sup>4</sup> in the bismuth-based compounds.

The properties of superconducting states of cuprates are also quite different to the conventional superconductors. The values of the ratio of  $E_g(0)/k_B T_c$  (see §1.2 equation 1.4) for the cuprates, seem to range from 5 to 8, which is slightly larger than the value obtained from BCS theory (3.5 for weak-coupling limit, and 4.5 for strong-coupling limit). In these new materials, both the Ginzburg-Landau coherence length,  $\xi_{GL}(T)$ , and penetration depth,  $\lambda$ , are highly anisotropic. For example, in YBa<sub>2</sub>Cu<sub>3</sub>O<sub>7</sub>, at 0 K the coherence length and the penetration depth are about 15 Å and 1400 Å in the CuO<sub>2</sub> plane, respectively, 1.5 Å to 3 Å and 7000 Å perpendicular to the plane, respectively. Therefore, the G-L parameter  $\kappa$  ( $\lambda/\xi_{GL}$ ) is anisotropic and extremely large, much greater than  $1/\sqrt{2}$ .

Since the new materials have such unusual properties, study in this field has brought great excitement to a large number of solid-state physicists, chemists and material scientists. However, the nature of the high T<sub>c</sub> superconductors and the superconductivity mechanisms operating in these materials to-date still remain open questions to be resolved.

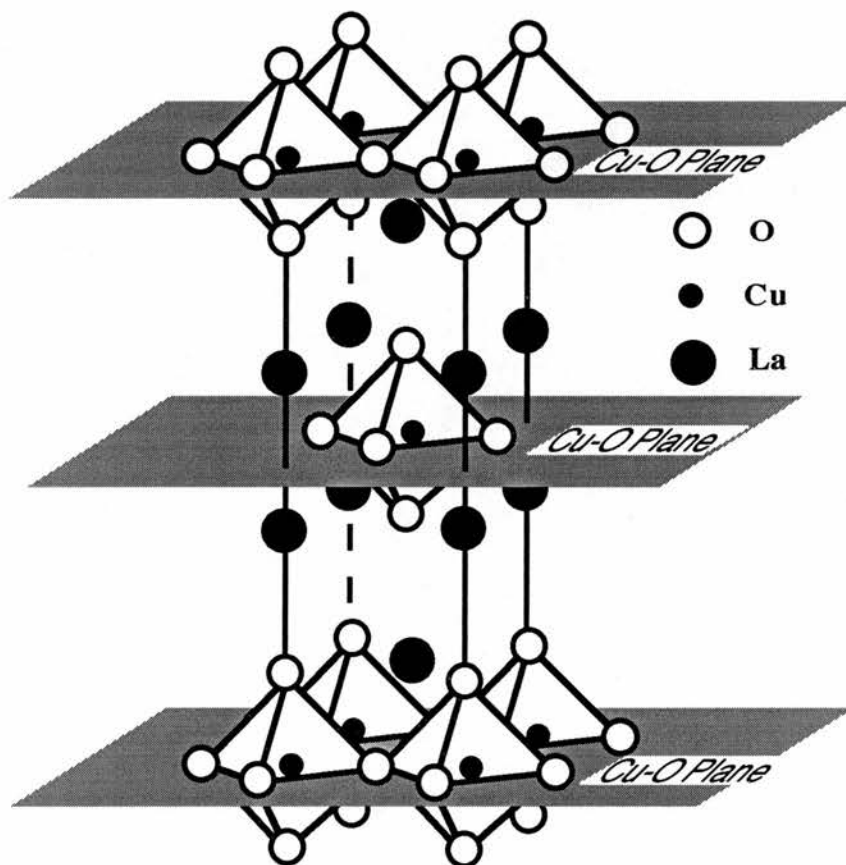


Figure 1.4 Crystal structure of  $\text{La}_{2-x}\text{Sr}_x\text{CuO}_4$

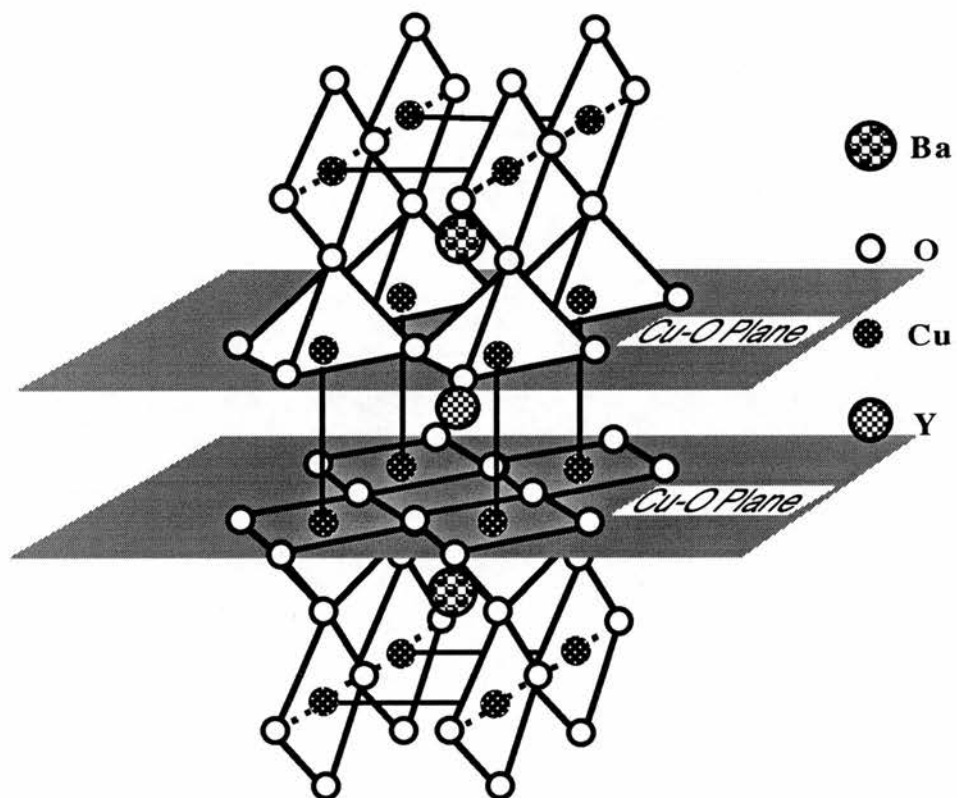


Figure 1.5 Crystal structure of  $\text{YBa}_2\text{Cu}_3\text{O}_{7-\delta}$ .

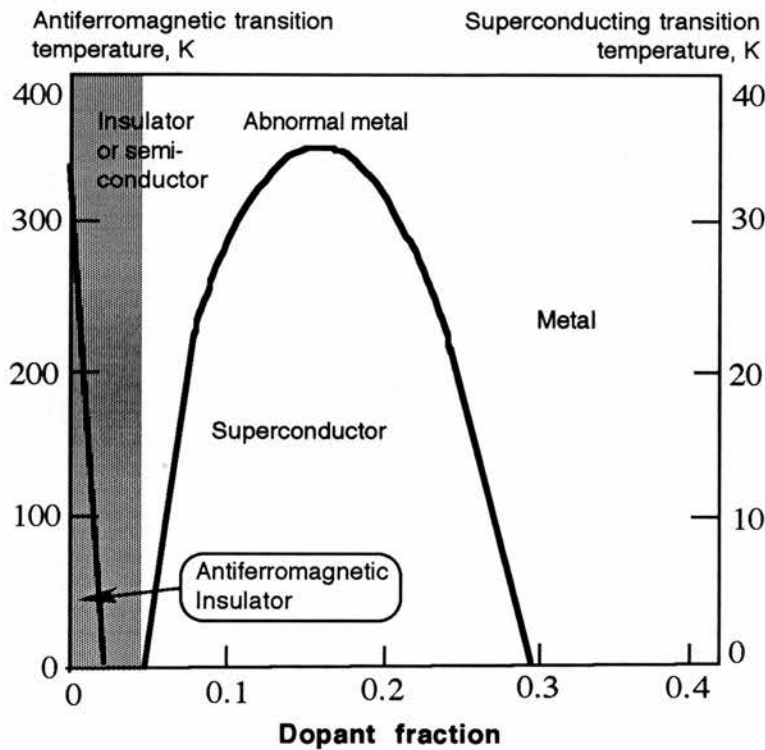


Figure 1.6 Phase diagram for  $\text{La}_{2-x}\text{Sr}_x\text{CuO}_4$  shows changes in the conductive properties of the alkaline-earth-doped lanthanum cuprate that occurs as the concentration of the dopant (Sr) is increased from zero to 0.4. When  $x=0$ , this material is an antiferromagnetic insulator; as  $x$  is increased it becomes, in sequence, insulator, or quantum spin fluid,<sup>29</sup> or semiconductor; superconductor with an unusual conductive state (an abnormal metal state) above  $T_c$ ; and finally, metal. (After Adrian and Cowan<sup>30</sup>)

### §1.3 Introduction to Nuclear Magnetic Resonance

The basic concept of the nuclear magnetic resonance (NMR) may be described in general terms as follows; when the nuclei are placed in a magnetic field Zeeman splitting can occur with an energy of  $\gamma\hbar B$  (where  $\gamma$  is nuclear gyromagnetic ratio,  $B$  is the strength of magnetic field) between the adjacent Zeeman energy levels. Therefore, the nuclei in lower energy levels may transfer to upper ones by absorption of energy of  $\gamma\hbar B$  (*e.g.* the energy can be supplied by applying an oscillating magnetic field with a frequency of  $\omega_0 = \gamma B$ , called the Larmor frequency). For more detail of the NMR concept, see the next chapter.

NMR was first observed in 1946 by Purcell, Torrey and Pound<sup>30</sup> and by Bloch, Hansen and Packard<sup>31</sup>, independently. In the same year, the Bloch equations, which describe the general law of nuclear relaxation, were set up, in which there are two characteristic times, namely  $T_1$  and  $T_2$ .  $T_1$  is called the 'spin-lattice relaxation time', which characterises how fast the nuclear spin magnetization relaxes back after it is disturbed from thermal equilibrium.  $T_2$  is called the 'spin-spin relaxation time', which characterises how fast the individual spins achieve thermal equilibrium with neighbouring spins.

In 1949, when Professor W. Knight made the copper metal NMR experiment, he found that the resonance frequency of  $\text{Cu}^{63}$  in metallic copper occurred at a frequency 0.23% higher than in diamagnetic  $\text{CuCl}$ , provided both resonances were performed at the same value of static field. Further studies revealed that the phenomenon was common to all metals. In fact, this shift is an effect of the interaction of the nuclear spin with the spin paramagnetism of conduction electrons and is now called the Knight shift.

In the following year (1950), the chemical shift was discovered by Dickinson<sup>32</sup> Lindstrom<sup>33</sup> and Proctor and Yu<sup>34</sup>. Chemical shift is the shift resulting from the nuclear

spin interaction with the closed shell electron orbits. Afterwards, the field of NMR has grown extensively both in terms of advanced theory and its applications. It has become a very useful and important tool for studying materials, including superconductors.

The first observation of nuclear magnetic resonance in the superconducting states was made by Reif<sup>35</sup> in 1956. Two years later, Yosida<sup>36</sup> extended the BCS theory to calculate the electronic spin susceptibility as a function of temperature (below  $T_c$ ). From Yosida's theory one would expect that the Knight shift should be zero at the BCS ground state ( $T=0$ ), because all the conduction electrons should pair up. However, this prediction contradicted Reif's experimental data. Soon afterwards, it was found that this contradiction was not due to the failure of BCS theory, but to the incomplete understanding of the mechanisms contributing to the Knight shift. Hg has strong spin-orbit coupling which induces a contribution to the Knight shift which does not vanish at  $T=0$ .

In 1959, Hebel and Slichter<sup>37</sup> first demonstrated the existence of a peak in their measurements of  $T_1$  on Al. This experiment is one of the most remarkable NMR experiments in superconductivity because it provided one of the first confirmations of the pairing aspects of the BCS theory.

For more detailed information on magnetic resonance studies on conventional superconductors the reader is referred to the general review by MacLaughlin<sup>38</sup>.

Since NMR played an important role in understanding the conventional superconductivity, it was natural for the NMR / NQR community to study the new high- $T_c$  superconductors soon after their discovery. In the past six years, a very large number of NMR / NQR papers both in theory and experiment have been published. NMR / NQR studies have made significant contributions to the understanding of different physical phenomena in the normal, as well as in the superconducting states, and are still

continuing to do so. NMR / NQR experiments have made on many different nuclei, such as  $^{63}\text{Cu}/^{65}\text{Cu}$ ,  $^{89}\text{Y}$ ,  $^{17}\text{O}$ ,  $^{205}\text{Tl}/^{203}\text{Tl}$ ,  $^{43}\text{Ca}$ ,  $^{139}\text{La}$ ,  $^{137}\text{Ba}/^{135}\text{Ba}$ ,  $^{207}\text{Pb}$  and others.

## **§ 1.4 Outline of This Work**

Chapter 2 presents the background theories of nuclear magnetic resonance. It gives some details of the interactions such as nuclear-nuclear and hyperfine interactions, in particular, those relevant to this work.

The experimental techniques are presented in Chapter 3, which include the NMR experimental procedure conditions and equipment required, powder sample alignment procedure, and the A.C. susceptibility experiments.

In order to better understand this work, we introduce the Tl-1212 system, including the phase diagram and the structure, and also present some results of Liu's work which are particularly relevant to this work in Chapter 4.

Chapter 5 is the results chapter. We present all the experimental results which involve alignment, A.C. susceptibility, thallium NMR, yttrium NMR, copper NMR and NQR, lead NMR results. We leave the data analysis and discussion to Chapter 6.

Finally, in Chapter 7, we present the conclusions and provide suggestions for future work.

## References

- 1 Onnes H. K. *Leiden Comm.* **120b**, **122b**, **124c** (1911)
- 2 Meissner W., Ochsenfeld R., *Naturewissenschaften* **21**, 787 (1933)
- 3 London F., and London H., *Proc. Roy. Soc.* **A149**, 71 (1935)
- 4 Pippard A. B., *Proc. Roy. Soc.* **A216**, 547 (1953)
- 5 Ginzburg V. L. and Landau L. D. *Soviet Phys. JETP* **20**, 1064 (1950)
- 6 See for example: Tinkham M., "Introduction to Superconductivity", McGraw-Hill, (1975) p9
- 7 Abrikosov A. A. *Soviet Phys. JETP*, **5**, 1174 (1957)
- 8 Bardeen J., Cooper L.N., Schrieffer J.R., *Phys. Rev.* **108**, 1175 (1957)
- 9 Frohlich H., *Phys. Rev.* **79**, 845 (1950)
- 10 Cooper L.N., *Phys. Rev.* **104**, 1189 (1956)
- 11 Daunt J.G., Mendelssohn K., *Proc. Roy. Soc.* **A185**, 225 (1946)
- 12 Parks R.D., *Superconductivity 3rd edn* Methuen, London (1969)
- 13 Eliashberg G.M., *Soviet Phys JETP* **11** 696 (1960), **12**, 1000 (1960)
- 14 McMillian W. L., *Phys. Rev.* **167** 331 (1968)
- 15 Gor'kov L. P., *Soviet Phys. JETP* **9**, 1364 (1959)
- 16 This figure is copied from Fig 13.1 in "Myers H. P., *Introductory Solid State Physics*, Taylor & Francis (1990) p428"
- 17 Josephson B. D., *Phys. Lett.* **1**, 251 (1962)
- 18 Gavalier J.R., *Appl. Phys. Lett.* **23** 480 (1975)

- 19 Bednorz J.G. and Muller K.A. *Z. Phys.* **B64**, 189 (1986)
- 20 Hulm J.K., Jones C.K., Mazelsky R., Hein R.A. and Gibson J.W., *Proceeding of the 9th International Conference on Low-temperature Physics*, Eds. by Daunt J.G., Edwards D.O., Milford F.J. and Yaquib M., 600 (1965)
- 21 Johnson D.C., Prabash H., Zachariasen W.H. and Viswanattian R., *Mater. Res. Bull.* **9**, 777 (1973)
- 22 Wu M.K., Ashburn J.R., Torng C.T., Hor P.H., Meng R.L., Gao L., Huang Z.J., Wang Y.Q. and Chu C.W., *Phys. Rev. Lett.* **58**, 908 (1987)
- 23 Maeda H., Tanaka Y., Fukutomi M. and Asano T., *Jpn. J. Appl. Phys. Lett.* **27**, L209 (1988).
- 24 Sheng Z.Z. and Hermann A. M., *Nature* **332**, 55 (1988)
- 25 Sheng Z.Z. and Hermann A. M., *Nature* **332**, 138 (1988)
- 26 Laguës M., Xie X.M., Tebbji H., Xu X., Mairet V., Beuran C.F., and Deville-Cavellin C., *Science* **262**, 1850 (1993)  
However, this process has not yet been reproduced by other researchers.
- 27 Anderson P.W. and Schrieffer J.R. *Physics Today* **44 no 6**, 54 (1991)
- 28 Adrian F.J. and Cowan D.O., *C & EN special report* 24 (Dec. 1992)
- 29 Sachdev S., private communication, (1993)
- 30 Purcell E.M., Terrey H.C. and Pound P.V., *Phys. Rev.* **69** 37 (1946)
- 31 Bloch F., Hansen W.W. and Packard M., *Phys. Rev.* **69** 127 (1946)
- 32 Dickinson W.C., *Phys. Rev.* **77** 736 (1950)
- 33 Lindstom G., *Phys. Rev.* **78** 817 (1950)

- 34 Proctor W.G. and Yu F.C., *Phys. Rev.* **77** 717 (1950)
- 35 Reif F., *Phys. Rev.* **106** 208 (1957)
- 36 Yosida K., *Phys. Rev.* **101** 769 (1958)
- 37 Hebel L.C. and Slichter C.S., *Phys. Rev.* **113** 1504 (1959)
- 38 MacLaughlin D.E., in *Solid State Physics*, vol **31**, eds. by Ehrenreich H., Seitz F. and Turnbull D., Academic Press, New York, 1 (1976)

## Chapter 2

# The Nuclear Magnetic Resonance Background Theories

### § 2.1 Introduction

In this chapter, we will summarise the nuclear spin property, basic nuclear resonance theory, the nuclear interactions, and the nuclear relaxations. For more detailed treatments, the reader is referred to the books by Slichter<sup>1</sup>, Abragam<sup>2</sup>, Rushworth and Tunstall<sup>3</sup>, Winter<sup>4</sup>, Carter, Bennett and Kahan<sup>5</sup>

### § 2.2 The Nuclear Spins

The nucleus is an assembly of neutrons and protons. Each neutron or proton has a spin angular momentum which corresponding to a quantum number  $\frac{1}{2}$ . In the nucleus, the nucleons, *i.e.* neutrons or protons, also possess orbital angular momentum. When the orbital angular momentum combines with the spin angular momentum, it produces a total nuclear spin angular momentum,  $\hbar\mathbf{I}$ ,

$$|\mathbf{I}| = [I(I + 1)]^{1/2} \quad (2.1)$$

where  $I$  is corresponding to quantum number, which may be different from nucleus to nucleus. The spinning nucleon produces a magnetic moment, the total nuclear magnetic

moment  $\boldsymbol{\mu}$  is expressed as

$$\boldsymbol{\mu} = \gamma \hbar \mathbf{I} \quad (2.2)$$

where  $\gamma$  is the nuclear gyromagnetic ratio.

### § 2.3 The Basic Theory of Nuclear Resonance

When the nucleus of magnetic moment  $\boldsymbol{\mu}$  is placed in an applied magnetic field  $\mathbf{B}_0$ , the interaction between  $\boldsymbol{\mu}$  and  $\mathbf{B}_0$  can be described quantum mechanically by the Zeeman Hamiltonian:

$$\mathcal{H}_z = -\boldsymbol{\mu} \cdot \mathbf{B}_0 = -\gamma \hbar \mathbf{I} \cdot \mathbf{B}_0 \quad (2.3a)$$

Taking the magnetic field  $\mathbf{B}_0$  to be along the z-direction, we can write that

$$\mathcal{H}_{zz} = \gamma \hbar B_0 I_z \quad (2.3b)$$

The allowed energies of the system are

$$E_{mz} = -\gamma \hbar B_0 m \quad (2.4)$$

where  $m = I, I-1, \dots, -I$ . So the nuclei have  $2I+1$  energy levels.

If an oscillating magnetic field  $\mathbf{B}_1$  of frequency  $\omega$  is applied perpendicular to the main field  $\mathbf{B}_0$ , when

$$\hbar \omega = -\gamma \hbar B_0 \quad (2.5)$$

the nuclei may obtain an energy of  $\hbar \omega$  to be transferred from the lower energy levels to the adjacent upper energy levels. The frequency at which the resonance occurs is known as the Larmor frequency,  $\omega_0$ , defined by

$$\omega_0 = \gamma B_0 \quad (2.6)$$

Considering an isolated ensemble of nuclear spins in a magnetic field  $\mathbf{B}_0$ , ( this is an ideal condition ), the population of each energy level follows the Boltzmann distribution *i.e.* proportional to  $\exp\left(\frac{\gamma\hbar B_0 m}{kT_s}\right)$ , where  $k$  is the Boltzmann constant and  $T_s$  is the spin temperature.

## § 2.4 The Nuclear Interactions

In the previous section, we assumed the nuclear spins to be isolated from their surroundings. In fact, complete isolation is not physically possible, and the nuclei must have interactions with other nuclei and electrons within the sample. The total interaction can be written by the Hamiltonian:

$$\mathcal{H} = \mathcal{H}_0 + \mathcal{H}_{dip} + \mathcal{H}_{nd} + \mathcal{H}_{en} + \mathcal{H}_{ex} + \mathcal{H}_Q \quad (2.7)$$

Where

$\mathcal{H}_0$  is the magnetic energy (see § 2.3),

$\mathcal{H}_{dip}$  is the magnetic dipole-dipole interaction energy (§ 2.4.1),

$\mathcal{H}_{nd}$  is the nuclear spin interaction with the diamagnetism of closed shell electron orbits (§ 2.4.2),

$\mathcal{H}_{en}$  is the nuclear-electron interaction energy (§ 2.4.3 and § 2.5),

$\mathcal{H}_{ex}$  is the exchange interaction energy (§ 2.4.4),

and  $\mathcal{H}_Q$  is the electric quadrupole interaction energy (§ 2.4.5).

### § 2.4.1 The Nuclear Magnetic Dipole Interaction

In a nuclear spin system, each spin is subject to the varying local field produced by its neighbours, so all the spins will interact with each other. The interaction between two magnetic  $\boldsymbol{\mu}_1$  and  $\boldsymbol{\mu}_2$  is given by the Hamiltonian<sup>1</sup>

$$\mathcal{H}_{dip} = \frac{\mu_0}{4\pi} \left[ \frac{\boldsymbol{\mu}_1 \cdot \boldsymbol{\mu}_2}{r_{12}^3} - \frac{3(\boldsymbol{\mu}_1 \cdot \mathbf{r}_{12})(\boldsymbol{\mu}_2 \cdot \mathbf{r}_{12})}{r_{12}^5} \right] \quad (2.8)$$

Since  $\boldsymbol{\mu}_1 = \gamma \hbar \mathbf{I}_1$ ,  $\boldsymbol{\mu}_2 = \gamma \hbar \mathbf{I}_2$ , and if we write  $\mathbf{I}_1$  and  $\mathbf{I}_2$  in term of unit vectors

$$\mathbf{I}_1 = I_{1x}\mathbf{i} + I_{1y}\mathbf{j} + I_{1z}\mathbf{k} \quad (2.8a)$$

$$\mathbf{I}_2 = I_{2x}\mathbf{i} + I_{2y}\mathbf{j} + I_{2z}\mathbf{k} \quad (2.8b)$$

$$I^+ = I_x + iI_y \quad (2.8c)$$

$$I^- = I_x - iI_y \quad (2.8d)$$

and changing from Cartesian coordinates to spherical polar coordinates, with  $\mathbf{B}_{appl}$  defining the z-axis, the equation (2.8) can be written<sup>1</sup>

$$\mathcal{H}_{dip} = \left( \frac{\mu_0}{4\pi} \right) \frac{\gamma^2 \hbar^2}{r_{12}^3} (A + B + C + D + E + F) \quad (2.9)$$

where

$$A = I_{1z}I_{2z}(1 - 3\cos^2 \theta_{12}) \quad (2.9a)$$

$$B = -\frac{1}{4} (I_1^+ I_2^- + I_1^- I_2^+) (1 - 3\cos^2 \theta_{12}) \quad (2.9b)$$

$$C = -\frac{3}{2} (I_1^+ I_{2z} + I_{1z} I_2^+) \sin \theta_{12} \cos \theta_{12} \exp(-i\phi_{12}) \quad (2.9c)$$

$$D = -\frac{3}{2} \left( I_1^- I_{2z} + I_{1z} I_2^- \right) \sin \theta_{12} \cos \theta_{12} \exp(i\phi_{12}) \quad (2.9d)$$

$$E = -\frac{3}{4} I_1^+ I_2^+ \sin^2 \theta_{12} \exp(-2i\phi_{12}) \quad (2.9e)$$

$$F = -\frac{3}{4} I_1^- I_2^- \sin^2 \theta_{12} \exp(2i\phi_{12}) \quad (2.9f)$$

The term  $A$  is the classical interaction between two dipoles; term  $B$  induces mutual spin flips between dipoles and hence yields an efficient mechanism for the transport of nuclear spin energy; term  $C$  and  $D$  flip one spin only; term  $E$  and  $F$  flip both spins in one direction. The  $C$ ,  $D$ ,  $E$ ,  $F$  terms produce absorption lines at frequencies 0 and  $2\omega_0$  which are so weak as to be negligible. A truncated dipolar Hamiltonian is therefore formed, containing only the  $A$  and  $B$  terms which commute with the Zeeman Hamiltonian. The simplified Hamiltonian (with the contributions only coming from  $A$  and  $B$ ) becomes:

$$\mathcal{H}_{dip} = \frac{\mu_0 \gamma^2 \hbar^2}{16\pi} \sum_{i,j} \frac{(1-3\cos^2 \theta_{ij})}{r_{ij}^3} (3I_{iz} I_{jz} - \mathbf{I}_i \cdot \mathbf{I}_j) \quad (2.10)$$

For solids this dipolar interaction can lead to a broad NMR linewidth. Since this interaction is proportional to  $r_{ij}^{-3}$ , it is therefore very sensitive to the changes in inter-nuclear distances. It should be noted that in equation (2.10), there is a  $(1-3\cos^2\theta)$  term which means the dipolar interaction is orientation dependent.

### § 2.4.2 The Nuclear Spin Interaction With Closed Shell Electron Orbits

In any non-metallic solid, there exists a shift which is called the chemical shift and which is caused by the nuclear spin interaction with the closed shell electron orbits.

Therefore, for a particular nucleus, the NMR line will be at a different frequency for a different chemical environment. The chemical shift,  $\sigma$ , normally has two contributions, *i.e.* a diamagnetic term,  $\sigma_d$ , and a paramagnetic term,  $\sigma_p$ :

$$\sigma = \sigma_d + \sigma_p \quad (2.11)$$

The diamagnetic term is due to the applied magnetic field producing an electronic charge circulation around the nucleus. The circulation creates a magnetic field opposed to the applied magnetic field, according to Lenz's law. The paramagnetic term is a correction for the distortion of the electron motion and the non-spherical charge distribution of the electron.

### § 2.4.3 The Interaction Between Nucleus and Conduction Electron

The interaction between a nuclear moment  $\mu_I$  and a conduction electron orbital moment  $\mu_L$  and spin moment  $\mu_s$  may be described by the Hamiltonian<sup>1</sup>

$$\mathcal{H}_{en} = \frac{\mu_0}{4\pi} \left[ \frac{2\mu_I \cdot \mu_L}{r^3} - \left( \frac{\mu_S \cdot \mu_I}{r^3} - \frac{3(\mu_I \cdot \mathbf{r})(\mu_S \cdot \mathbf{r})}{r^5} \right) + \frac{8\pi}{3} \mu_I \cdot \mu_S \delta(r) \right] \quad (2.12)$$

The first term represents the coupling between the nucleus and the electron orbital momentum. The resultant of this term will lead to an electron orbital shift  $K_{orb}$ . The second and third terms represent the dipolar coupling between the nucleus and the electron spin and is analogous to the interaction presented in the previous section (§ 2.4.1). These two terms should vanish in diamagnetic materials where the total electron spin and orbital moment is zero, but may need to be considered in metals if the electron wave function at the Fermi surface has any p or d-wave character. The last term is the

Fermi contact interaction, which becomes important close to the nucleus where the dipolar approximation breaks down.

#### § 2.4.4 The Exchange Interaction

The presence of a nuclear moment on a lattice site has the effect of making that site more favourable to an electron of parallel moment. Because of the presence of electron bonds, the preferred spin orientation of an electron on one site causes an electron on the nearby sites to have a preferred orientation in the opposite direction. This results in the nucleus on the nearby site being in the non-zero field of its own electron and effective nuclear-nuclear exchange coupling results, since the field direction would reverse if the nucleus on the original site reversed. For a system of spins, this may be expressed in terms of an effective exchange Hamiltonian:

$$\mathcal{H}_{ex} = \sum_{i,j} A_{ij}(r_{ij}) \mathbf{I}_i \cdot \mathbf{I}_j \quad (2.13)$$

where  $\mathbf{I}_i$  and  $\mathbf{I}_j$  are the spins of the nuclei linked by the interaction,  $A_{ij}(r_{ij})$  is a function of  $r_{ij}$ , the distance between the two nuclei.

In solids, the main effect of this interaction is on the resonance linewidth<sup>6</sup>. If all the nuclei are alike, the linewidth is reduced (exchange narrowing). However, if the nuclei are unlike, the line is broadened.

#### § 2.4.5 The Quadrupole Interaction

Nuclei of spin  $I$  greater than  $\frac{1}{2}$  usually possess electric quadrupole moments which can interact with electric field gradients to produce a perturbation of the nuclear energy levels. (Figure 2.1) For  $I = \frac{1}{2}$  there is no quadrupole moment  $Q$  so that no quadrupole

effects are seen in the NMR spectra. In materials for which a nucleus of any spin,  $I$ , is in a site of cubic symmetry, the net interaction is also zero.

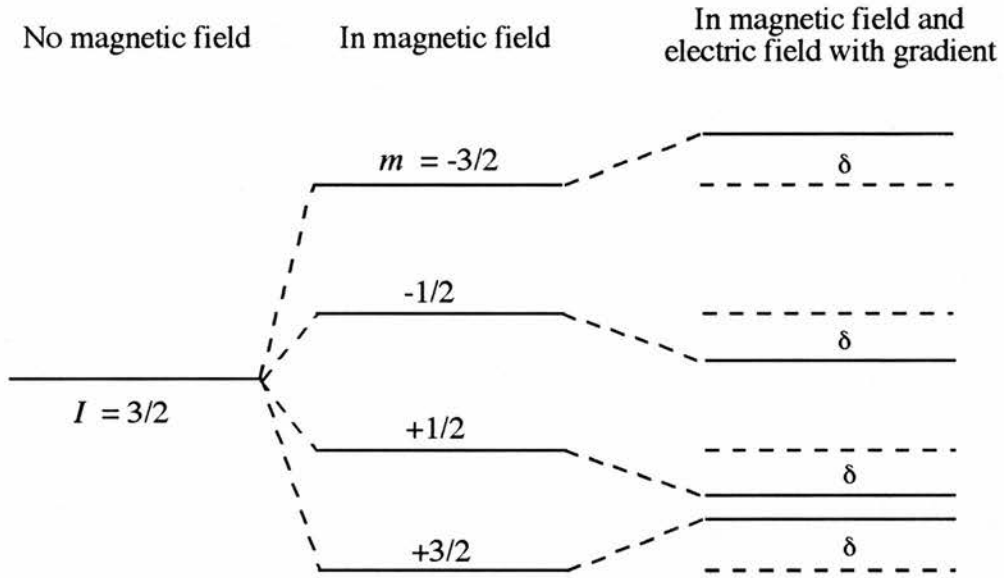


Fig.2.1 The perturbation of the Zeeman splitting by a nuclear quadrupole interaction.

The interaction between the quadrupole moment  $Q$  and the electric field gradient  $q$  can also be represented by the Hamiltonian<sup>2</sup>

$$\mathcal{H}_Q = \frac{e^2 q Q}{4I(2I-1)} \left[ 3I_z^2 - \mathbf{I}^2 + \frac{1}{2} \eta (I_+^2 + I_-^2) \right] \quad (2.14)$$

where

$$eQ = \int \rho(\mathbf{r}) (3z^2 - r^2) d\tau$$

(  $\rho(\mathbf{r})$  is the nuclear charge density distribution ) (2.14a)

$$eq = V_{zz} \quad (V \text{ is the external electric potential}) \quad (2.14b)$$

$$\eta = \frac{(V_{xx} - V_{yy})}{V_{zz}} \quad (\eta \text{ called asymmetry parameter}) \quad (2.14c)$$

$$I_+ = I_x + iI_y \quad (I \text{ is nuclear spin quantum number}) \quad (2.14d)$$

$$I_- = I_x - iI_y \quad (2.14e)$$

$$V_{\alpha\alpha} = \frac{\partial^2 V}{\partial^2 \alpha} \quad (\alpha = x, y, z, V_{xx} \leq V_{yy} \leq V_{zz}) \quad (2.14f)$$

#### § 2.4.5.1 The First-order Quadrupole Effects

If  $\mathcal{H}_Q$  is small compared to the Zeeman Hamiltonian then it is sufficient to calculate the transition frequency for ( $m \leftrightarrow m-1$ ) by first order perturbation theory giving<sup>5</sup>:

$$\nu_{(m \leftrightarrow m-1)}^{(1)} = \nu_0 + \frac{\nu_Q}{2} \left(m - \frac{1}{2}\right) \left(3 \cos^2 \theta - 1 - \eta \sin^2 \theta \cos 2\phi\right) \quad (2.15)$$

where  $\theta$  is the angle between  $\mathbf{B}_0$  and the principal z-axis and  $\phi$  is the azimuthal angle.  $\nu_0$  is the Larmor frequency.  $\nu_Q$  is an expression for the pure quadrupole frequency and defined as:

$$\nu_Q = \frac{3e^2 qQ}{2I(2I-1)h} \quad (2.16)$$

The result is that the  $m = \pm \frac{1}{2}$  levels are shifted by the same amount so the central transition frequency remains at  $\omega_0$ . The remaining energy levels are no longer equally spaced and so produce a series of  $2I-1$  lines symmetrically displaced around  $\omega_0$ , called *satellite* lines. Figure 2.2 shows the absorption curve for a nuclei of  $I = \frac{3}{2}$  in a powdered sample<sup>7</sup>.

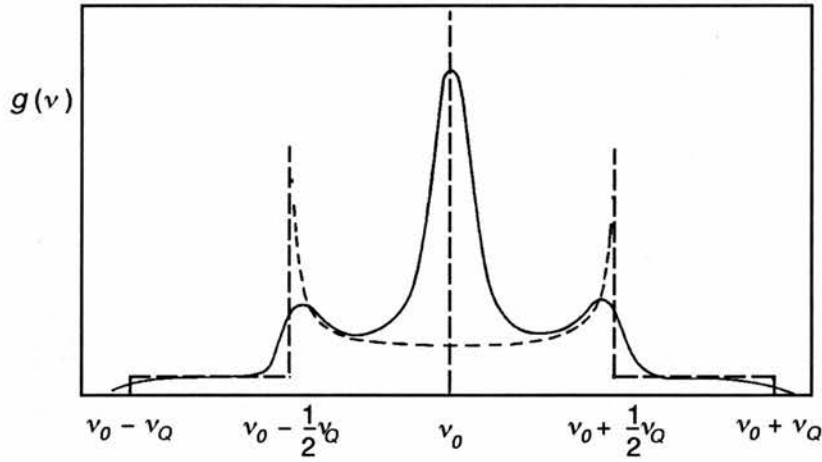


Figure 2.2 *First-order quadrupole splitting. The broken line describes the theoretical magnetic resonance absorption of spin 3/2 in axially symmetric electric fields of gradient  $eq$ , calculated for a powder specimen with isotropic orientation distribution. The full line includes symmetric broadening.  $\nu_0 = e^2 qQ/2h$*

#### § 2.4.5.2 The Second-order Quadrupole Effects

If  $\mathcal{H}_Q$  is of the same order as the Zeeman Hamiltonian then the second order perturbation should be considered. It gives (for  $\eta = 0$ )<sup>5</sup>:

$$\nu_{m \leftrightarrow m-1}^{(2)} = \nu_{m \leftrightarrow m-1}^{(1)} + \left( \frac{\nu_Q^2}{32\nu_0} \right) \sin^2 \theta \left\{ \begin{aligned} &\cos^2 \theta [102m(m-1) - 18I(I+1) + 39] \\ &- [6m(m-1) - 2I(I+1) + 3] \end{aligned} \right\} \quad (2.17)$$

and leads to a shift in the central transition and a second order quadrupole broad line.

For a central  $m = 1/2 \leftrightarrow -1/2$  transition and  $I = 3/2$ , the equation (2.17) becomes:

$$\nu_{1/2 \leftrightarrow -1/2} = \nu_0 + \frac{3\nu_Q^2}{16\nu_0} (1 - \cos^2 \theta) (1 - 9\cos^2 \theta) \quad (2.17a)$$

The powder pattern resulting from a random distribution of crystallite orientations is shown in Figure 2.3.

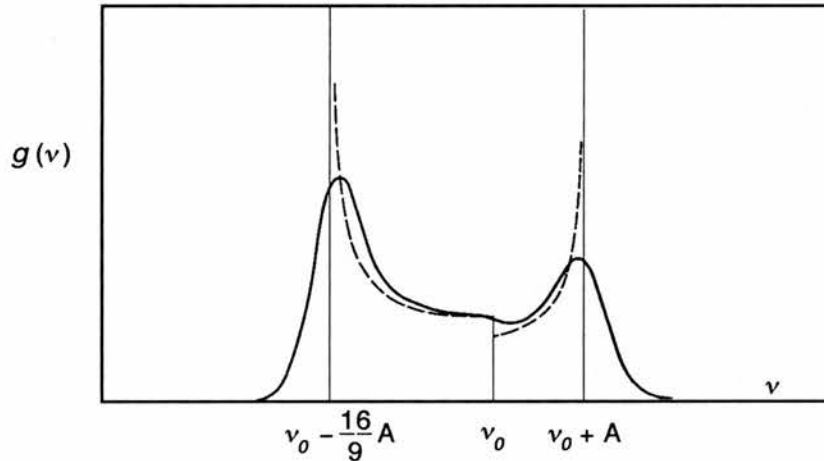


Figure 2.3 *Second-order quadrupole splitting of the central  $m = 1/2 \leftrightarrow -1/2$  transition. The dashed curve shows the theoretical absorption line shape in a powdered sample of axially symmetric crystals. The full curve indicates the effect of dipolar broadening.  $A = \frac{3\nu_Q^2}{16\nu_0}$ .*

## § 2.5 The Knight Shift

### § 2.5.1 Introduction

Magnetic shifts arise because of the simultaneous interaction of a nucleus with an electron and that of the electron with the applied field  $\mathbf{H}_0$ , the NMR resonance frequency  $\nu$  is given (in the absence of nuclear electric quadrupole effects) by:

$$\nu = \frac{\gamma H_0}{2\pi}(1 + \Delta) \quad (2.18)$$

where  $\gamma$  is the nuclear gyromagnetic ratio and  $\Delta$  is the sum of chemical shift and Knight shift, *i.e.*:

$$\Delta = \sigma + K \quad (2.19)$$

where  $\sigma$  is the chemical shift (see § 2.4.2), and  $K$  is the Knight shift resulting from nuclear spin interaction with the conduction electrons.

### § 2.5.2 Knight Shift in the Normal State

In the normal state, the conduction electron susceptibility,  $\chi_{con}$ , in a metal can be divided into three contributions:

$$\chi_{con} = \chi_s + \chi_{orb} + \chi_d \quad (2.20)$$

where  $\chi_s$ ,  $\chi_{orb}$  and  $\chi_d$  are the s-type Pauli spin susceptibility, the Van Vleck orbital susceptibility and the Pauli spin susceptibility of non-s type electrons of which the d-type electrons contribution will be particularly important in transition metals, respectively.

Corresponding to each term of the susceptibility there exists a contribution to the Knight shift:

$$K = K_s + K_{orb} + K_d = A_s \chi_s + A_{orb} \chi_{orb} + A_d \chi_d \quad (2.21)$$

Each mechanism produces a shift component proportional to the corresponding susceptibility in the linear approximation, where the local field at a nuclear site and the corresponding bulk magnetization are themselves linearly related. The constants of proportionality,  $A_s$ ,  $A_{orb}$  and  $A_d$  are the hyperfine fields.

It should be mentioned here that the definition of Knight shift and chemical shift may be different to the above in some articles<sup>8</sup> in which Knight shift contains the s-type conduction electron spin susceptibility  $\chi_s$  and  $\chi_d$  contributions, whilst  $\sigma$  the chemical shift contains  $K_{orb}$  as well as true chemical shifts.

### § 2.5.3 Orientation Dependence of Knight Shift

The electron-nuclear dipole interaction (the second term of equation (2.12)) causes anisotropic effects in the Knight shifts when the symmetry at the nucleus is lower than cubic. The Knight shift for this case, in the absence of any quadrupole effects, is written as<sup>5</sup>:

$$K = K_{iso} + \frac{K_1}{2}(3 \cos^2 \theta - 1) - \frac{K_2}{2} \sin^2 \theta \cos 2\phi \quad (2.22)$$

where  $K_{iso}$  is the isotropic shift defined as:

$$K_{iso} = \frac{1}{3}(K_x + K_y + K_z) \quad (2.22a)$$

and

$$K_1 = K_z - K_{iso} \quad (2.22b)$$

$$K_2 = K_y - K_x \quad (2.22c)$$

$K_x, K_y$  and  $K_z$  are the Knight shift in x, y and z direction component, respectively.  $\theta$  and  $\phi$  are defined as § 2.4.5.

If the sample is axially symmetric, as are the samples studied in this work, then  $K_2 = 0$  and equation (2.22) becomes

$$K = K_{iso} + \frac{K_1}{2}(3 \cos^2 \theta - 1) \quad (2.23)$$

and

$$K_{iso} = \frac{\nu_0 - \nu_{ref}}{\nu_0} = \frac{1}{3}(K_{//} + 2K_{\perp}) \quad (2.23a)$$

$$K_{\perp} = K_{ax} = \frac{1}{3} \frac{\nu_{//} - \nu_{\perp}}{\nu_{ref}} = \frac{1}{3}(K_{//} - K_{\perp}) \quad (2.23b)$$

where  $K_{//}$  and  $K_{\perp}$  are the Knight shift in c-axis (the axis of axial symmetry) parallel and perpendicular to the applied field  $\mathbf{H}_0$ , respectively.  $\nu_{ref}$  is the resonance frequency of a suitable reference material. The spectrum for a resonance with axial Knight shift effects is shown in Figure 2.4.

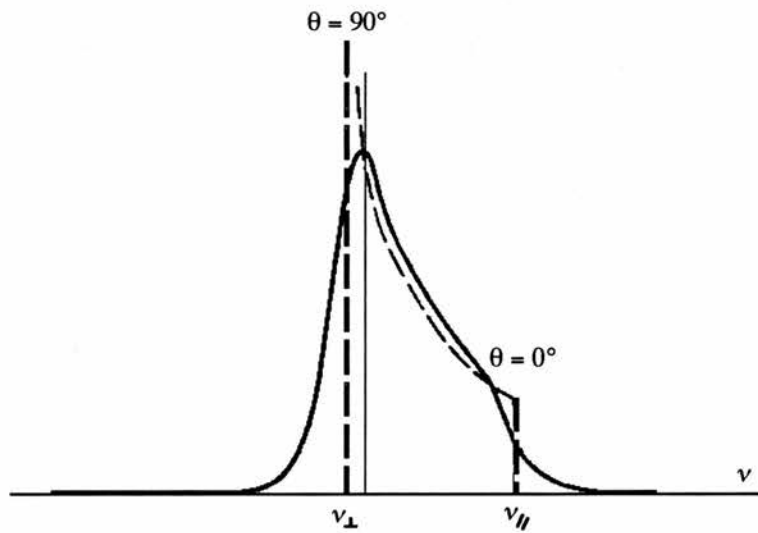


Figure 2.4 *Spectrum for a resonance with axial Knight shift effects. The dashed line shows the theoretical absorption line shape and the full line indicates the symmetrically broadened shape.*

### § 2.5.4 Knight Shift and Quadrupole Effects Present Simultaneously

In § 2.4.5 and § 2.5.3, we individually described the nuclear quadrupole effects and the Knight shift. Now if the nuclear quadrupole effects and Knight shift are present simultaneously, the transition frequency for ( $m \leftrightarrow m-1$ ) should be (for the case of axial symmetry *i.e.*  $\eta = 0$  and  $K_2 = 0$ )<sup>5</sup>:

$$\begin{aligned} \nu(m \leftrightarrow m-1) = \nu_0 + & \left[ \frac{1}{2} \nu_Q \left( m - \frac{1}{2} \right) + \frac{K_{ax} \nu_{ref}}{2} \right] (3 \cos^2 \theta - 1) \\ & + \left( \frac{\nu_Q^2}{32 \nu_0} \right) \sin^2 \theta \left\{ \cos^2 \theta [102m(m-1) - 18I(I+1) + 39] \right. \\ & \left. - [6m(m-1) - 2I(I+1) + 3] \right\} \end{aligned} \quad (2.24)$$

This case has been studied by Jones *et al.*<sup>9</sup>. For the central ( $m = 1/2 \leftrightarrow -1/2$ ) resonance and  $I = 3/2$  the equation (2.24) can be written:

$$\begin{aligned} \nu_{m=1/2 \leftrightarrow -1/2} = \nu_0 + & \frac{K_{ax} \nu_{ref}}{2} (3 \cos^2 \theta - 1) + \left( \frac{3 \nu_Q^2}{16 \nu_0} \right) \sin^2 \theta (1 - 9 \cos^2 \theta) \\ = \nu_0 & \left[ 1 + a (3 \cos^2 \theta - 1) + \frac{b}{\nu_0^2} \sin^2 \theta (1 - 9 \cos^2 \theta) \right] \end{aligned} \quad (2.25)$$

where

$$a = \frac{K_{ax}}{1 + K_{iso}} \quad \text{and} \quad b = \frac{\nu_Q^2}{16} \left[ I(I+1) - \frac{3}{4} \right] = \frac{3 \nu_Q^2}{16} \quad (2.25a)$$

The line shape for a powdered sample depends upon the strength of the two interactions (*i.e.* the quadrupole and axial shift interactions). Jones *et al.*<sup>8</sup> have demonstrated the line shape as a function of  $r$ , the parameter which measures the relative strength of the two interactions, shown in Figure 2.5. Figure 2.6 shows the angular dependences of  $K_{ax}$  and second-order quadrupole frequency shifts.

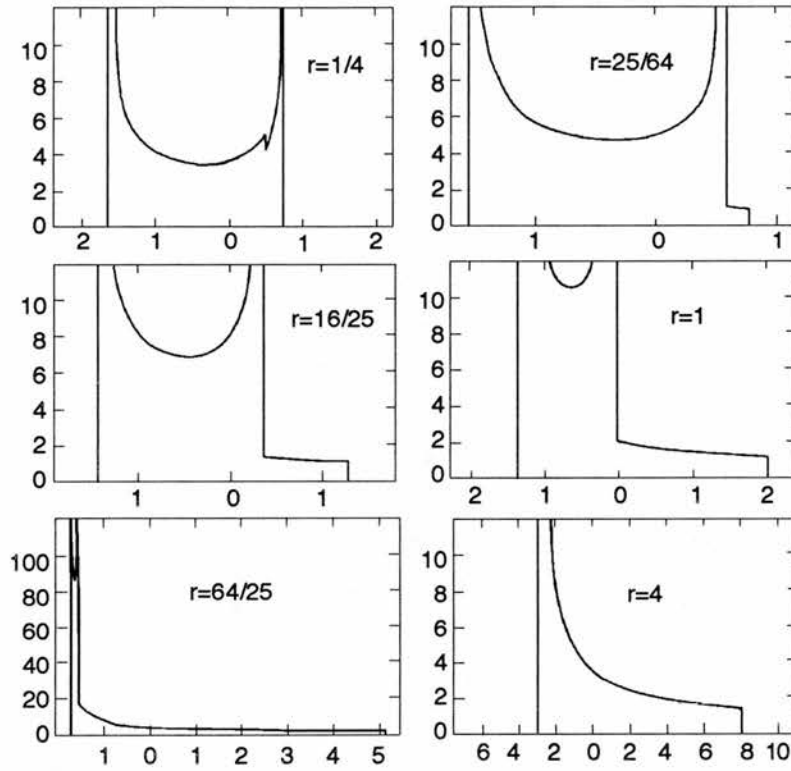


Figure 2.5 Line shape function for the case of combined quadrupole and axial shift interactions. The parameter  $r = av_0^2/b$  measures the relative strength of the two interactions. (After Jones et al. <sup>9</sup>)

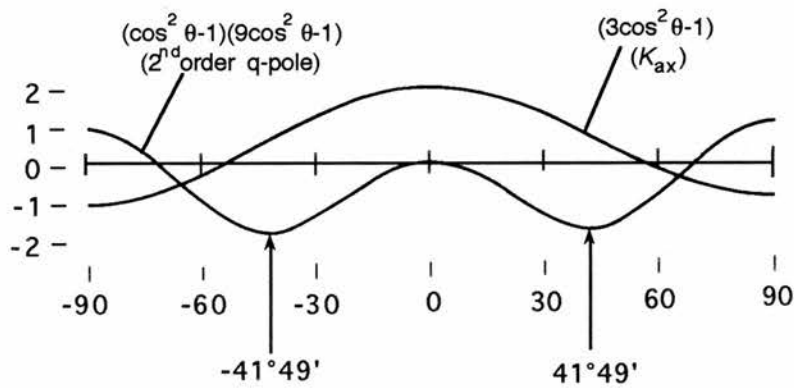


Figure 2.6 The second-order quadrupole frequency shifts and  $K_{ax}$  as a function of angle  $\theta$ , between the crystal  $c$ -axis and the applied magnetic field  $\mathbf{B}$ . (After Carter et al. <sup>5</sup>)

### § 2.5.5 Knight Shift in Superconducting State

In the superconducting state the temperature dependence of electron spin susceptibility has been calculated from the BCS theory by Yosida<sup>10</sup>. Within the strict BCS theory with s-wave orbital and singlet spin pairing, one has vanishing spin susceptibility at  $T=0\text{K}$ . In the event that the Knight shift has both  $K_s$  and  $K_{\text{orb}}$  contributions, one expects that  $K_s(T=0\text{K}) = 0$ , and  $K(T=0\text{K}) = K_{\text{orb}}$ . Figure 2.7 shows that the experimental data for aluminium obeys the theory of Yosida.

However, the temperature dependence of  $\chi_s$  and  $K_s$  will be modified if for example, one has p-wave rather than s-wave orbital pairing state (with triplet rather than singlet spin pairing)<sup>11</sup>.

For more details of NMR in the superconducting state of BCS materials, the reader is referred to a review article by MacLaughlin<sup>12</sup>.

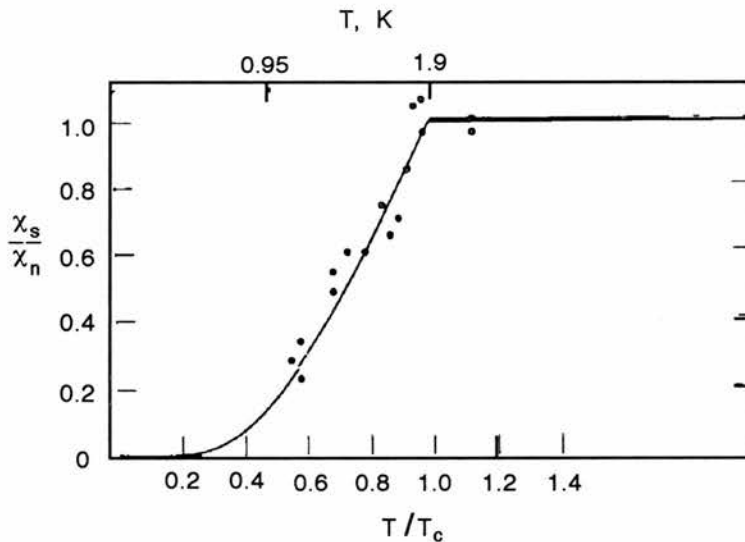


Figure 2.7 *Spin susceptibility in superconducting aluminium; the data of Fine et al.<sup>13</sup>. The theory of Yosida<sup>10</sup> is well obeyed. (After MacLaughlin<sup>14</sup>).*

## § 2.6 NMR in Type-II Superconductors

For a type-II superconductor, the magnetic field can penetrate in the form of a flux lattice.<sup>15,16,17</sup> The original calculation of Abrikosov<sup>15</sup> assumed a square lattice. Later Kleiner *et al.*<sup>18</sup> showed that a triangular lattice was slightly more favourable energetically which has been proved by a number of experiments. Figure 2.8 shows the ideal magnetic field distribution in the mixed phase of a type-II superconductor. It has been pointed out that many kinds of random distribution of the flux lattice, such as pinning at defects, impurities, and the surface, will significantly degrade the sharpness of the saddle-point singularity resulting in a broadening of the NMR spectrum.<sup>19</sup> The decay of field from  $M$  is exponential with a decay constant equal to the penetration depth.

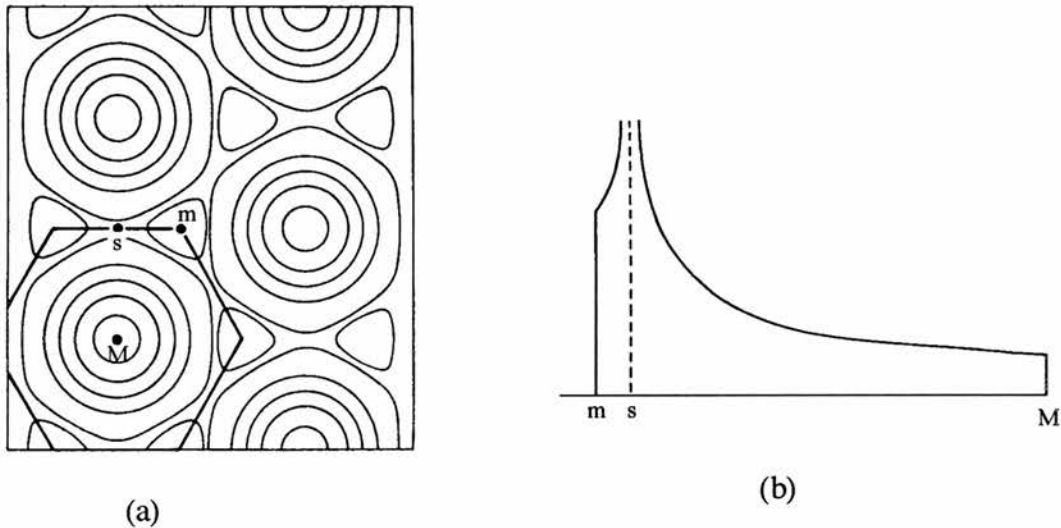


Figure 2.8 (a) *Vortex lattice in the mixed state. Contours of constant magnetic field on positions of maximum field ( $M$ ), minimum field ( $m$ ) and saddle points ( $s$ ).* (b) *Local field distribution function  $f(h)$ . The maximum ( $M$ ), minimum ( $m$ ) and saddle ( $s$ ) field points are shown. Plot of numbers of nuclei at field  $h$ ,  $f(h)$ , as function of  $h$ .*

Using NMR techniques to study type II superconductors, one may obtain information on the penetration of flux in high magnetic fields from the line shape. To simplify, if we ignore shift anisotropy,<sup>20</sup> the linewidth should be related to an average penetration depth. For a Gaussian line shape, the second moment is a good measurement of its linewidth. Pincus *et al.*<sup>17</sup> have calculated the second moment of field distribution  $(\overline{\Delta h^2})^{1/2}$  for  $H_{c1} \ll H \ll H_{c2}$ ,

$$(\overline{\Delta h^2})^{1/2} = \frac{n\varphi_0 d}{\lambda \sqrt{4\pi}} \left[ 1 + \left( \frac{2\pi\lambda}{d} \right)^2 \right]^{-1/2} \approx \frac{\varphi_0}{\lambda^2 \sqrt{16\pi^3}} \quad (2.26)$$

where  $\varphi_0 = hc/2e$  is the quantum of flux,  $\lambda$  is the penetration depth.

## § 2.7 Nuclear Relaxation

### § 2.7.1 Spin-lattice Relaxation

As mentioned at end of §2.3, a group of spins ( $\frac{1}{2}$ ) nuclei placed in a magnetic field would distribute themselves between the two states according to the Boltzmann relation. During this process, there must be energy transferred. Therefore, the induced magnetisation ( $M_0$ ) cannot form instantaneously. We introduce a relaxation time  $T_1$  and write:

$$\frac{dM}{dt} = \frac{M_0 - M}{T_1} \quad (2.27)$$

$$M = M_0 \left( 1 - \exp\left(-t/T_1\right) \right) \quad (2.28)$$

where  $M_0$  is the thermal equilibrium magnetization and  $M$  is the magnetization at time  $t$ .  $T_1$  is called spin-lattice relaxation time, also called the longitudinal relaxation time. In a

metal the nuclear spin-lattice relaxation is often dominated by the scattering of conduction electrons. As a nuclear spin flips from quantum number  $m$  to  $m'$ , an electron is scattered from a state  $k$  and  $s$  into a state  $k'$  and  $s'$  in an energy conserving process.

Korringa<sup>21</sup> has shown the following relation:

$$T_1TK^2 = \left( \frac{\hbar}{4\pi k_B} \right) \left( \frac{\gamma_e}{\gamma_n} \right)^2 \quad (2.29)$$

where  $T_1$  is the spin-lattice relaxation time,  $T$  is the temperature,  $K$  is the Knight shift,  $\gamma_e$  and  $\gamma_n$  are the electron and nuclear gyromagnetic ratio.

A similar relation can also hold for the core polarisation interaction<sup>22</sup>:

$$T_{1cp}TK_{cp}^2 = \left( \frac{\hbar}{4\pi k_B} \right) \left( \frac{\gamma_e}{\gamma_n} \right)^2 B \quad (2.30)$$

where  $B$  is a factor of order unity. As Balakrishnan *et al*<sup>23</sup> point out the factor  $B$  depends on orbital character. For  $s$  orbitals,  $B$  is equal to one, for  $d$  orbitals,  $B$  varies from 2 to 5, for  $p$  orbitals,  $B$  is typically 3. However, the Korringa-like relation cannot hold for the orbital interaction, since  $K_{orb}$  is derived from a second order effect. The diagonal matrix elements of the orbital angular momentum are quenched, whereas the relaxation rate involves off-diagonal elements which are not quenched.

It needs to be noted here, if all of the three interactions (i.e. contact, core polarisation and orbital interactions) are important, then the relaxation rates from the three mechanism will add to produce the total relaxation rate, whereas the shifts may lead to cancellations, since  $K_{cp}$  will be negative, and  $K_{orb}$  will usually be small. Hence for the measured relaxation rate, the measure  $K$  value may be less than that predicted by equation (2.29).

### § 2.7.2 Spin-Spin relaxation ( $T_2$ )

If we treat the spin ensemble as a system, there must be a mechanism for transferring the energy from one spin to another in order to attain internal thermal equilibrium. In §2.4.1 we mentioned that the spin-spin interaction will lead to a broadening of the resonance line. The connection between line width and spin-spin interaction can be described by a spin-spin relaxation time  $T_2$ , which is a measure of how fast a spin system comes into equilibrium within itself.

Ordinarily in NMR, the spin-spin relaxation, also called the transverse relaxation, arises from one or both of two mechanisms<sup>24</sup>: (1) Nuclear spin-spin coupling (via the magnetic dipolar, as we mentioned in § 2.4.1, or indirect, interaction (exchange interaction § 2.4.4). (2) Spin-lattice relaxation. The first mechanism leads to relaxation curves which have a wide variety of time dependences for which in general it is not possible to find the exact theoretical form. Under certain circumstances the decay has a simple time dependence such as an exponential (for most liquid cases) or a Gaussian (for most solid cases). The second mechanism leads to an exponential decay with a time constant related to the spin-lattice relaxation by Redfield theory<sup>25</sup>. We denote this time constant as  $T_{2R}$ .

Another spin-spin relaxation time  $T_2^*$  not only depends on the spin-spin interaction but it also depends on the homogeneity of the magnetic field. We can write it as:

$$\frac{1}{T_2^*} = \frac{1}{T_2} + \gamma\Delta B_0 \quad (2.31)$$

where  $\gamma$  is gyromagnetic ratio.  $\Delta B_0$  is the field inhomogeneity.

## References

- 1 Slichter C.P., *Principles of magnetic Resonance*, Harper and Row (1963)
- 2 Abragam A., *Principles of Nuclear Magnetism*, OUP (1961)
- 3 Rushworth F.A., and Tunstall D.P., *Nuclear Magnetic Resonance*, Gordon and Breach (1973)
- 4 Winter J., *Magnetic Resonance in Metals*, OUP (1973)
- 5 Carter G.C., Bennett L.H., Kahan D. J., *Metallic shifts in NMR*, (Progress in materials science **vol 20**) (1977) Pergamon Press Ltd, UK.
- 6 Ruderman M.A. and Kittel C., *Phys. Rev.* **96** 99 (1953)
- 7 Feld B. and Lamb W.E., *Phys. Rev.* **67** 15 (1945)
- 8 See for example, Pennington C.H., and Slichter C.P., in *Physical Properties of High Temperature Superconductors*, **vol II**, Ed by Ginsberg D.M., Word Scientific 275-276 (1990)
- 9 Jones W.H. Jr, Graham T.P. and Barnes R.G., *Phys. Rev.* **132A** 1898 (1963)
- 10 Yosida K., *Phys. Rev.* **110**, 769 (1958)
- 11 Leggett A.J., *Rev. Mod. Phys.* **47**, 331 (1975)
- 12 MacLaughlin D.E., in *Solid State Physics*, **vol 31**, eds. by Ehrenreich H., Seitz F. and Turnbull D., Academic Press, New York, 1 (1976)
- 13 Fine H.L., Lipsicas M., and Strongin M., *Phys. Lett.* **29A**, 366 (1969)
- 14 MacLaughlin D.E., in *Solid State Physics*, **vol 31**, eds. by Ehrenreich H., Seitz F. and Turnbull D., Academic Press, New York, 1 (1976)
- 15 Abrikosov A.A., *Sov. Phys. JETP* **5**, 1174 (1957)

- 16 Fite W. and Redfield A.G., *Phys. Rev. Lett.* **17** 381 (1966); Redfield A.G., *Phys. Rev.* **162** 367 (1967)
- 17 Pincus P., Gossard A.C., Jaccarino V. and Wernick J.H., *Phys. Lett.* **13** 21 (1964)
- 18 Kleiner W.H., Roth L.M. and Autler S.H., *Phys. Rev.* **133**, A1226 (1964)
- 19 Brandt E.H., *J. Low Temp. Phys.* **73**, 355 (1989)
- 20 Song Y.-Q., Lee M., Halperin W.P., Tonge L.M., and Marks T.J., *Phys. Rev. B* **44** 914 (1991)
- 21 Korringa J., *Physica*, **16** 601 (1950)
- 22 Yafet Y. and Jacarino V., *Phys. Rev.* **133 A** 1630 (1964)
- 23 Balakrishnan G., Dupree R., Farnan I., McKPaul D. and Smith M.E., *J. Phys. C: Solid State Phys.* **21** L847 (1987)
- 24 Pennington C.H., Durand D.J., Slichter C.P., Rice J.P., Bukowski E.D. and Ginsberg D.M., *Phys. Rev. B* **39** 274 (1989)
- 25 Poole C.P. Jr. and Farach H.A., *Relaxation in Magnetic Resonance* Academic Press, New York, (1971)

## Chapter 3

# Experimental Techniques

### § 3.1 Introduction

During the past three years of this work, the main experimental technique used has been NMR. Nevertheless, many other experiments have also been done, *e.g.* A.C. susceptibility measurement, sample alignment, using X-ray diffraction and electron microscopy to characterise the degree of alignment of the samples.

### § 3.2 Pulsed NMR and Fourier Transform

#### § 3.2.1 Introduction

Because the results of this work use mostly the pulsed NMR technique, it is necessary to summarise some of its elementary features.

The technique is probably best described by the semi-classical treatment of precessing vectors. In a pulsed NMR experiment, there are two frames, namely, the laboratory frame ( $x, y, z$ ) and the rotating frame ( $x', y', z'$ ) shown in figure 3.1. It is usual to define the static applied magnetic field  $\mathbf{B}_0$  along  $z$ -axis and the oscillating rf magnetic field  $\mathbf{B}_1$  along  $x'$ -axis. Therefore, standing in the laboratory frame, there are two magnetic fields,  $\mathbf{B}_0$  along  $z$ -axis and  $\mathbf{B}_1$  rotating with frequency of  $\omega$  in the  $x$ - $y$  plane. Standing in the rotating frame, it can be seen that  $\mathbf{B}_0$  is along  $z'$ -axis and  $\mathbf{B}_1$  is now steady along the  $x'$ -axis. However, because now the sample with the nuclei is

rotating in  $x'$ - $y'$  plane with a frequency of  $-\omega$ , this turns out to be equivalent to an additional field  $\mathbf{B}' = -\omega/\gamma$  in opposing to  $\mathbf{B}_0$  direction. Therefore, the total magnetic field is usually defined as the effective field  $\mathbf{B}_{\text{eff}}$  (shown in Figure 3.2(a)) and is given by:

$$\mathbf{B}_{\text{eff}} = \mathbf{B}_0 + \mathbf{B}_1 + \mathbf{B}' = B_1 \mathbf{i}' + \frac{\omega_0 - \omega}{\gamma} \mathbf{k}' \quad (3.1)$$

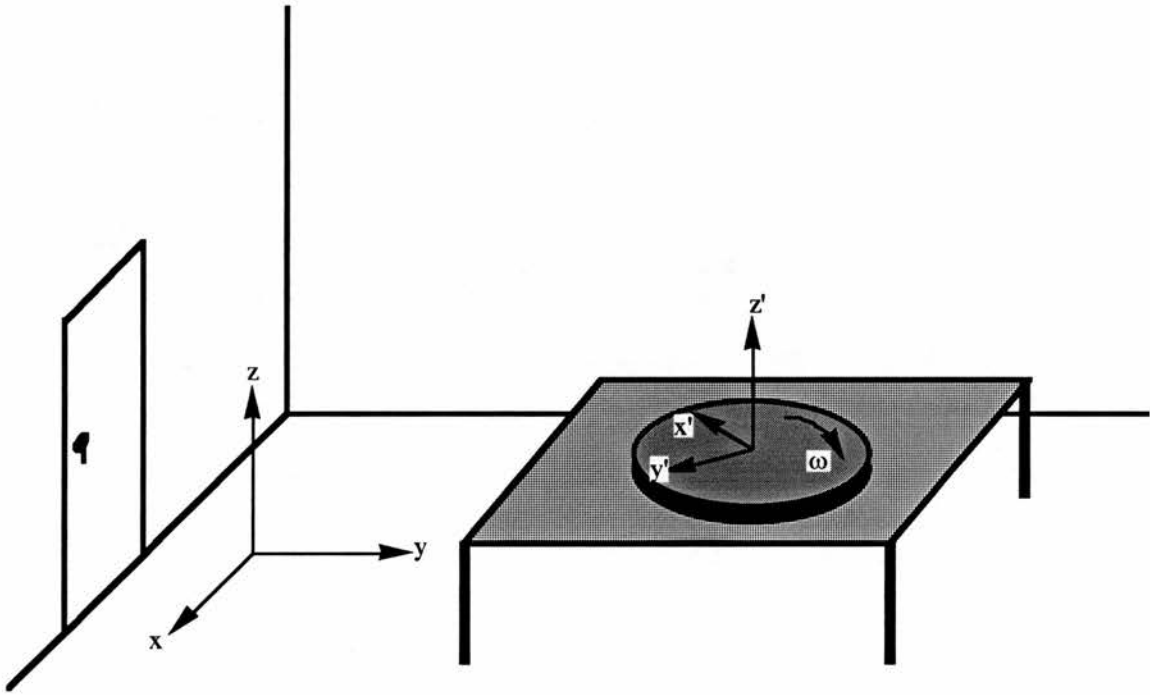


Figure 3.1 A comparison between the two frames (i.e. the laboratory frame  $(x, y, z)$  and the rotating frame  $(x', y', z')$ ).

If  $\omega_0 = \omega$ , then  $\mathbf{B}_{\text{eff}} = B_1 \mathbf{i}'$  (shown in Figure 3.2(b)). If  $\mathbf{B}_1$  is a pulsed signal, and at  $t=0$   $\mathbf{B}_1$  is turned on, then the magnetization  $\mathbf{M}$  will rotate in  $y'$ - $z'$  plane at a frequency of  $\omega_1 = \gamma B_1$ . After  $t_p$ , called the pulse width or pulse length,  $\mathbf{B}_1$  is turned off. At this moment, the magnetization vector  $\mathbf{M}$  will have been tipped through an angle  $\theta$  given by:

$$\theta = \omega_1 t_p = \gamma B_1 t_p \quad (3.2)$$

Typically,  $t_p$  is adjusted so that the angle  $\theta$  is  $90^\circ$  ( $\pi/2$ ) or  $180^\circ$  ( $\pi$ ) and the pulse is called  $90^\circ$  ( $\pi/2$ ) or  $180^\circ$  ( $\pi$ ) pulse, respectively.

After the rf field  $\mathbf{B}_1$  is turned off, the magnetisation will precess freely. In a coil with its axis perpendicular to the applied magnetic field  $\mathbf{B}$ , this decaying magnetisation will induce an rf current at the Larmor frequency in complete analogy with an electrical generator. This signal induced in the coil is a free precession signal and, owing to its decay, is called a free induction decay (FID) shown in Figure 3.3(a). Figure 3.4 shows what happens to a typical assembly of spins when such a pulse is applied, with  $\mathbf{B}_1$  in the  $x'$  direction.

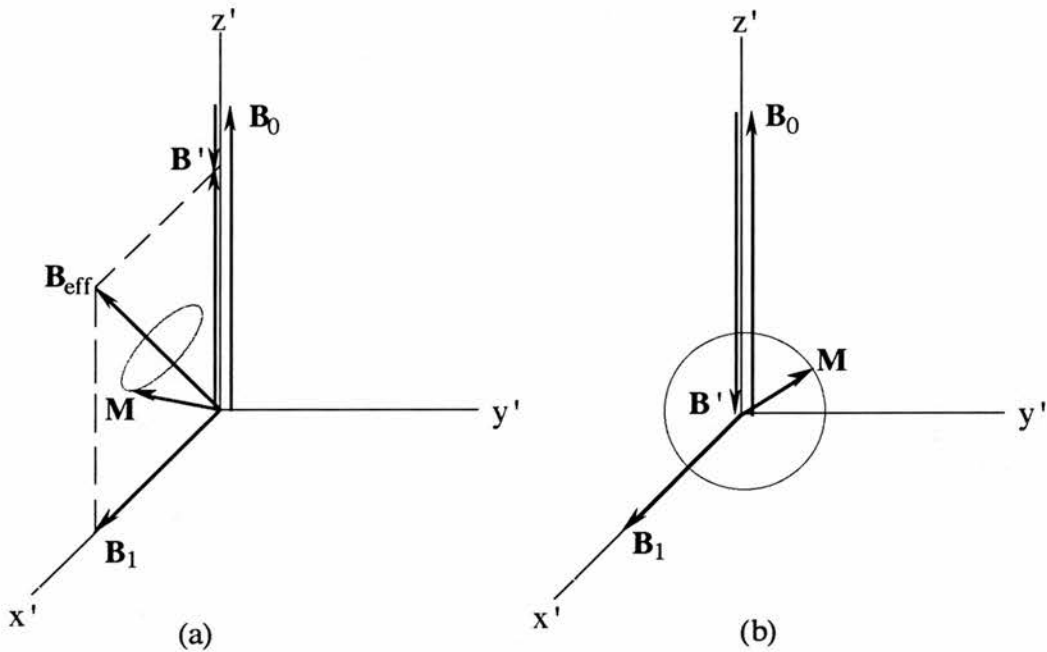


Figure 3.2 In the rotating frame, the magnetisation  $\mathbf{M}$  precesses around a  $\mathbf{B}_{\text{eff}}$  fields. (a)  $\omega < |\gamma\mathbf{B}_0|$  (b)  $\omega = |\gamma\mathbf{B}_0|$  and so then  $\mathbf{B}_{\text{eff}} = \mathbf{B}_1$ .  $\mathbf{M}$  traces out a disc in the  $y'$ - $z'$  plane.

## § 3.2.2 Introduction to Fourier Transform (FT)

Generally, there are two representations for a wave. One is an amplitude versus time. Another one is an amplitude versus frequency. And these two representations contain the same information and can be transformed into each other by a mathematical technique called a Fourier transform (FT) represented by:

$$A(t) = \frac{1}{2\pi} \int_{-\infty}^{+\infty} A(\omega) e^{i\omega t} d\omega \quad (3.3)$$

$$A(\omega) = \int_{-\infty}^{+\infty} A(t) e^{-i\omega t} dt \quad (3.4)$$

Lowe and Norberg<sup>1</sup> were the first to have shown that the Fourier transform of the FID, after a 90° pulse, was identical to the steady state spectrum. Later it was pioneered experimentally by Clark<sup>2</sup> in 1964 and by Ernst and Anderson<sup>3</sup> in 1966. Figure 3.3 shows the typical FID signal and its Fourier transformation.

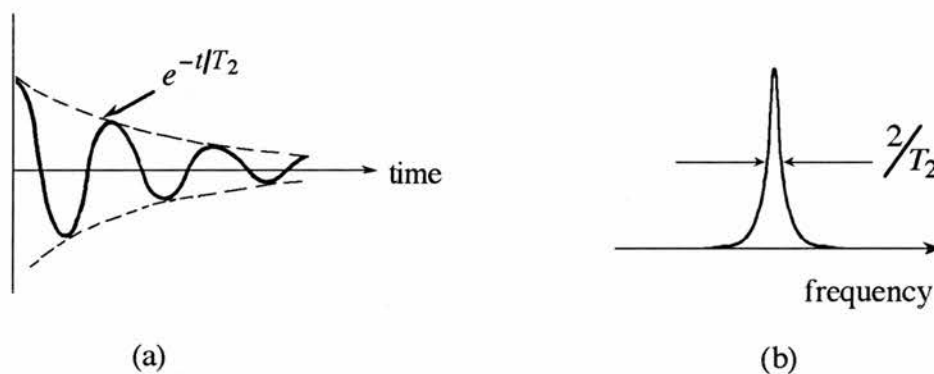


Figure 3.3 (a) A typical free induction decay (FID) signal . (b) its Fourier transformation. (After Fukushima and Roeder<sup>4</sup>)

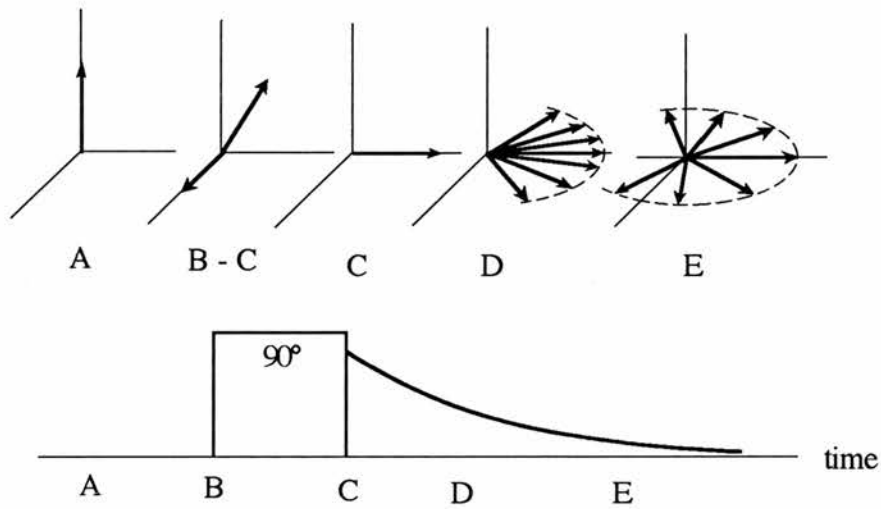


Figure 3.4 *Diagram of behaviour of spin isochromats under action of  $90^\circ$  pulse with  $\mathbf{B}_1$  in  $x'$  direction. (After Rushworth and Tunstall <sup>5</sup>)*

### § 3.2.3 The Spin Echo Technique

The spin echo technique was discovered by Hahn<sup>6</sup> in 1950. Suppose that a  $90^\circ$  pulse is applied along  $x'$  at time  $t=0$  to a spin system, shortly thereafter, the spin isochromats will have dephased in the  $x'$ - $y'$  plane. As a result, there is no net magnetization component in the  $x'$ - $y'$  plane, although the individual spin isochromats have not yet dephased (see Figure 3.4). Suppose at a time  $t = \tau$ , a  $180^\circ$  pulse is applied along the  $x'$ -axis. Any magnetization along  $z'$  direction would therefore simply be inverted to the  $-z'$  direction and be of no consequence. Of the magnetisation remaining in the  $x'$ - $y'$  plane each one of the spin isochromats would be rotated  $180^\circ$  about the  $x'$ -axis. As a consequence, those spin isochromats which had got ahead of the average spin isochromats by a certain angle are now behind the average of the pack of spin isochromats by the same amount. Similarly those spin isochromats which were going

slower than average are now ahead of the average. Therefore, following the  $180^\circ$  pulse, the spin isochromats begin to rephase to form a net magnetisation as the rapid isochromats catch up with the slow ones. The result is that the magnetisation becomes refocussed along the  $-y'$  axis at time  $t=2\tau$ , and it will cause an inverted spin echo. The spin echo consists of two FID's back-to-back. It is possible to obtain spin echoes by applying  $180^\circ$  pulse taken place along the  $y'$ -axis so the echo will be have the same sign as the FID shown in Figure 3.5

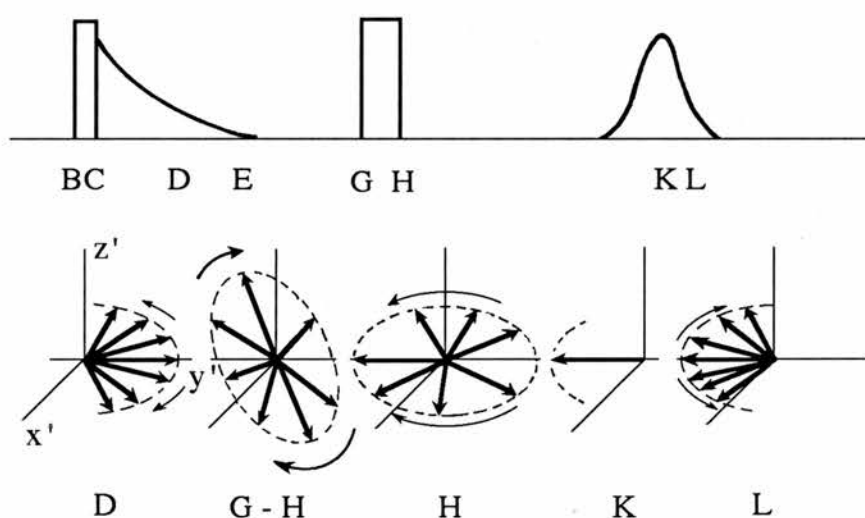


Figure 3.5 *Formation of spin-echo from  $90^\circ - \tau - 180^\circ$  pulse sequence (After Rushworth and Tunstall <sup>5</sup>)*

## § 3.3 The NMR Spectrometer

### § 3.3.1 General Spectrometer

In general, a pulsed NMR spectrometer basically involves the following main parts (shown in Figure 3.6):

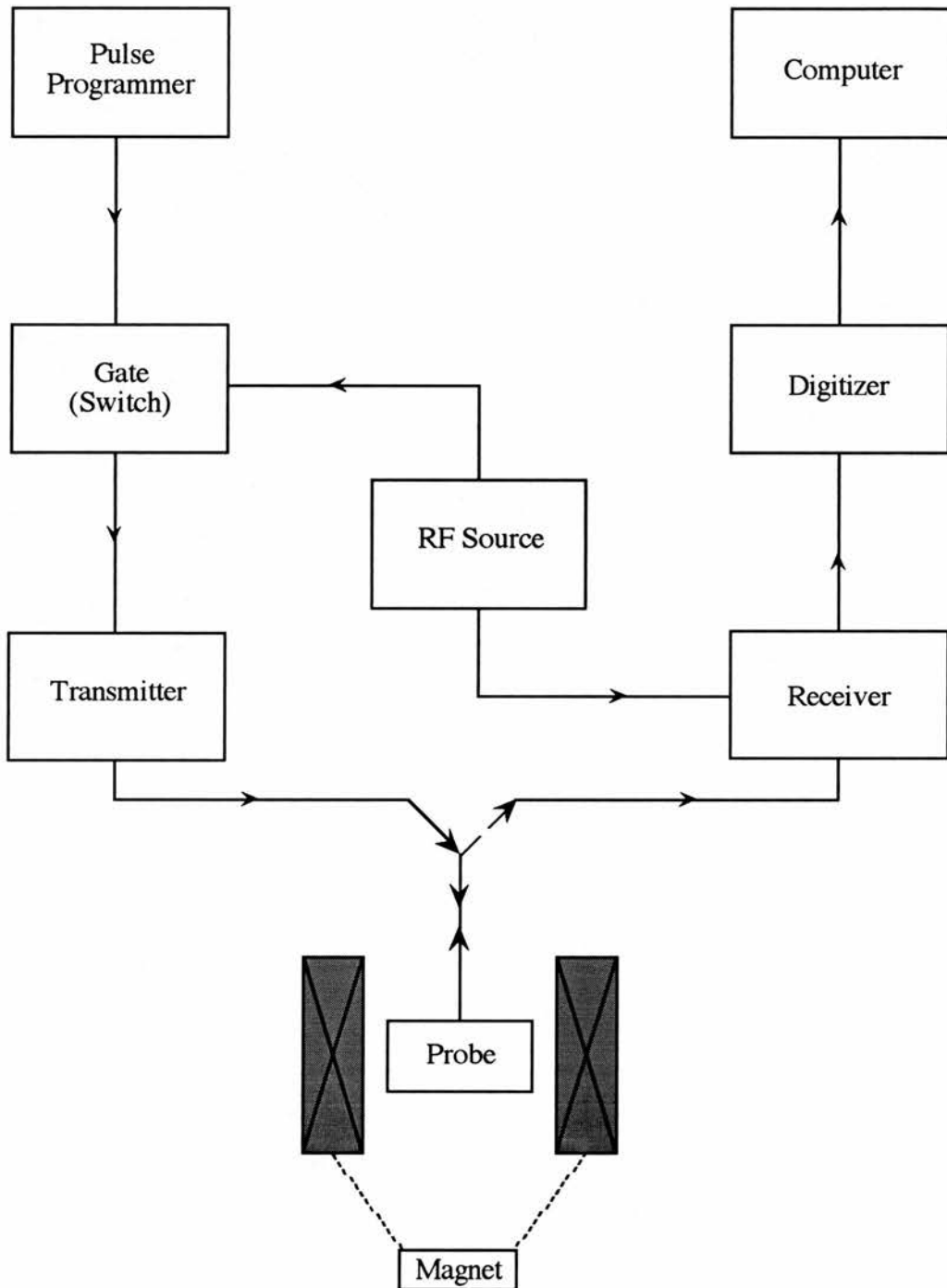


Figure 3.6 A schematic of a modern pulsed NMR spectrometer.

- i) Rf source: providing a reference frequency to receiver and carrying pulses.
- ii) Pulse programmer: used for timing and providing the stable pulses. It switches the gate on or off by sending the control pulses to the transmitter.
- iii) Transmitter: amplifying the radio frequency signal before applying it to the transmitter coil inside the probe.
- iv) Probe: situated inside the magnet and having the parts required for variable temperature experiments. It contains the coil which can make both excitation and detection of an NMR signal.
- v) Magnet: providing a homogeneous high magnetic field  $B_0$ . It is now normally built by a superconducting coil.
- vi) Receiver: detecting and amplifying the signal.
- vii) Digitiser: collecting signal and translating to readable data by computer.
- viii) Computer or Scope: displaying signal, analysing data, maybe also controlling system process.

### § 3.3.2 The Bruker MSL-500 spectrometer

In this work the yttrium-89 copper-63 and lead-207 NMR were performed using a Bruker MSL-500 spectrometer together with an 11.74 Tesla Oxford Instruments wide bore (89mm) superconducting cryomagnet. The copper NQR experiments were also performed using the Bruker MSL-500 spectrometer, however, with no magnetic field.

The spectrometer is managed by the Aspect-3000 computer which allows simultaneous data acquisition and data manipulation using the DISMSL software. An onboard system process controller (SPC) manages the transmitter and receivers and can

be programmed (using a highly structured Bruker Specific Programming Language) to perform any form of complex pulse routine.

The spectrometer is capable of performing pulse NMR spectroscopy over a continuous frequency range of 17 to 215 MHz (low frequency transmitter) and at a proton frequency of 500 MHz (proton frequency transmitter). The continuous low frequencies are generated by a frequency synthesiser with a resolution of 1 Hz. Pulses are produced by the SPC via an RF interface. Further details of the spectrometer and its operation and magnet design can be found in the Bruker reference manual<sup>7,8</sup> and in the Oxford Instruments manual.<sup>9</sup>

### § 3.3.3 The Low Temperature Spectrometer

The thallium NMR was performed using a home built spectrometer. The configuration of this spectrometer is same as that represented in Figure 3.6, with a coil system based on the single coil series resonant circuit of Clark and McNeil<sup>10</sup> (1973). For more detailed information about the spectrometer and the probe, the reader is referred to Webster.<sup>11</sup>

## § 3.4 NMR and NQR Measurements

### § 3.4.1 Yttrium-89 NMR

#### §3.4.1.1 Magnetic Shift Measurement

The yttrium NMR was performed on the Bruker MSL-500 spectrometer at a frequency of 24.506 MHz with the constant magnetic field of 11.74 Tesla. A simple pulse sequence called QUADCYCL.PC was used shown in Figure 3.7. After 5  $\mu$ s (microsecond) a 90° pulse is started with a pulse length D1 of typically 12  $\mu$ s. After the

pulse is applied, waiting for D3 (normally 30  $\mu$ s), then the data collection is started. D0, the time length between the end of data collecting and beginning of next pulse sequence, is typically 20 s (second). Before starting acquisition all the parameters should be set. e.g. SW (spectral width), TD(number of data points), SI(size of data), NS (number of scans), D0, D1, D3 and so on.

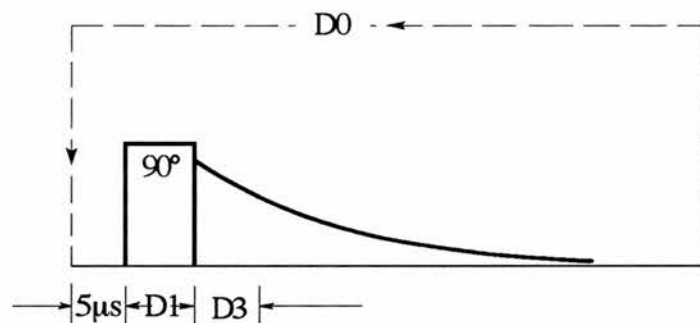


Figure 3.7 *QUADCYCL.PC pulse sequence.*

After the acquisition finishes, the collected data is saved and processing of the data is typically as follows: i) LS (left shift) to remove the dead time of the FID if necessary, ii) reset TD (typically 150W), SI (16K), iii) FT (Fourier transform), iv) under the EP (expand and phase correction) mode to do the phase and baseline correction. The frequency dependent spectrum is then plotted. In order to obtain an accurate measure of the shift, the shift in a 1 molar  $YCl_3$  solution is measured at 24.506 MHz at room temperature. The temperature range for yttrium NMR was 160K ~ 293K (room temperature).

#### § 3.4.1.2 Spin-lattice Relaxation Time ( $T_1$ ) Measurements

The yttrium spin-lattice relaxation time ( $T_1$ ) measurement used a pulse program is called "SATREC.PC", standing for used saturation recovery. The first part of this pulse sequence is a saturating 'comb' of 90° pulses (or close to 90°) with a spacing D20, the time between the adjacent two pulses, of the order of  $T_2$  typically 5 ms (millisecond).

C1 the number of the pulses is at least tens, even up to hundreds. The intention of using this comb is to reduce the nuclear magnetisation of the sample to zero. The remaining parts of this pulse sequence are a time delay VD (variable delay) and a  $90^\circ$  pulse sequence same as last section shown in Figure 3.8. Successive experiments are performed with different VD delays which may be set from 1s to 100s by 'VDlist.001'. A program called TONEAQ.AUM is used to run this experiment and automatically change VD and store the series data files. NE (number of experiments) is set for how many experiments to run which depends on how many different VDs there are in the VDlist. To start the experiment, one uses the command AU (execute automation program). After the acquisition finishes, all the data are automatically saved in the computer. The data processing is similar to the last section. One should however remember that in order to obtain comparable data, before the processing, the AI (absolute intensity mode) flag should be set to 1.

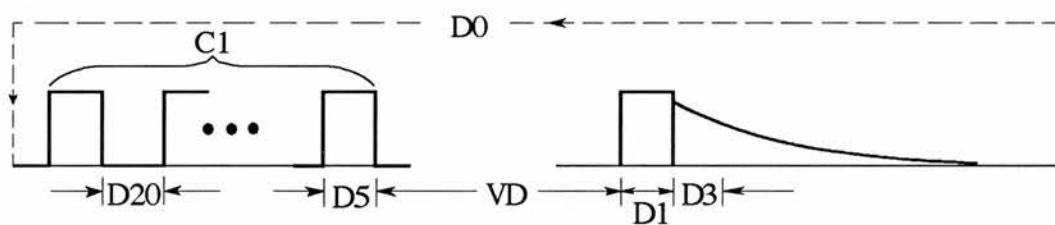


Figure 3.8 *SATREC.PC pulse sequence.*

## § 3.4.2 Copper-63 and Lead-207 NMR and Copper-63 NQR

### § 3.4.2.1 Frequency Spectra Measurements

Since the  $^{63}\text{Cu}$  NMR and NQR, and  $^{207}\text{Pb}$  NMR spectra observed were very broad, the resulting FID from a one pulse experiment (like § 3.4.1.1) would be very short with much signal being lost in the dead time from the probe. In order to solve the problem, a spin-echo pulses sequence called SAM1ECHO.PC is used to acquire the

broad spectra. In § 3.2.3, we have described the spin-echo techniques. Here, we represent the spin-echo pulse sequence and with the certain conditions for each experiment. After 2  $\mu\text{s}$ , the first  $90^\circ$  pulse is applied with a pulse length D1 of 5  $\mu\text{s}$ . The time between the first pulse and the second pulse is D6. Because the spin-spin relaxation time  $T_2$  is very short for Copper NMR and NQR (only order of tens of microseconds), the signal falls off rapidly after the pulses. To obtain a better signal and to ensure observation of, as closely as possible, an undecayed signal, D6 should be chosen as short as possible (in our experiments, D6 is 10  $\mu\text{s}$  for Cu NMR and 15  $\mu\text{s}$  for Cu NQR. Even with D6 short, an allowance for decay during D6 may be necessary). Because the  $T_2$  for Pb NMR is quite long (order of hundreds of microseconds), it is possible to set D6 for Pb NMR around 40  $\mu\text{s}$ . After D6, the second pulse ( $180^\circ$ ) is applied with a pulse length of  $D2 = 2D1 = 10 \mu\text{s}$ . Following D3 and D8, the data collection is then started. D8 is usually equal to D6. In order to start collecting data exactly from the peak of the echo *i.e.* to obtain a complete FID signal from the echo, therefore,  $\frac{1}{2}D1 + D6 + \frac{1}{2}D2 = \frac{1}{2}D2 + D3 + D8$  and so  $D3 = \frac{1}{2}D1 = 2.5\mu\text{s}$ . Figure 3.9 shows the pulse sequence. D0 as defined in the last section was set to 5 ms for all Cu NMR and NQR and Pb NMR experiments. Other parameters were set as following: TD = 500W, SI = 1K, NS = 30000, SW =  $2.5 \times 10^6$ . Before starting acquisition, the frequency should be set by command SF and then the probe should be tuned under the TUNE mode. To start acquisition, one uses the command ZG (zero memory and go). After acquisition finishes, the data is stored by WR (write data to disk). Then SF (set another frequency) and TUNE and ZG (start next acquisition).

Before data processing, the AI flag should be set to 1. In this work, we used a data file as reference file and set its echo area to 100. For all Cu NMR and NQR and Pb NMR, we used the same reference data. The data processing is similar to the Yttrium NMR in the last section. However, LS is now unnecessary and TD is set to 200W, SI to 8K. After FT, EP, phase and baseline correction the signal is then integrated and the

echo area is recorded. A frequency spectrum is constructed for each sample by performing a point by point frequency sweep throughout the spectral region of interest and acquiring a spin echo signal at each frequency. The step of frequency is 100 KHz for Cu NMR, 5 ~ 20 KHz for Pb NMR and 500 KHz for Cu NQR.

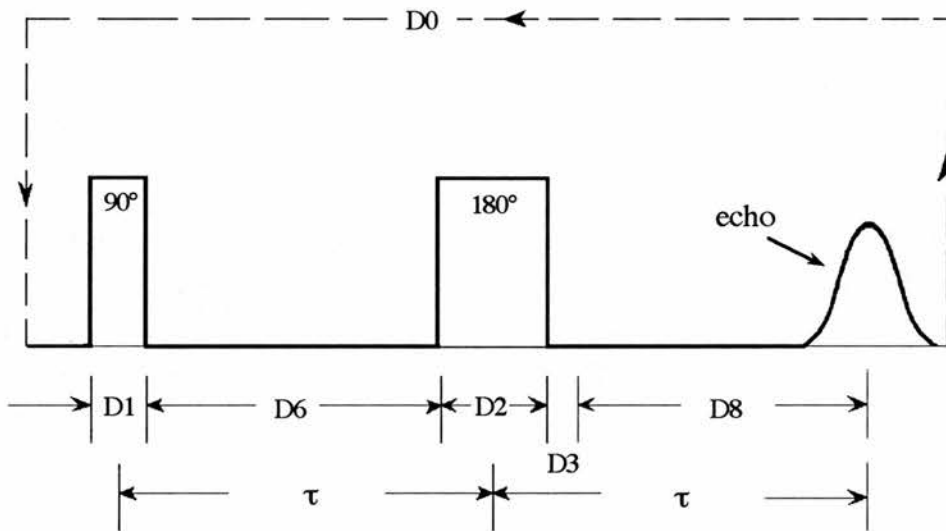


Figure 3.9 SAM1ECHO.PC pulses sequence.

#### § 3.4.2.2 $T_1$ Measurements

The pulse program for measuring the spin-lattice relaxation time  $T_1$  for copper, lead NMR and copper NQR is modified from SAM1ECHO.PC program by simply adding a saturating comb of  $90^\circ$  pulses similar to § 3.4.1.2 shown in Figure 3.10 called XDNMRT1.PC and XDT1NQR.PC, respectively.

#### § 3.4.2.3 $T_2$ Measurements

The pulse program for spin-spin relaxation time  $T_2$  measurements is also modified from SAM1ECHO.PC program by only changing  $D_6$  and  $D_8$  to VD called

XDT2TEST.PC and XDT2NQR.PC for NMR and NQR respectively. Using VDlist and automatic program TONEAQ.AUM to run it is similar to § 3.4.1.2.

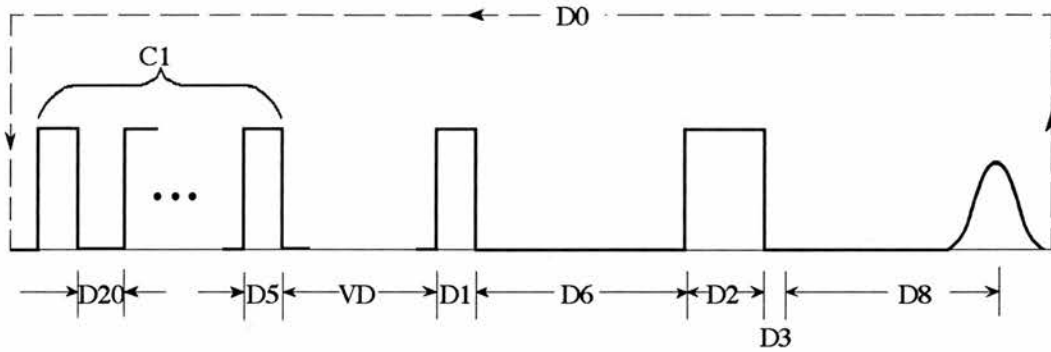


Figure 3.10 *Pulse sequence for measuring  $T_1$  modified from SAMIECHO.PC.*

#### § 3.4.2.4 Difference Between NMR and NQR Measurements

Although the pulse sequence and the parameters could be same for both NMR and NQR experiments, because the NQR measurement is performed with no magnetic field, the magnetisation precession is different between NMR and NQR. Therefore, one should be careful to choose the directions of the applied pulse magnetic field and data collection. Table 3.1 shows the phase listing for NMR and NQR.

**Table 3.1** *The difference between NMR and NQR in phase programming for data collection.*

	NMR	NQR
PLS1*	+X +X +X +X	+X +X +X +X
PLS2**	+X +Y -X -Y	+X +Y -X -Y
RLS‡	-Y +Y -Y +Y	+X -X +X -X

\* the first pulse, \*\* the second pulse, ‡ data collection

### § 3.4.3 Thallium NMR Measurements

Since the thallium nuclear gyromagnetic ratio  $\gamma$  is quite high ( $^{203}\gamma = 24.33$  MHz/Tesla and  $^{205}\gamma = 24.57$  MHz/Tesla for the bare nucleus), if thallium NMR was performed at 11.74 Tesla, the resonance frequency would be around 290 MHz which is out of scale for the MSL-500 spectrometer. Therefore, we performed thallium NMR using a home-built spectrometer mentioned in § 3.3.3.

The NMR spectra were obtained at 1.5 K and a constant frequency of 141.0 MHz by sweeping the magnetic field and measuring the spin-echo amplitude. A  $90^\circ$ - $\tau$ - $90^\circ$  pulse sequence was used with a pulse width of 2  $\mu$ s and separation time  $\tau$  of 20  $\mu$ s. In order to improve the signal to noise, the successive echo signals were acquired and averaged 2048 times on the Digitising Oscilloscope<sup>12</sup>. In general, the signal to noise ratio was about 10:1. The repetition rate was 6.25Hz (or one pulse sequence took 0.16 s).

### § 3.5 Sample Preparation and Alignment Procedure

All of the samples were prepared by Dr. Ru-Shi Liu<sup>13</sup> at the Interdisciplinary Research Centre (IRC), University of Cambridge. All samples were prepared by solid state reaction. High purity  $\text{CaCO}_3$ ,  $\text{Y}_2\text{O}_3$ ,  $\text{SrCO}_3$  and  $\text{CuO}$  powders were calcined in the appropriate stoichiometric proportions at 970 °C, ground and pressed into a cylindrical pellet, 10mm in diameter and 2mm in thickness, under a pressure of 2 ton/cm<sup>2</sup>. The pellets were then wrapped in gold foil to prevent loss of thallium and lead during the heating. The samples were the sintered at 950 °C for 3h in flowing oxygen followed by cooling to room temperature at a rate of 5 °C/min. Full details can be obtained in ref. (13).

In order to obtain better NMR and NQR results, an attempt was made to align the samples. The alignment procedure was the following, samples were ground into very fine powders (mean particle size  $5\mu\text{m}$ ). We then mixed fixed amounts of powders with Stycast (in a proportion by volume of 10% powder to 90% Stycast). The mixtures were shaken with an ultrasonic drill for about 2 minutes and then allowed to set in a magnetic field of 8 Tesla for about 15 hours at a temperature of approximately 320 K.

### 3.6 Characterisation of Alignment by X-ray Diffraction

After the alignment procedure, the samples were taken to check the alignment by X-ray diffraction. The aligned samples were sliced to a 1 mm thick disc from the end of the cylinders. Therefore, the c-axis alignment was in the plane, perpendicular to the plane of the X-ray beam. The room temperature X-ray diffraction studies were performed on the Philips PW 1049 X-ray diffractometer using a copper target  $\text{CuK}\alpha$  radiation with a wavelength  $\lambda$  of  $1.54050 \text{ \AA}$ . The  $\text{CuK}\beta$  radiation was eliminated by a nickel filter in the diffraction beam. X-rays were fired through a  $1^\circ$  divergence slit and irradiated the sample on one side. With this experimental arrangement, diffracted rays leave the specimen along the generators of cones concentric with the original beam. The generators make an angle of  $2\theta$  between  $5^\circ$  and  $90^\circ$ , with a step size of  $0.02^\circ$ .

In order to identify the peaks, experimental values of  $2\theta$  were compared with the computer generated tables of theoretical  $2\theta$  values. For the  $(\text{Tl}_{0.5}\text{Pb}_{0.5})\text{Sr}_2(\text{Y}_y\text{Ca}_{1-y})\text{Cu}_2\text{O}_7$  system, all the structures are tetragonal. From Ladd and Palmer<sup>14</sup>, the interplanar spacing,  $d_{hkl}$ , for a specified plane  $(hkl)$  can be represented in terms of the crystal lattice parameters  $a$ ,  $b$ , and  $c$  ( $a = b \neq c$ ):

$$d_{hkl} = \frac{a}{\sqrt{h^2 + k^2 + \left(\frac{al}{c}\right)^2}} \quad (3.5)$$

using this equation and Bragg's law<sup>15</sup>,

$$\lambda = \frac{2d_{hkl}}{n} \sin \theta \quad (3.6)$$

the spectra produced from the X-ray equipment can be analysed. More details about the computer program and X-ray data analysing can be found in ref.(11).

## § 3.7 A.C. Susceptibility Measurements

### § 3.7.1 A.C. Susceptibility Measurements

A.C. susceptibility is a method used to study the magnetic properties of materials. Using this method to study superconductors, the critical temperature,  $T_c$ , can be determined and the volume fraction can also be studied.

The basis of A.C. susceptibility is to measure the effect of the sample on the magnetic flux within a sensing coil placed around the specimen. This is achieved by applying a small A.C. magnetic field of a constant amplitude to the sample and monitoring the induced voltage in the coil. Figure 3.11(a) shows the basic schematic diagram of the A.C. susceptometer. The mutual inductance bridge (made by Oxford Instruments) can be used for precise measurements of mutual inductance over a large of values, from a few nH up to 1H. The bridge frequency is 119Hz. The sense coil is wound in series opposition with an identical, sample free coil to simplify interpretation of detected signal shown in Figure 3.11(b). In this case the induced voltage from the two coils cancel when the susceptibility of their cores is identical. A net signal, directly proportional to the sample susceptibility, therefore, is only observed when one coil contains a sample of either para or diamagnetic character.

### § 3.7.2 Temperature Controller and Measurement

The A.C.Susceptibility measurements were performed in the CF 1200 Cryostat (made by Oxford Instruments). The temperature can be continuously controlled in a range of 3.8 K to 500 K by an Intelligent Temperature controller ITC4 (made by Oxford Instruments).

In order to obtain a more accurate evaluation of the temperature on the sample, the temperature was measured at two points besides the sample. As Figure 3.12 shows, the temperature sensor is placed at the L point at which the temperature is measured by ITC4. The sample is placed at the M point. Because there is always a temperature gradient in the cryostat, a one point measurement could not obtain the exact temperature on the sample. A diode is therefore placed at the N point to measure the temperature. The temperature versus the voltage was calibrated by Dr D P Tunstall, and is shown in Figure 3.13. Assuming that  $T_L$ ,  $T_M$ ,  $T_N$  are the temperature of L, M, N points, respectively, and the temperature gradient is linear, a good approximation to the temperature  $T_M$  should be:

$$T_M = \frac{(x \times T_L + y \times T_N)}{x + y} \quad (3.7)$$

where  $x$ ,  $y$  are the distances between L and M, M and N respectively.

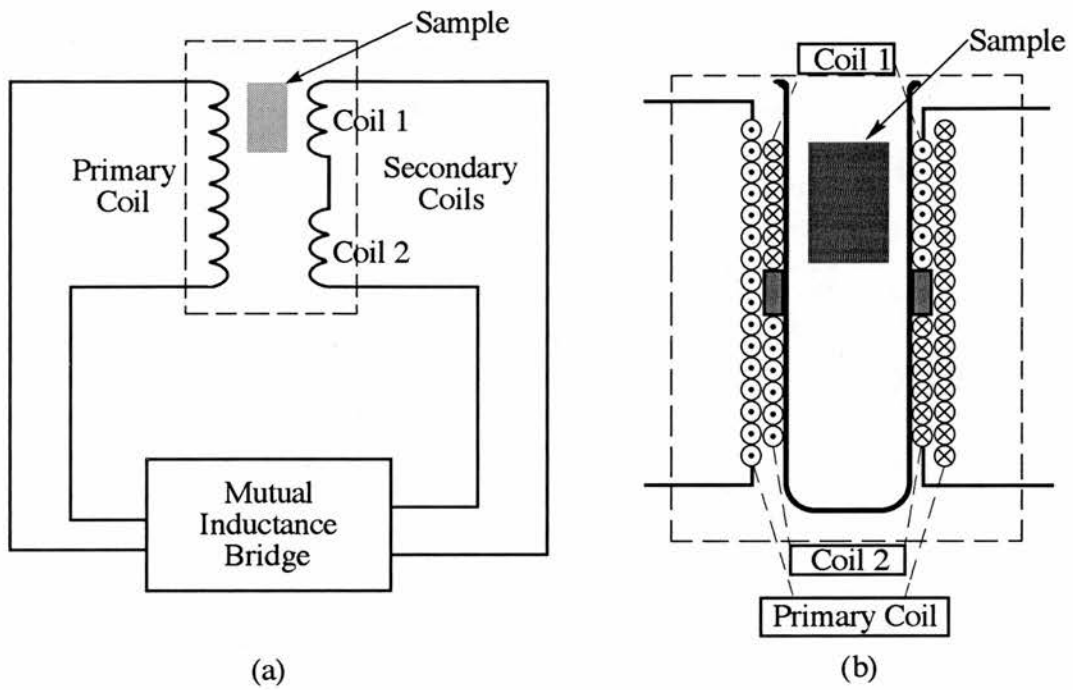


Figure 3.11 (a) *The basic schematic diagram of the A.C. susceptometer.* (b) *Cross-section of primary and secondary coils of the A.C. susceptibility.*

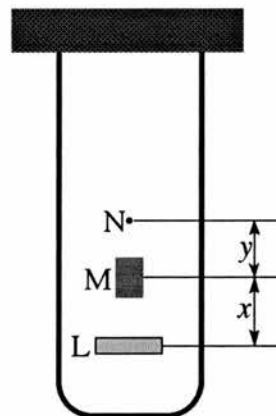


Figure 3.12 *Schematic diagram of the cryostat.*

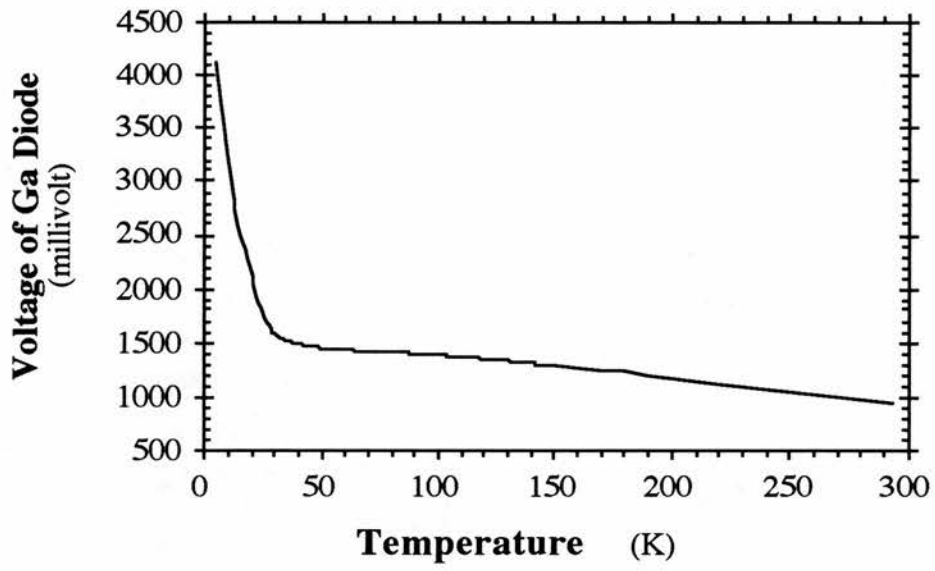


Figure 3.13 *The calibration of the Ga diode versus temperature (Dr. D P Tunstall).*

## References

- 1 Lowe I.J. and Norberg R.E., *Phys. Rev.* **107** 46 (1957)
- 2 Clark W.G., *Rev. Sci. Instr.* **35** 316 (1964)
- 3 Ernst R.R., and Anderson W.A., *Rev. Sci. Instr.* **37** 93 (1966)
- 4 Fukushima E., and Roeder S.B.W., *Experimental Pulse NMR*, Addison-Wesley, (1981)
- 5 Rushworth F.A., and Tunstall D.P., *Nuclear Magnetic Resonance*, Gordon and Breach (1973)
- 6 Hahn E.L., *Phys. Rev.* **80** 580 (1950)
- 7 Aspect 3000 System Software Manual, Bruker (1989)
- 8 Aspect 3000 MSL (CXP) Software Manual, Bruker (1989)
- 9 500/89 Superconducting Magnet System, Oxford Instruments (1989)
- 10 Clark W.G., and McNeil J.A., *Rev. Sci. Instr.* **44** 844 (1973)
- 11 Webster W.J., *PhD Thesis*, St. Andrews University, UK. (1993)
- 12 HEWLETT PACKARD 54502A 400 MHz 400 MSa/s Digitising Oscilloscope.
- 13 Liu R.S., *PhD Thesis*, Cambridge University, UK. (1992)
- 14 Ladd M.F.C., and Palmer R.A., *Structure Determination by X-ray Crystallography*, Plenum (1979)
- 15 Bragg W.L., *Proc. Cambridge Phil. Soc.* **17** 43 (1913)

## Chapter 4

# The $(\text{Tl}_{0.5}\text{Pb}_{0.5})\text{Sr}_2(\text{Y}_y\text{Ca}_{1-y})\text{Cu}_2\text{O}_{7-\delta}$ System

### § 4.1 Introduction

The septenary Tl-1212 system,  $(\text{Tl}_{0.5}\text{Pb}_{0.5})\text{Sr}_2(\text{Y}_y\text{Ca}_{1-y})\text{Cu}_2\text{O}_{7-\delta}$ , which has been studied in the present work, was made by Dr. R-S Liu in IRC at the University of Cambridge, and has been studied using a wide variety of techniques by the group at the IRC. The studies include X-ray and neutron diffraction, Hall effect, thermopower, magnetoresistance, resistivity, electron energy loss, specific heat and magnetisation measurements<sup>1</sup>. In order to understand this work more easily, we think it is worthwhile to present those of Liu's results that are, in particular, relevant to this work, in this chapter. Most of the results in this chapter are taken from ref. (1).

Because there are not many published NMR papers on this system, in order to help us to analyse our experimental results, we contrast this system to the best known  $\text{YBa}_2\text{Cu}_3\text{O}_{7-\delta}$  system. Therefore, some of Liu's results are also compared with the  $\text{YBa}_2\text{Cu}_3\text{O}_{7-\delta}$  system in this chapter.

### § 4.2 Introduction to the Tl-1212 System

#### § 4.2.1 General Introduction

As mentioned in Chapter 1, after the 30 K LaBaCuO superconductor was first

discovered by Bednorz and Muller<sup>2</sup>, a number of cuprate superconducting systems were discovered including YBaCuO, the first system with  $T_c$  above liquid nitrogen temperature<sup>3</sup>, BiSrCaCuO, the first system with  $T_c$  above 100 K<sup>4</sup>, and TlBaCaCuO, the system with the highest reproducible  $T_c$  above 120 K<sup>5,6</sup>.

In the Tl-based system, two series of superconducting phases, double TlO-layer  $Tl_2Ba_2Ca_{n-1}Cu_nO_{2n+4}$ <sup>7,8,9</sup> and single TlO-layer  $TlBa_2Ca_{n-1}Cu_nO_{2n+3}$ <sup>10,11</sup>, were rapidly identified. The formula with  $n=2$  in the series of single TlO-layer,  $TlBa_2CaCu_2O_7$  has been widely called the Tl-1212 phase. The TlSrCaCuO system was discovered by Sheng *et al.*<sup>12</sup> and Nagashima *et al.*<sup>13</sup>. Based on this phase a number of groups have attempted to increase the critical temperature  $T_c$  via chemical substitution, for instance, with the substitution of Pb<sup>14,15,16</sup> or Bi<sup>17,18</sup> in Tl site, or rare-earth elements (La, Nd, and Y) in the Ca sites<sup>19,20</sup> in the  $TlSr_2CaCu_2O_7$ . In particular, Liu and his coworkers systematically investigated the  $(Tl_{1-x}Pb_x)Sr_2(Y_yCa_{1-y})Cu_2O_{7-\delta}$  system.<sup>21,22,23,24</sup>

#### § 4.2.2 Metal-Superconductor-Insulator Transition in

##### $(Tl_{1-x}Pb_x)Sr_2(Y_yCa_{1-y})Cu_2O_{7-\delta}$ System

The compound  $TlSr_2CaCu_2O_7$  is itself a metal, but exhibits no superconductivity at temperatures down to 4 K. The oxide can be converted to a superconductor by replacing some of  $Ca^{2+}$  with yttrium ions.  $Y^{3+}$  ions raise the reduction state of the structure without distorting it (diameters:  $Y^{3+}=188$  picometers,  $Ca^{2+}=198$  picometers). When approximately two-thirds of the  $Ca^{2+}$  ions are replaced by  $Y^{3+}$ , then a critical temperature,  $T_c$  of 78 K is obtained. Adding more yttrium only makes the  $T_c$  fall again.

The same behaviour can be found when the thallium ions ( $Tl^{3+}$ ) in the starting compound,  $TlSr_2CaCu_2O_7$ , are replaced by lead ( $Pb^{4+}$ ). The critical temperature again reaches a maximum of 78 K, when exactly half  $Tl^{3+}$  of the ions have been replaced by  $Pb^{4+}$  ions.

What happens if one takes this new compound,  $(\text{Tl}_{0.5}\text{Pb}_{0.5})\text{Sr}_2\text{CaCu}_2\text{O}_7$ , and start replacing the Ca ions with Y ions as before? The  $T_c$  increases dramatically, rising to peak of 108 K when one fifth of the Ca ions are exchanged for Y ions. The ‘magic’ formula is  $(\text{Tl}_{0.5}\text{Pb}_{0.5})\text{Sr}_2(\text{Y}_{0.2}\text{Ca}_{0.8})\text{Cu}_2\text{O}_7$ . Again, if more Y ions are added then the  $T_c$  drops rapidly. When two-thirds of the calcium ions had been replaced the superconductivity disappeared altogether. Figure 4.1 shows the phase diagram for the Metal-Superconductor-Insulator,  $(\text{Tl}_{1-x}\text{Pb}_x)\text{Sr}_2(\text{Y}_y\text{Ca}_{1-y})\text{Cu}_2\text{O}_{7-\delta}$ , system.

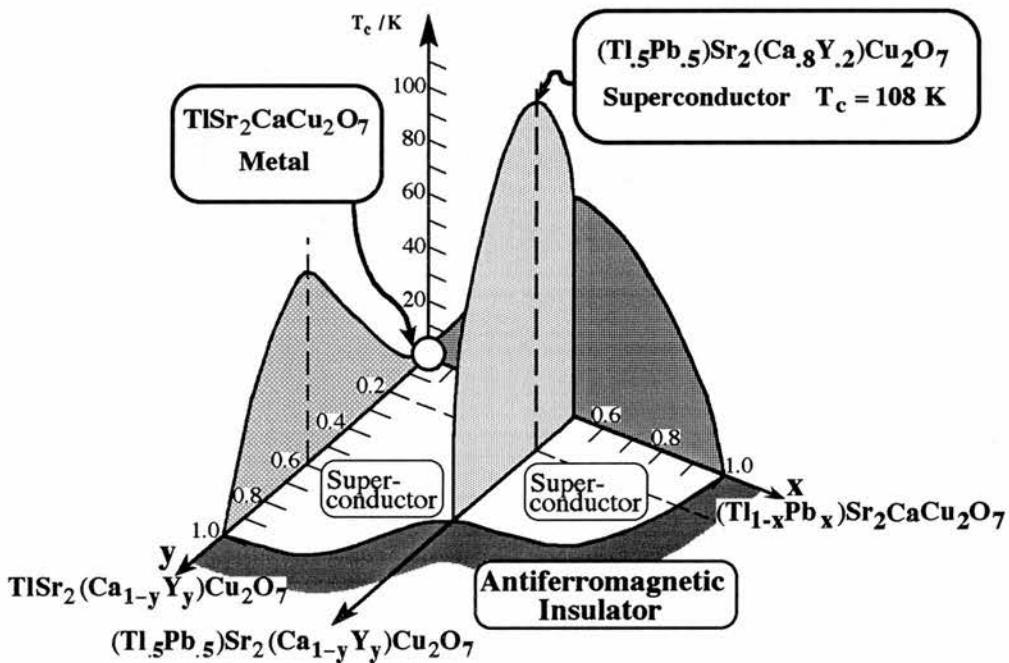


Figure 4.1 Metal-Superconductor-Insulator phase diagram for the  $(\text{Tl}_{1-x}\text{Pb}_x)\text{Sr}_2(\text{Y}_y\text{Ca}_{1-y})\text{Cu}_2\text{O}_{7-\delta}$  system.

### § 4.3 The Structure of $(\text{Tl}_{0.5}\text{Pb}_{0.5})\text{Sr}_2(\text{Y}_y\text{Ca}_{1-y})\text{Cu}_2\text{O}_{7-\delta}$

The structure of  $(\text{Tl}_{0.5}\text{Pb}_{0.5})\text{Sr}_2(\text{Y}_y\text{Ca}_{1-y})\text{Cu}_2\text{O}_{7-\delta}$  consists of layers of thallium ( $\text{Tl}^{3+}$ ) or lead ( $\text{Pb}^{4+}$ ) and copper ions ( $\text{Cu}^{2+}$ ), with strontium ions ( $\text{Sr}^{2+}$ ) and calcium

( $\text{Ca}^{2+}$ ) or yttrium ( $\text{Y}^{3+}$ ) sandwiched in between. All the members of the solid solution have the 1212-type layered structure of  $\text{TlBa}_2\text{CaCu}_2\text{O}_7$ , space group  $\text{P4/mmm}$ . The structure of these materials is similar to  $\text{YBa}_2\text{Cu}_3\text{O}_7$ , with Sr replacing Ba and  $\text{Tl}_{0.5}\text{Pb}_{0.5}$  replacing the chain Cu(1) in  $\text{YBa}_2\text{Cu}_3\text{O}_7$ . However, they are tetragonal and have no chain structure. Figure 4.2 shows a structural comparison between the Tl-1212 system and the YBCO-1237 system.

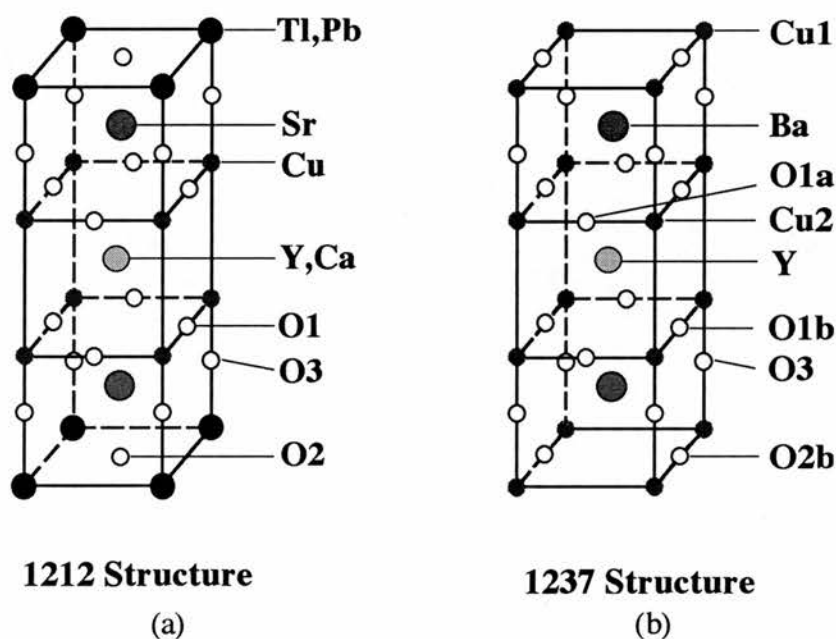


Figure 4.2 A crystal structural comparison between the Tl-1212 system and the YBCO system. [Note: the labelling of the oxygen ions for YBCO is not conventional.]

The powder X-ray diffraction (XRD), selected area electron diffraction (SAED) and energy dispersive X-ray (EDX) have been made on the  $(\text{Tl}_{0.5}\text{Pb}_{0.5})\text{Sr}_2(\text{Y}_y\text{Ca}_{1-y})\text{Cu}_2\text{O}_{7-\delta}$  system by Liu and his coworkers. From their XRD, SAED and EDX results, they confirmed that the sintered samples  $(\text{Tl}_{0.5}\text{Pb}_{0.5})\text{Sr}_2(\text{Y}_y\text{Ca}_{1-y})\text{Cu}_2\text{O}_{7-\delta}$  were homogeneous both in structure and composition. However, from our X-ray data, we did find that there is a small impurity phase on  $y=0.4$  and probably  $y=0.3$  as well. The

impurity phase does affect the Cu NMR and Pb NMR results noticeably. The detailed discussion will be given in next chapter.

Their neutron diffraction data has confirmed the materials to be tetragonal, space group P4/mmm. Site occupancy refinements were carried out on all of these samples and data are consistent with the nominal chemical stoichiometries except the Ca/Y position which refined to a Y occupancy 15% greater than expected. This corresponds to a 10% Tl occupancy of Cu/Y sites.

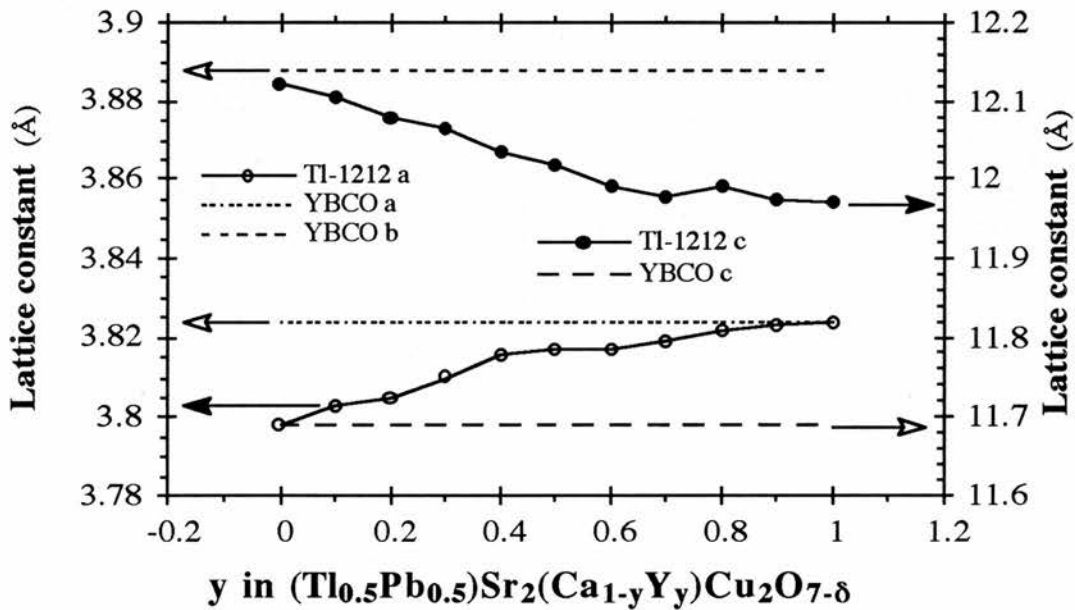


Figure 4.3 Lattice constants (*a* and *c*) for  $(Tl_{0.5}Pb_{0.5})Sr_2(Y_yCa_{1-y})Cu_2O_{7-\delta}$  ( $0 \leq y \leq 1$ ) refined from the neutron diffraction data. The dashed lines are the lattice constants of YBaCuO in which data was taken from Johnston et al.<sup>25</sup>

Figure 4.3 and Table 4.1 show the resulting lattice constants (*a* and *c*), as refined from the neutron diffraction data, for the entire series in  $(Tl_{0.5}Pb_{0.5})Sr_2(Y_yCa_{1-y})Cu_2O_{7-\delta}$ . With increasing yttrium content (*y*), they found a

decrease in the  $c$  lattice parameter, but an increase in the corresponding  $a$  lattice parameter. This reduction in  $c$  probably arises because the radius of the  $Y^{3+}$  ion is slightly smaller than that of the  $Ca^{2+}$  ions<sup>26</sup>. They proposed that the expansion in  $a$  with an increase in  $y$  in this system can be attributed to a longer Cu-O1 (in  $CuO_2$  plane) bond length, and the increase in the Cu-O1 bond length with increasing  $y$  shown in Figure 4.4 may result from a decrease in the effective hole concentration in conducting  $CuO_2$  planes. In contrast to typical YBCO data, the  $a$ -lattice constant is smaller and the  $c$ -lattice constant is larger, as shown in Figure 4.3.

**Table 4.1** The lattice constants for the entire series in  $(Tl_{0.5}Pb_{0.5})Sr_2(Y_yCa_{1-y})Cu_2O_{7-\delta}$ .

$y$	$a$ (Å)	$c$ (Å)
0.0	3.79850(2)	12.1236(1)
0.1	3.80262(2)	12.1064(1)
0.2	3.80562(2)	12.0804(1)
0.3	3.80990(2)	12.0656(1)
0.4	3.81608(2)	12.0347(1)
0.5	3.81742(2)	12.0186(1)
0.6	3.81732(2)	11.9918(1)
0.7	3.81854(2)	11.9790(1)
0.8	3.82172(2)	11.9899(1)
0.9	3.82331(2)	11.9735(1)
1.0	3.82391(2)	11.9697(1)

The crystal structure parameters are important parameters for analysing the NMR / NQR data. It is necessary to know the detailed metal-oxygen interatomic distances in the series of  $(\text{Tl}_{0.5}\text{Pb}_{0.5})\text{Sr}_2(\text{Y}_y\text{Ca}_{1-y})\text{Cu}_2\text{O}_{7-\delta}$ . Figures 4.4 ~ 4.7 show all the ion distances to their neighbouring oxygen and some corresponding distances in the typical  $\text{YBa}_2\text{Cu}_3\text{O}_{7-\delta}$  in which the data all were taken from ref. (25). All the data for  $(\text{Tl}_{0.5}\text{Pb}_{0.5})\text{Sr}_2(\text{Y}_y\text{Ca}_{1-y})\text{Cu}_2\text{O}_{7-\delta}$  system were taken from Table 2.2 in ref. (1). Comparison of the structural parameters between the two systems may provide some useful information for analysing the NMR and NQR data. In particular, we notice that the Y-O distance is larger in the Tl system than in YBCO. However, the yttrium to the copper plane distance is smaller in the Tl system than in YBCO shown in Figure 4.7 and Figure 4.9.

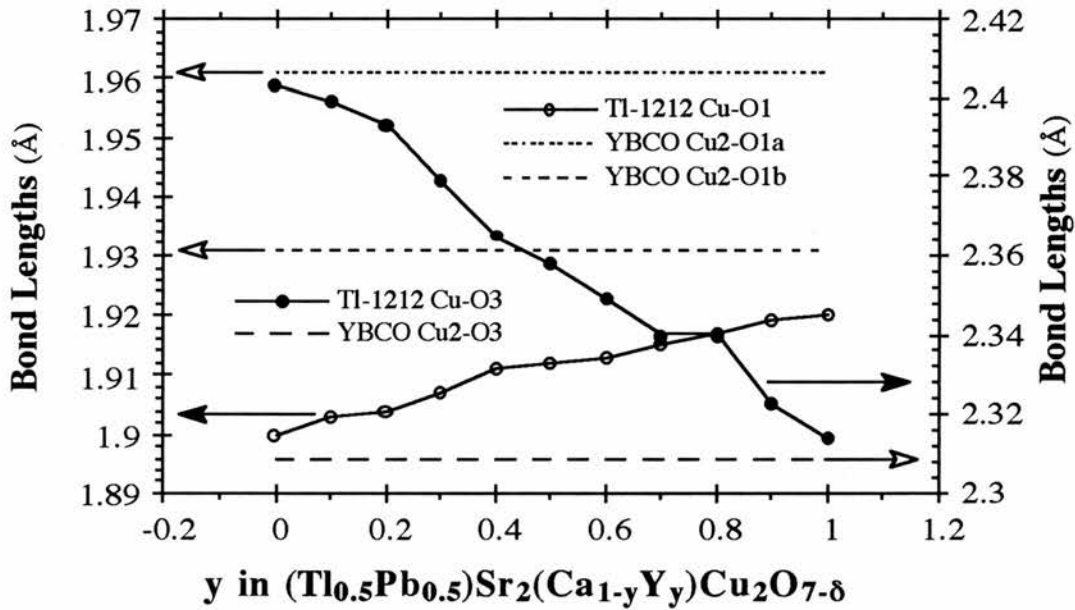


Figure 4.4 Copper ion to its neighbouring oxygen distances. [Note: Figure 4.2 gives the labelling of the oxygen ions for YBCO, which is not conventional.]

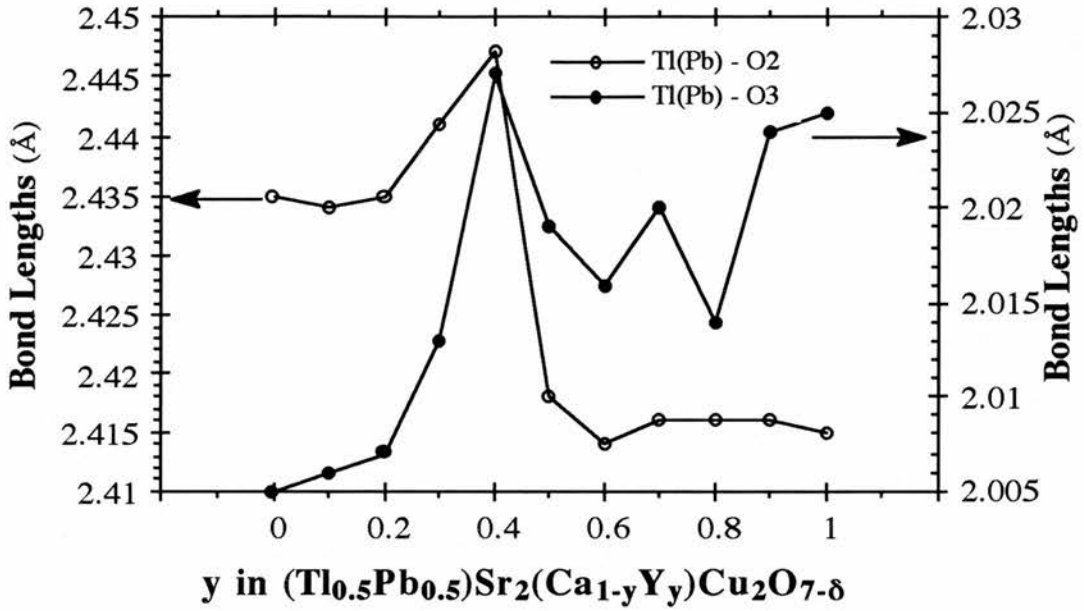


Figure 4.5 Thallium (Lead) ion to its neighbouring oxygen distances.

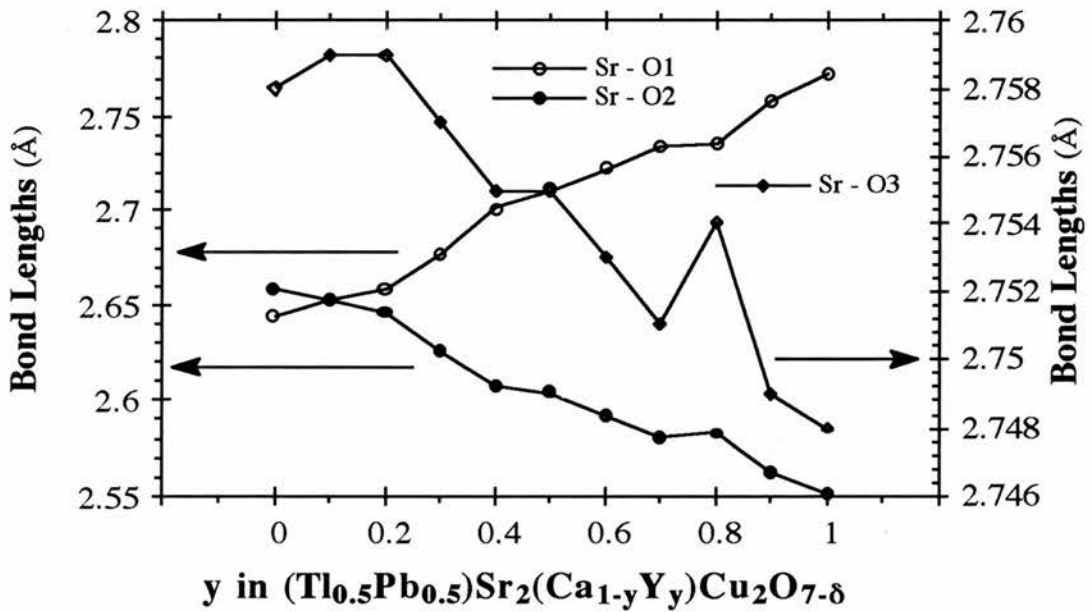


Figure 4.6 Strontium ion to its neighbouring oxygen distances.

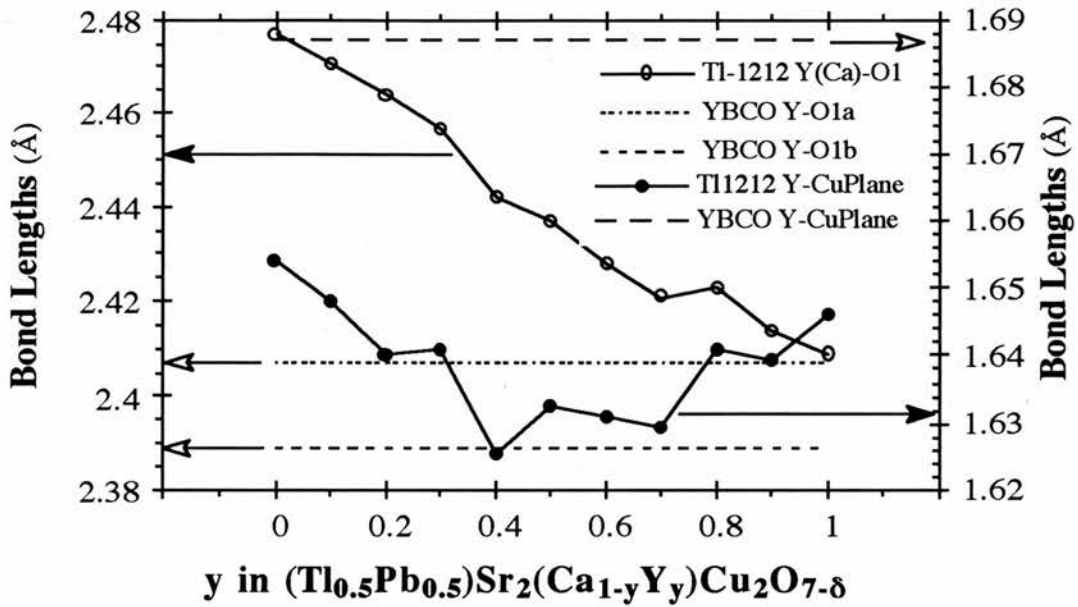


Figure 4.7  $Y^{3+}$  ( $Ca^{2+}$ ) to its neighbouring oxygen distances. [Note: Figure 4.2 gives the labelling of the oxygen ions for YBCO, which is not conventional.]

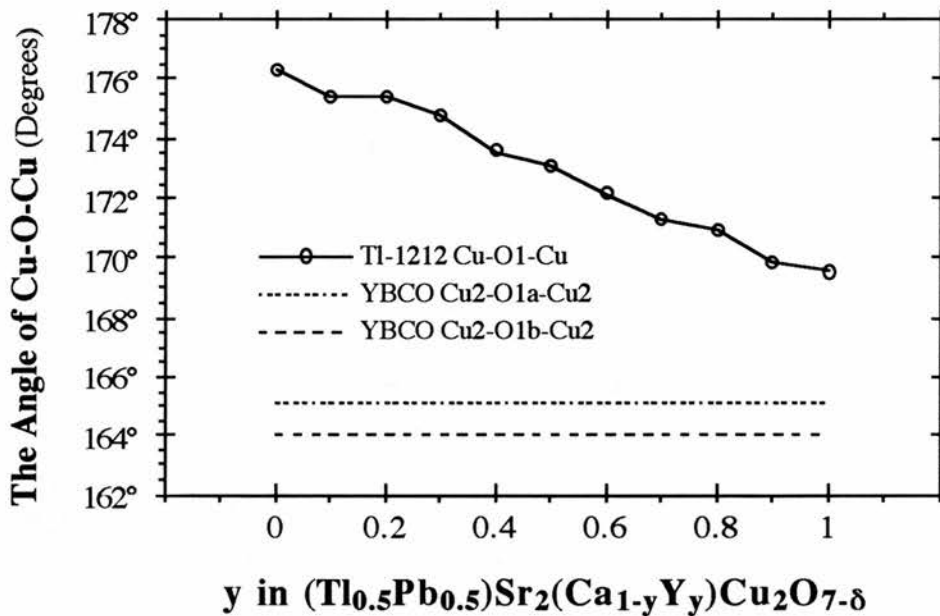


Figure 4.8 The angle of Cu-O-Cu in Cu-O plane. [Note: Figure 4.2 gives the labelling of the oxygen ions for YBCO, which is not conventional.]

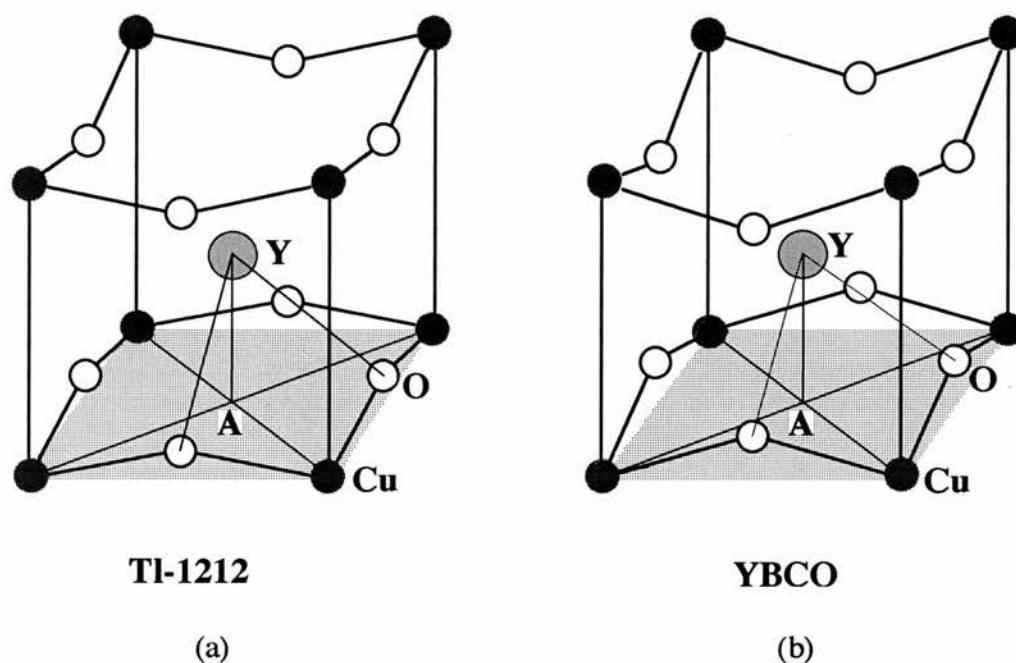


Figure 4.9 A partial structural comparison between  $(Tl_{0.5}Pb_{0.5})Sr_2(Y_yCa_{1-y})Cu_2O_{7-\delta}$  and  $YBa_2Cu_3O_{7-\delta}$ .

One needs to mention here that the distance of Tl (Pb) to O2 is less than  $\frac{\sqrt{2}}{2}a$ .

Evidence for structure disorder, associated with the Tl/Pb and O sites in the (Tl,Pb)-O layers, comes from the large in-plane thermal parameters and this shows the O is displaced from its central position. Fourier difference analysis of the data also suggests a small Cu occupancy in the Tl/Pb sites.

The distance of Tl(Pb)-O2 was also measured by some other groups on the samples of  $(Tl_{1-x}Pb_x)Sr_2(Y_yCa_{1-y})Cu_2O_7$  by Vijayaraghavan *et al.*<sup>27</sup> and  $(Tl_{0.5}Pb_{0.5})Sr_2CaCu_2O_7$  by Parise *et al.*<sup>28</sup> and Otto *et al.*<sup>29</sup>, and  $(Tl_{0.8}Pb_{0.2})Sr_2CaCu_2O_7$  in ref. (29). However, no structure disorder in the Tl (Pb)-O layers was found by them. We cannot confirm which is correct.

## § 4.4 Physical Properties of $(\text{Tl}_{0.5}\text{Pb}_{0.5})\text{Sr}_2(\text{Y}_y\text{Ca}_{1-y})\text{Cu}_2\text{O}_7$

### § 4.4.1 Resistivity

Resistivity measurements on the Tl-1212 system have been made by Liu *et al.*<sup>1</sup>. Figure 4.10 represents the results of their measurements on  $y=0.0 \sim 0.6$ . With increasing  $y$ , the room temperature resistivity increase monotonically. To clarify the room temperature properties, we redraw the resistance as a function of  $y$  ( $0 \leq y \leq 0.6$ ), the yttrium concentration at room temperature, shown in Figure 4.11. For comparison, the resistance of YBaCuO has also been shown in the figure in which data was taken from Cooper *et al.*<sup>30</sup>

For  $y = 0.6$ , the sample exhibits semiconducting behaviour. This semiconducting state may well be anti-ferromagnetic. The evidence for this is based on: i) characteristic semiconducting resistivity behaviour, ii) the absence of any intrinsic  $\text{Cu}^{2+}$  electron spin resonance signal (from room temperature to liquid helium temperature), an observation reminiscent of high-temperature antiferromagnetic ordering in cuprates, iii) the observation of antiferromagnetism in the related compound  $\text{TlBa}_2\text{YCu}_2\text{O}_7$ , which has a Neel temperature in excess of 350 K. Liu *et al.* have proposed that the insulating state at  $y = 1$ ,  $(\text{Tl}_{0.5}\text{Pb}_{0.5})\text{Sr}_2\text{YCu}_2\text{O}_7$ , may, in fact, be antiferromagnetic. From our NMR experiments, we agree with their proposal that the sample  $y = 1.0$  is antiferromagnetic. Moreover, we found that the sample  $y = 0.9$  also exhibits an antiferromagnetic behaviour with a Neel temperature around 340 K, as discussed in next chapter.

### § 4.4.2 Meissner Effect

Figure 4.12 shows the temperature dependence of the field-cooled magnetization (called the Meissner effect) of powdered samples  $(\text{Tl}_{0.5}\text{Pb}_{0.5})\text{Sr}_2(\text{Y}_y\text{Ca}_{1-y})\text{Cu}_2\text{O}_7$ . With

increasing  $y$  values, the onset diamagnetism rises up from 77.5 K for  $y=0.0$  to a maximum 108 K for  $y=0.2$  and then decreases. From Figure 4.12, the volume fraction (Meissner fraction,  $\chi/\chi_0$  where  $\chi$  and  $\chi_0$  are the measured and the perfect diamagnetic susceptibility ( $-1/4\pi$ ) without field penetration, respectively) has been calculated out by Liu *et al.* A continuous decrease in the apparent superconducting volume fraction with increasing  $y$  was obtained. However, this has detailed differences from the data of our experiment of A.C. inductance measurement on the powder samples set in Stycast, to be discussed in next chapter.

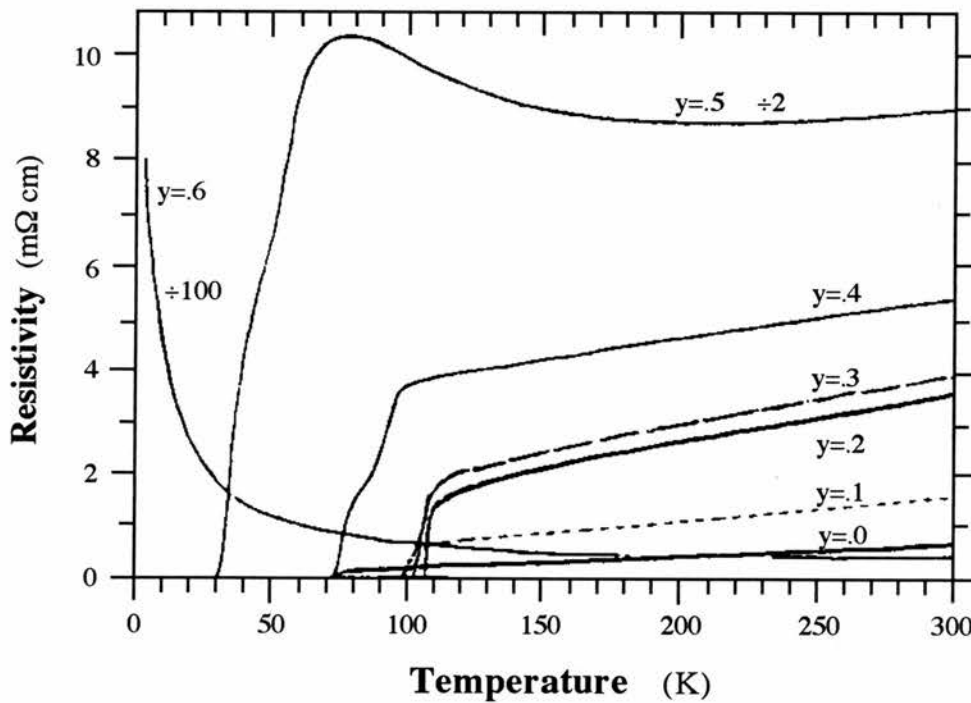


Figure 4.10 Temperature dependence of the electrical resistivity of  $(Tl_{0.5}Pb_{0.5})Sr_2(Y_yCa_{1-y})Cu_2O_7$  for  $0 \leq y \leq 0.6$

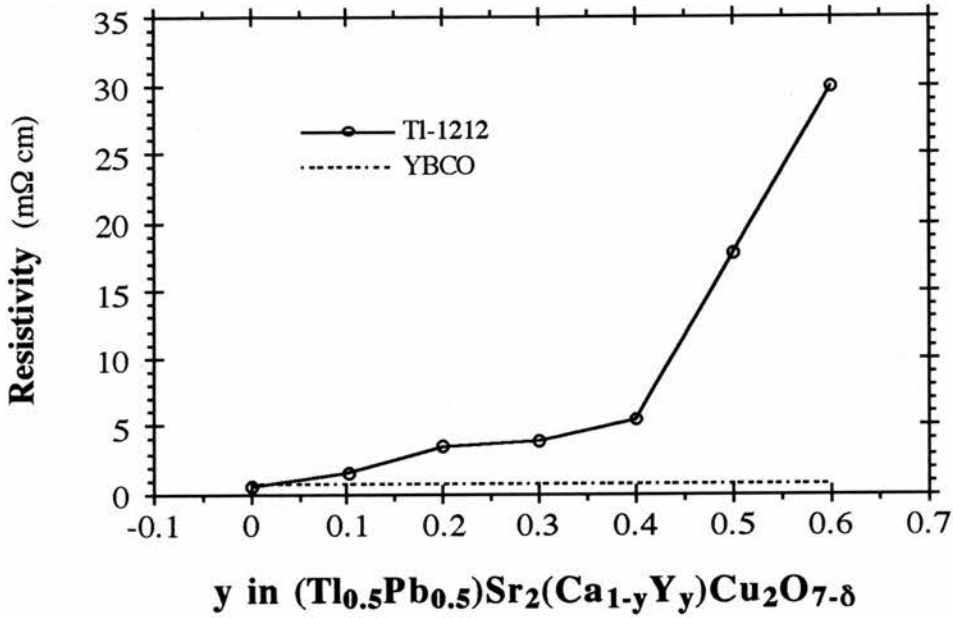


Figure 4.11 The resistivity as a function of yttrium concentration at room temperature. The data is taken from Figure 4.10. The dashed line is the resistivity of  $\text{YBa}_2\text{Cu}_3\text{O}_{7-\delta}$  ( $\delta = 0.05$ ) data taken from Cooper et al.<sup>30</sup>

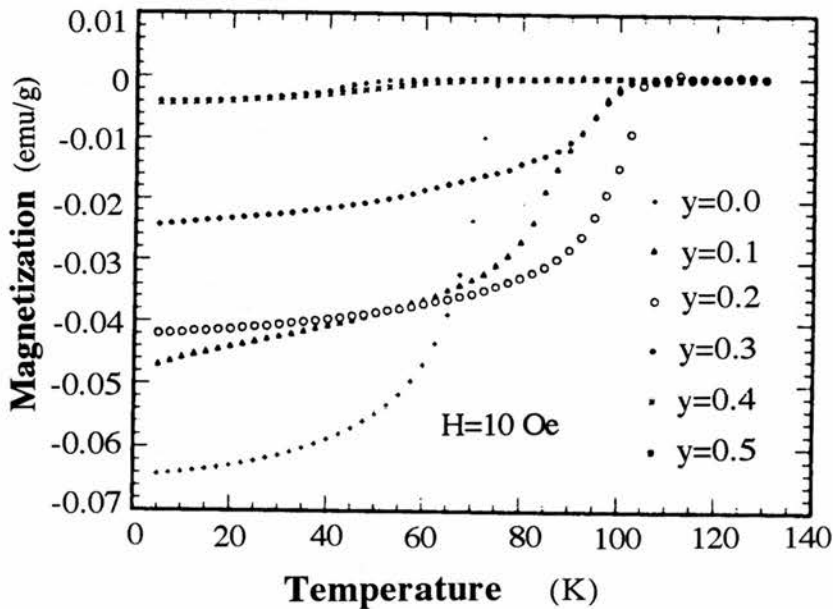


Figure 4.12 Temperature dependence of the field cooled magnetization of the powdered samples. (After Liu<sup>1</sup>)

### § 4.4.3 Hall Effect

Hall effect is potentially one of the most useful experiments, since it provides information on the charge carrier density  $n$ , as well as the sign of the carriers.<sup>31</sup> However, as in most studies of the normal state properties of the high- $T_c$  oxide superconductors the results display an interesting pattern that complicates the interpretation of the data.<sup>32,33</sup> An anomalous contribution to the Hall scattering modulates the temperature dependence in a characteristic way: the Hall coefficient  $R_H$  increases monotonically with decreasing temperature in all the superconductors based on  $\text{CuO}_2$  planes.<sup>34</sup>

It is often convenient to express  $R_H$  in terms of a "Hall density"  $n_H$  [defined as  $1/(R_H e)$ ]. For comparison between systems,  $n_H$  is often normalised to the unit-cell volume. It is also useful to express the carrier density as the number of mobile holes per Cu ion. The Hall density normalised in this way is called  $p_H$  [defined as  $n_H V/N$  where  $V$  is the unit cell volume and  $N$  the number of Cu ions per cell]. In the  $\text{YBa}_2\text{Cu}_3\text{O}_{7-\delta}$  system,  $N$  is defined as the number of plane-site ions *i.e.* Cu(2) because it is believed that holes on the chain sites are immobile.

Figure 4.13 shows the compositional dependence ( $y$ ) of the Hall number at room temperature. It can be seen that the Hall number monotonically decreases as the compositional parameter  $y$  is increased. This supports the proposal that substitution of  $\text{Y}^{3+}$  for  $\text{Ca}^{2+}$  in  $(\text{Tl}_{0.5}\text{Pb}_{0.5})\text{Sr}_2(\text{Y}_y\text{Ca}_{1-y})\text{Cu}_2\text{O}_{7-\delta}$  results in the introduction of excess electrons into the conducting  $\text{CuO}_2$  planes. This finding is fully consistent with the chemically intuitive view of the effects of the substitution of 3+ ions for 2+ ions in the structure. It is generally assumed that this excess electron enters an antibonding Cu-O hybrid orbital and results in a decrease in the hole concentration.<sup>35</sup> This suggestion is also consistent with the observed expansion of the  $a$  lattice constant and Cu-O1 bond length with increasing  $y$  (see Figure 4.3 and 4.4).

For comparison, the Hall number density of  $\text{YBa}_2\text{Cu}_3\text{O}_{7-\delta}$  ( $\delta = 0.05$ ) has also been shown in Figure 4.13 (dashed line). Data is taken from ref.(30). As we can see, the Hall number in YBCO is larger than in the Tl-1212 system *i.e.* the hole concentration is larger in YBCO than in Tl-1212.

Some other physical properties have also been studied by Liu, *e.g.* thermoelectric power effect, Specific heat effect, magnetoresistance effect, electron energy loss studies. For details about these physical properties, the reader is referred to ref. (1).

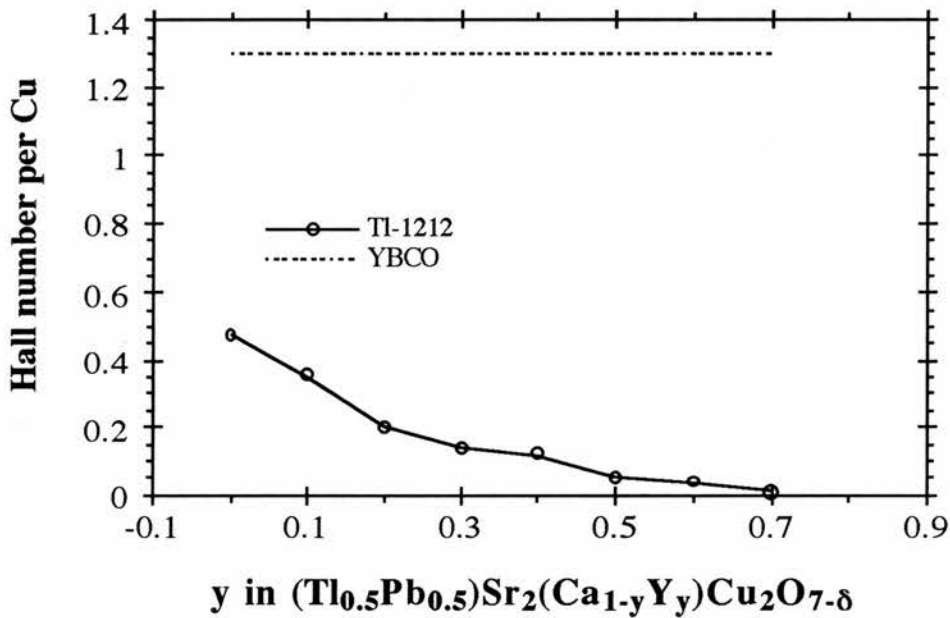


Figure 4.13 Hall number per Cu at room temperature for the series  $(\text{Tl}_{0.5}\text{Pb}_{0.5})\text{Sr}_2(\text{Y}_y\text{Ca}_{1-y})\text{Cu}_2\text{O}_{7-\delta}$  ( $0 \leq y \leq 0.7$ ). The dashed line is for  $\text{YBa}_2\text{Cu}_3\text{O}_{7-\delta}$  ( $\delta = 0.05$ ) data taken from ref.(30)

## References

- 1 (a) Liu R.S., Edwards P.P., Huang Y.T., Wu S.F., and Wu P.T., *J. Solid State Chem.* **86**, 334 (1990)  
 (b) Liu R.S., and Edwards P.P., *Material Science Forum* ed by Pouch J.J. et al. NASA (1992)  
 (c) Liu R.S., *PhD Thesis*, University of Cambridge, UK (1992)
- 2 Bednorz J.G. and Muller K.A. *Z. Phys.* **B64**, 189 (1986)
- 3 Wu M.K., Ashburn J.R., Torng C.T., Hor P.H., Meng R.L., Gao L., Huang Z.J., Wang Y.Q. and Chu C.W., *Phys. Rev. Lett.* **58**, 908 (1987)
- 4 Maeda H., Tanaka Y., Fukutomi M. and Asano T., *Jpn. J. Appl. Phys. Lett.* **27**, L209 (1988)
- 5 Sheng Z.Z. and Hermann A. M., *Nature* **332**, 138 (1988)
- 6 Sheng Z.Z., Kiehl W., Bennett J., Ali A.El, Marsh D., Mooney G.D., Arammash F., Smith J., Viar D., Hermann A.M., *Appl. Phys. Lett.* **52**, 1738 (1988)
- 7 Hazen R.M., Finger L.W., Angel G.J., Prewit C.T., Ross N.L., Ali A.El, Hermann A.M., *Phys. Rev. Lett.* **60**, 1657 (1988)
- 8 Torandi C.C., Subramanian M.A., Gopalakrishnan J., McCarron E.M., Morrissey K.J., Askew T.R., Flippen R.B., Chowdhry U and Sleight A.W., *Science* **240**, 631 (1988)
- 9 Parkin S.S.P., Lee V.Y., Engler E.M., Nazzal A.I., Huang T.C., Gorman G., Savoy R., and Beyers R., *Phys Rev. Lett.* **60**, 2539 (1988)
- 10 Parkin S.S.P., Lee V.Y., Nazzal A.I., Savoy R., Beyers R., and *Phys Rev. Lett.* **61**, 750 (1988)
- 11 Beyers R., Parkin S.S.P., Lee V.Y., Nazzal A.I., Savoy R., Gorman G., Huang T.C., and Placa S.J. *La Appl. Phys Lett.* **53**, 432 (1988)

- 12 Sheng Z.Z., Hermann A.M., Vier D.C., Schultz S., Oseroff S.B., George D.J., and Hazen R.M., *Phys. Rev. B* **38**, 7074 (1988)
- 13 Nagashima T., Watanabe K., Saito H., and Fukai Y., *Jpn. J. Appl. Phys.* **27**, L1077 (1988)
- 14 Subramanian M.A., Torardi C.C., Gopalakrishnan J., Gai P.L., Calabrese P.L., Askew T.R., Flippen R.B., and Sleight A.W., *Science* **242**, 249 (1988)
- 15 Ganguli A.K., Nanjundaswamy K.S., and Rao C.N.R., *Physica C* **156**, 788 (1988)
- 16 Liu R.S., Huang Y.T., Lee W.H., Wu S.F., and Wu P.T., *Physica C* **156** 791 (1988)
- 17 Haldar P., Sridhar S., Roig-Janicki A., Kennedy W., Wu D.H., Zahopoulos C., and Giessen B.C., *J. Supercon.* **1**, 211 (1988)
- 18 Li S., and Greenblatt M., *Physica C* **157** 365 (1989)
- 19 Sheng Z.Z., Sheng L., Fei X., and Hermann A.M., *Phys. Rev. B* **39**, 2918 (1989)
- 20 Rao C.N.R., Ganguli A.K., Vijayaraghavan R., *Phys. Rev. B* **40**, 2565 (1989)
- 21 Liu R.S., Liang J.M., Wu S.F. Huang Y.T., Wu P.T., and Chen L.J., *Physica C* **159**, 385 (1989)
- 22 Wu P.T., Liu R.S., Liang J.M., Huang Y.T., Wu S.F. and Chen L.J., *Appl. Phys. Lett.* **54**, 2464 (1989)
- 23 Liang J.M., Liu R.S., Huang Y.T., Wu S.F., Wu P.T., and Chen L.J., *Physica C* **165**, 347 (1990)
- 24 Huang Y.T., Liu R.S., Wang W.N., and Wu P.T., *Jpn. J. Appl. Phys.* **28**, L1514 (1989)

- 25 Johnston D.C., Jacobson A.J., Newsam J.M., Lewandowski J.T., Goshorn D.P., Xie D., and Yelon W.B., *Am. Chem. Soc. Symposium Series* **351**, 136 (1987)
- 26 Shannon R.D., *Acta Cryst. A* **32**, 751 (1976)
- 27 Vijayaraghavan R., Rangavittal N., Kulkarni G.U., Grantscharova E., Row T.N.G., and Rao C.N.R., *Physica C* **179**, 183 (1991)
- 28 Parise J.B., Gai P.L., Subramanian M.A., Gopalakrishnan J., and Sleight A.W., *Physica C* **159**, 245 (1989)
- 29 Otto H.H., Zetterer T., and Renk K.F., *Z. Phys.*, **B 75**, 433 (1989)
- 30 Cooper J.R., Obertelli S.D., and Loram J.W., *Phys. Rev. B* **44**, 12086 (1991)
- 31 *The Hall Effect and Its Applications*, ed. by Chien C.L., and Westgate C.R., Plenum press, New York, (1980)
- 32 *Novel Superconductivity*, ed. by Wolf S.A., Kresin V.Z., Plenum press, New York, (1987)
- 33 *High Temperature Superconductors and Materials and Mechanisms of Superconductivity, Parts I & II*, ed by Muller J., and Olsen J.L., North Holland, Amsterdam (1988) [*Physica C* **153-155**, (1988)].
- 34 Ong N.P., in *Physical Properties and High Temperature Superconductors Vol II* ed by Ginsberg D., World Scientific Publishers (1990)
- 35 Goodenough J.B., *Supercond. Sci. Technol.* **3**, 26 (1990); Goodenough J.B. and Zhou J., *Phys. Rev. B* **42**, 4276 (1990)

## Chapter 5

# Experimental Results

In order to obtain better NMR results, we attempted to align the powder samples in Stycast. Since for different probes one needs a different size of sample, initially, we set in Stycast 3 different series of samples for thallium NMR (labelled as TAY\*, \* = 0, 1, 2, ..., 10, for the sample of  $y = 0.0, 0.1, 0.2, \dots, 1.0$ , on  $(\text{Tl}_{0.5}\text{Pb}_{0.5})\text{Sr}_2(\text{Y}_y\text{Ca}_{1-y})\text{Cu}_2\text{O}_{7-\delta}$ , respectively) copper NMR (labelled as CAY\*), and yttrium NMR (labelled YAY\*). Later, we set in Stycast another two series of samples for Cu NMR which are labelled as NCAY\* and RCY\* where N and R stand for newly aligned setting sample and randomly oriented sample, respectively.

### § 5.1 Alignment

The x-ray diffraction spectra have been performed on most of the samples. Figure 5.1 shows some of the spectra on the randomly oriented samples (RCY\*) which look entirely the same as those published by Liu et al.<sup>1</sup> Figure 5.2 and 5.3 present some of the spectra on the partially aligned samples of CAY\* and NCAY\*, respectively. Using a computer programme (see Chapter 3) to identify the peaks ( $hkl$ ) shown in the figures, we found an obvious impurity phase in sample  $y = 0.4$ , and also perhaps in  $y = 0.3$ , shown in Figure 1(e) and 1(d). The composition of the impurity phase may be  $(\text{Sr,Ca})_5\text{Cu}_2\text{Pb}_3\text{O}_y$ <sup>2</sup>. From these diagrams, we can see that the degree of the alignment differs from sample to sample. Briefly to say, the sample is aligned better, then the

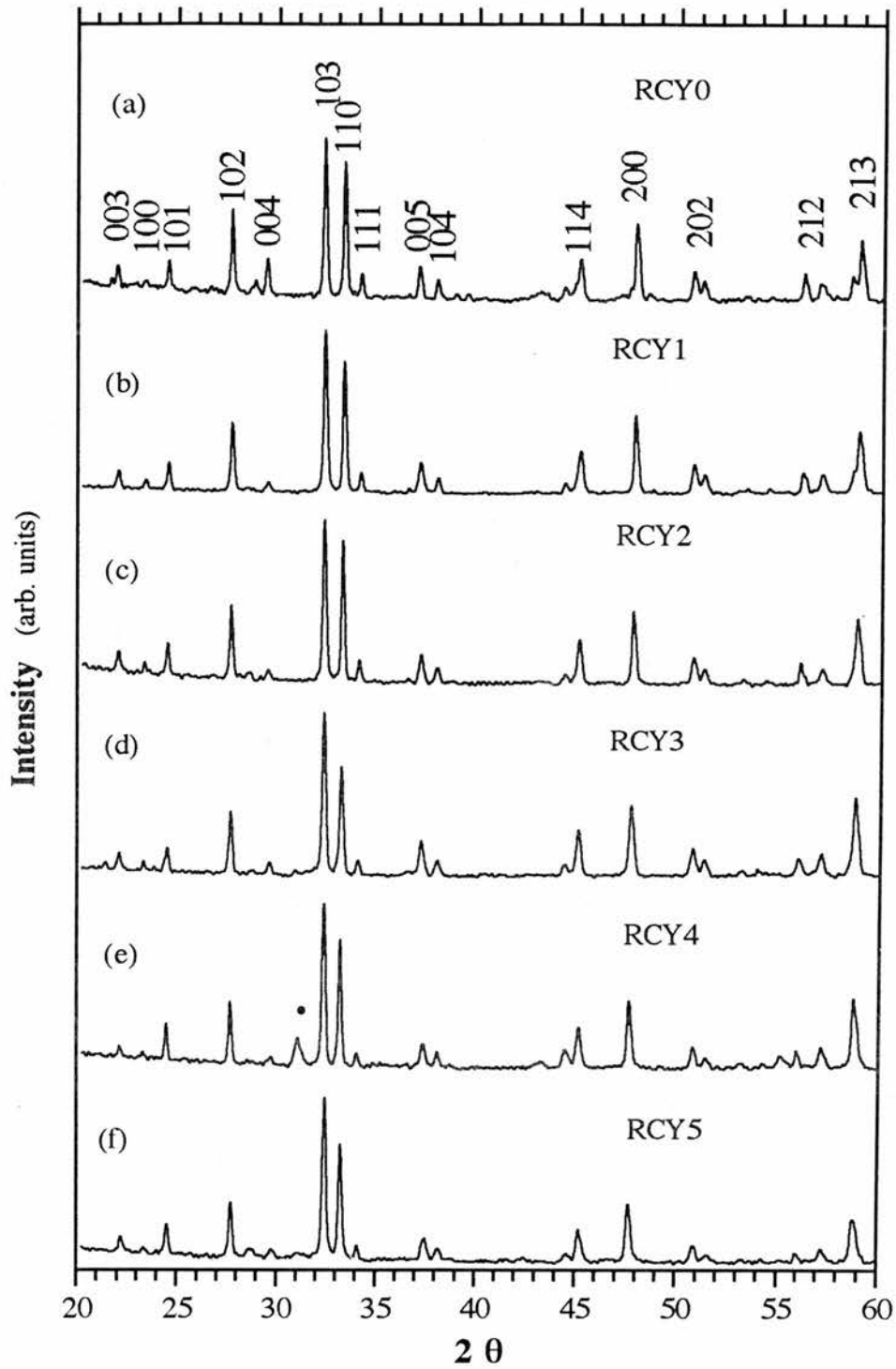


Figure 5.1 X-ray spectra on RCY\* series samples. Evidently there is impurity phase for  $y = 0.4$  sample shown in (e) labelled as dot.

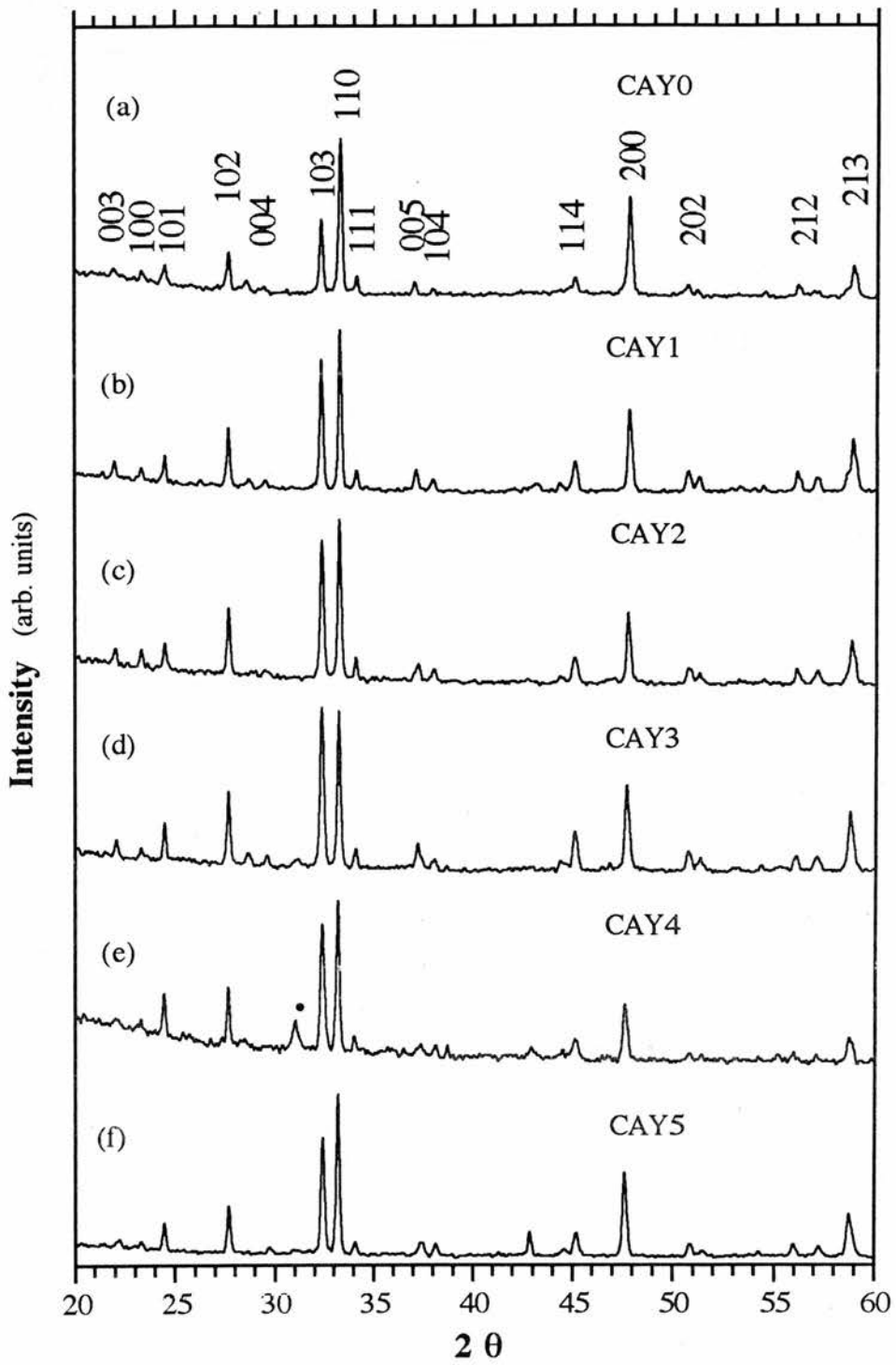


Figure 5.2 X-ray diffraction patterns from the partially aligned powder samples of CAY\* series.

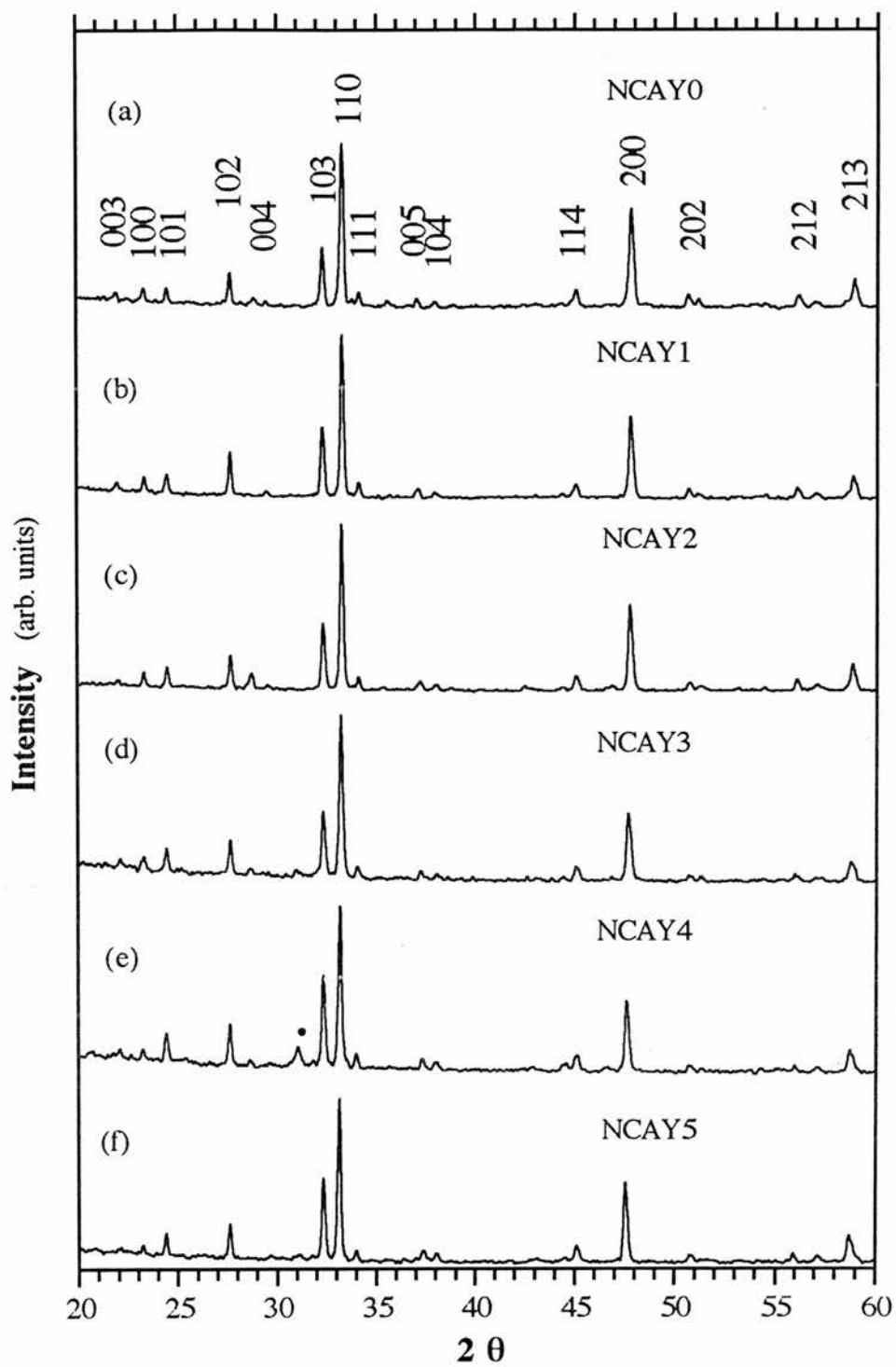


Figure 5.2 X-ray diffraction patterns from the partially aligned powder samples of NCAY\* series.

intensities of the X-ray peaks with  $(hk0)$  (e.g. (110), (200) etc.) are larger, and the others are smaller.

Evidently, the samples of NCA $Y^*$  series are aligned better than the samples of CAY $^*$  series are. To compute the degree of alignment from x-ray data, we used two integrated intensities of the nearby and higher intensity (103), and (110) peaks (we consulted the suggestion by Lusnikov *et al.*<sup>3</sup>). The ratios of the intensities are:

$$R = \frac{I_{110}}{I_{103}} \quad (5.1)$$

$$R' = \frac{I_{110}'}{I_{103}'} = \frac{(1+x)I_{110}}{(1-x)I_{103}} \quad (5.2)$$

where the unprimed and primed quantities denote the values of random and aligned sample, respectively, and  $x$  is the degree of alignment. From equation (5.1) and (5.2), we have:

$$x = \frac{R' - R}{R' + R} \quad (5.3)$$

From the randomly oriented powder samples, we measured the average  $R$  is about 0.77. The measured  $R'$  values and derived  $x$  values using equation (5.3) are listed in Table 5.1, 5.2, 5.3 and 5.4 for the samples of TAY $^*$ , YAY $^*$ , CAY $^*$ , and NCA $Y^*$  series, respectively. In our previous work<sup>4</sup>, we mistakenly believed that the degree of the alignment would not differ from sample to sample. The method of estimation in the previous work is different to this work. Therefore, the degree of alignment estimated in that previous work is higher than here. We believe our present estimates are more accurate.

As we can see from these tables, the highest degree of alignment is less than 60% and the lowest degree is just over 10%. However, under the same conditions, the degree

of alignment of YBCO sample can achieve as high as 97%<sup>5</sup>. We found that for some reason in the thallium based material, it is always difficult to obtain a good alignment. For example, Song *et al.* only obtained 20% ~ 40% alignment on  $Tl_2Ba_2Ca_2Cu_3O_{10+\delta}$  material<sup>6</sup>.

**Table 5.1.** The ratios ( $R'$ ) and degrees of alignment ( $x$ ) of the samples on TAY\*.

Samples	$R'$	$x$ in %
TAY0	2.94	58.5
TAY2	2.08	46.0
TAY3	1.06	16.0
TAY4	1.67	36.8

**Table 5.2.** The ratios ( $R'$ ) and degrees of alignment ( $x$ ) of the samples on YAY\*.

Samples	$R'$	$x$ in %
YAY1	1.64	36.0
YAY2	0.98	14.0
YAY3	1.56	34.0
YAY4	1.39	28.7
YAY5	1.59	34.7
YAY6	1.54	33.2
YAY7	1.28	25.0

**Table 5.3.** The ratios ( $R'$ ) and degrees of alignment ( $x$ ) of the samples on CAY\*.

samples	$R'$	$x$ in %
CAY0	2.174	47.7
CAY1	1.250	23.8
CAY2	1.149	19.8
CAY3	0.980	14
CAY4	1.220	22.6
CAY5	1.389	28.7

**Table 5.4.** The ratios ( $R'$ ) and degrees of alignment ( $x$ ) of the samples on NCAY\*.

samples	$R'$	$x$ in %
NCAY0	2.857	57.5
NCAY1	2.381	51.1
NCAY2	2.564	53.8
NCAY3	2.564	53.8
NCAY4	1.818	40.5
NCAY5	2.041	45.2
NCAY6	2.857	57.5
NCAY7	1.923	42.8
NCAY8	2.703	55.7

## § 5.2 A.C. Susceptibility

Initially, we measured the A.C. susceptibility of the samples of TAY\* series shown in Figure 5.4. This has detailed differences from the data in Liu's work, (see Figure 4.12). If we take the size of the diamagnetic step as a measure of the superconducting fraction, then clearly  $y = 0.3$  has the largest fraction in our TAY\* series. They found the largest fraction at  $y = 0.0$ ; thereafter there is a monotonic decrease. In comparing the two sets of data it is important to realize the distinctly different sample conditions: Liu's work is with a compacted ceramic pellet or powder, albeit in a magnetic field of 1 mT. In our case each particle is well separated by Stycast from its neighbour, and our sample is partially aligned in such a way that the  $c$  axis of the aligned powders lies perpendicular to the A.C. magnetic field.

To find out the exact reason for the distinction, we have then performed A.C. inductance measurements on the samples of CAY\* and NCAY\* series shown in Figure 5.5 and 5.6, respectively. As we can see from these diagrams, the largest superconducting fraction differs from one series to another. Further analysing the data and comparing with the alignment fraction from the X-ray measurement shown in Table 5.1, 5.3, and 5.4, we found that the superconducting fraction is related to the alignment fraction, and a larger alignment fraction tends to reduce the superconducting fraction. Therefore we propose if we perform the A.C. inductance measurement on random oriented powder samples, we should obtain the same order as Liu's work. To prove this point, we then performed the measurement on the RCY\* samples shown Figure 5.7. As we can see from Figure 5.7, the largest superconducting fraction is at  $y = 0.0$  and thereafter there is a monotonic decrease as we expected.

From our A.C. inductance measurement, we can point out the following two points: i) under exactly the same conditions, the superconducting fraction decreases with increasing yttrium concentration. ii) for the same yttrium concentration, the

superconducting fraction also decreases as the degree of alignment increases. One may ask why the superconducting fraction depends on the yttrium concentration and the degree of alignment. The effects might be related to the variation of penetration depth with hole carrier concentration,  $n$ . However, as we can see later from T1 NMR measurements at 1.5 K, the penetration depth does not seem to change much with yttrium concentration changes. This effect may be related to the defect model, which will be discussed in § 6.9. Since the penetration depth is highly anisotropic for all cuprate superconductors, and larger for the field parallel to Cu-O plane than perpendicular to the plane, in the cases of our experiment, because the aligned c-axis is always perpendicular to the A.C. magnetic field, *i.e.* the field is parallel to Cu-O plane, a larger degree of alignment will produce a larger penetration depth and therefore smaller superconducting fraction. Measuring the magnetization on the partially aligned  $\text{YBa}_2\text{Cu}_3\text{O}_{7-\delta}$  sample by Lusnikov *et al.* have indicated that when the field direction is parallel the preferred c direction of the grains, the magnetic susceptibility  $\chi$  is larger than when the field direction is perpendicular to the c direction.<sup>3</sup>

To compute the susceptibility from A.C. inductance measurement, we have,

$$L_{\text{exp.}} = L_1' + L_2 \quad (5.4)$$

where  $L_{\text{exp.}}$ ,  $L_1'$  and  $L_2$  are the inductances of experimental value, coil 1 and coil 2, (see Figure 3.11), respectively. If we put a sample with the susceptibility  $\chi$  into coil 1, then the inductance of coil 1 is,

$$L_1' = L_1 \left( 1 + \frac{V_s}{V_c} \chi \right) \quad (5.5)$$

where the primed and unprimed quantities denote the inductances with and without sample, respectively.  $V_c$  and  $V_s$  are the volume of the coil and sample, respectively. Since the coil 2 is wound in opposition with an identical to coil 1, we then have,

$$L_2 = -L_1 \quad (5.6)$$

therefore, the experimental value is,

$$L_{\text{exp.}} = L_1 \left( 1 + \frac{V_s}{V_c} \chi \right) - L_1 = \frac{V_s L_1}{V_c} \chi \quad (5.7)$$

So the A.C. susceptibility is,

$$\chi = \frac{V_c L_{\text{exp.}}}{V_s L_1} \quad (5.8)$$

To compute the susceptibility, the volume of the coil 1,  $V_c$ , the volume of sample,  $V_s$  and the inductance of coil 1,  $L_1$ , need to be measured. Since the perfect diamagnetic susceptibility  $\chi_0$  without field penetration is -1, then we can calculate a superconducting volume fraction  $\frac{\chi}{\chi_0}$  shown in Table 5.5 together with the results of Liu's work. From

this table, we can see that two results are in a good agreement.

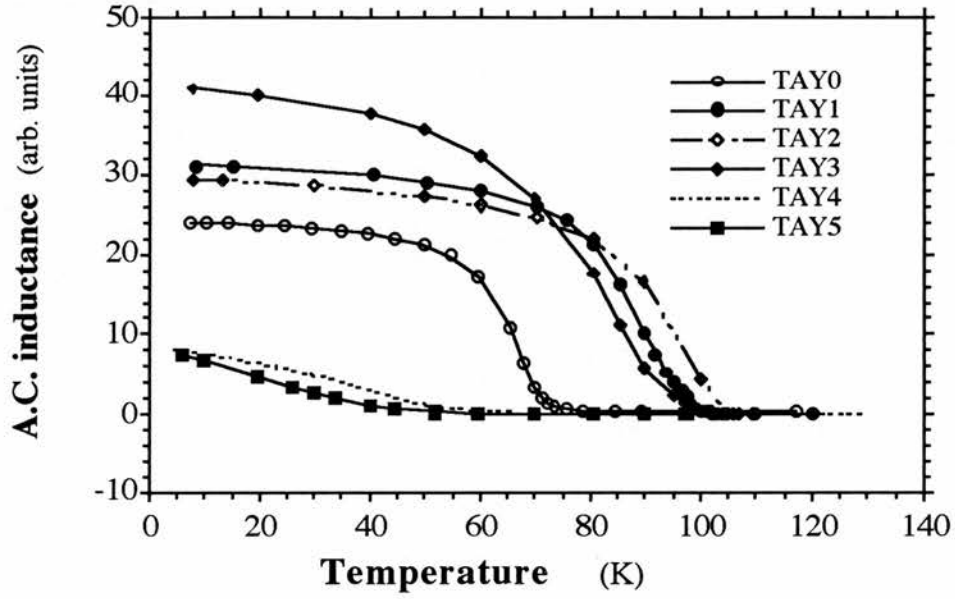


Figure 5.4 A.C. inductance vs temperature for the samples of TAY\*.

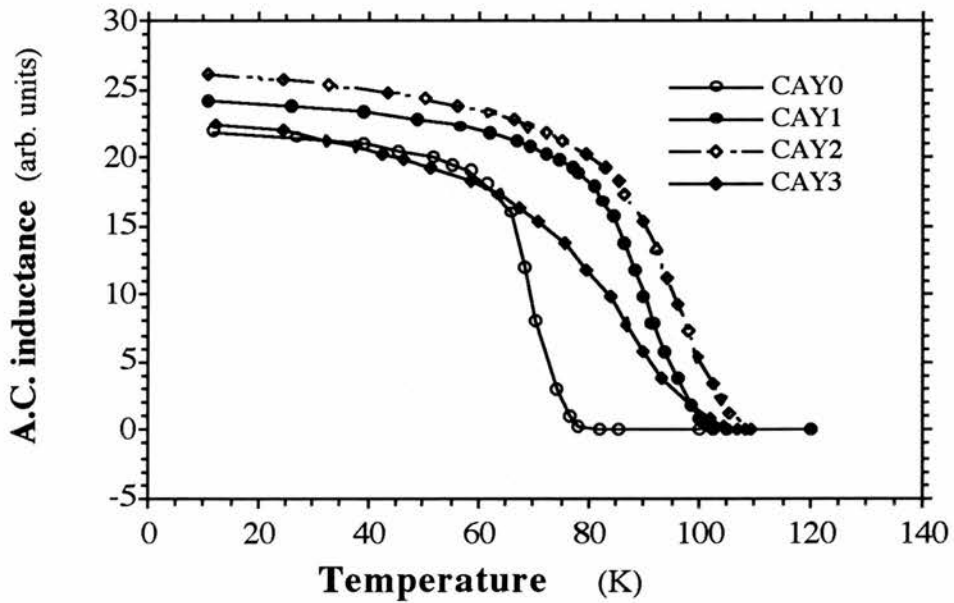


Figure 5.5 A.C. inductance vs temperature for the samples of CAY\*.

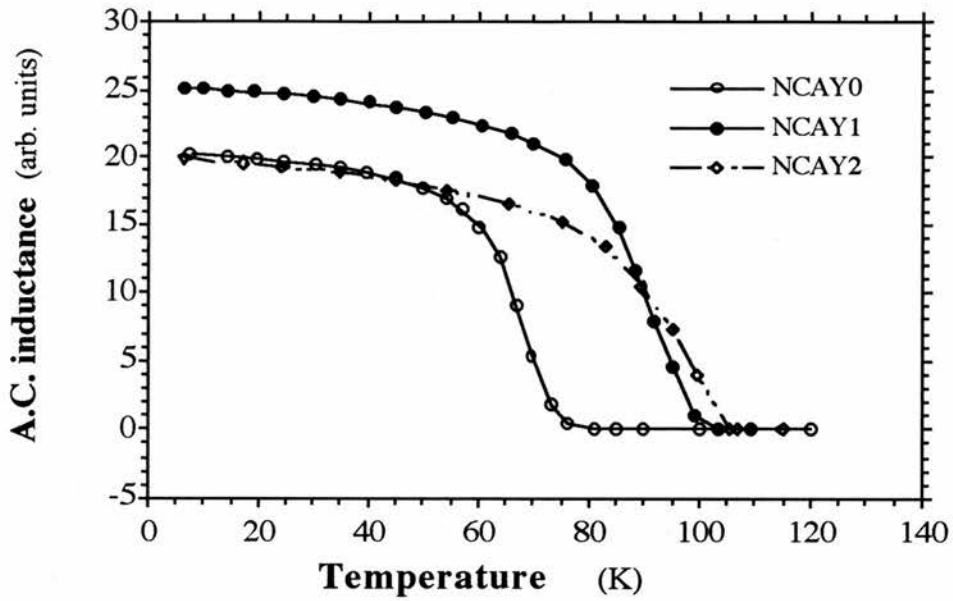


Figure 5.6 A.C. inductance vs temperature for the samples of NCAY\*.

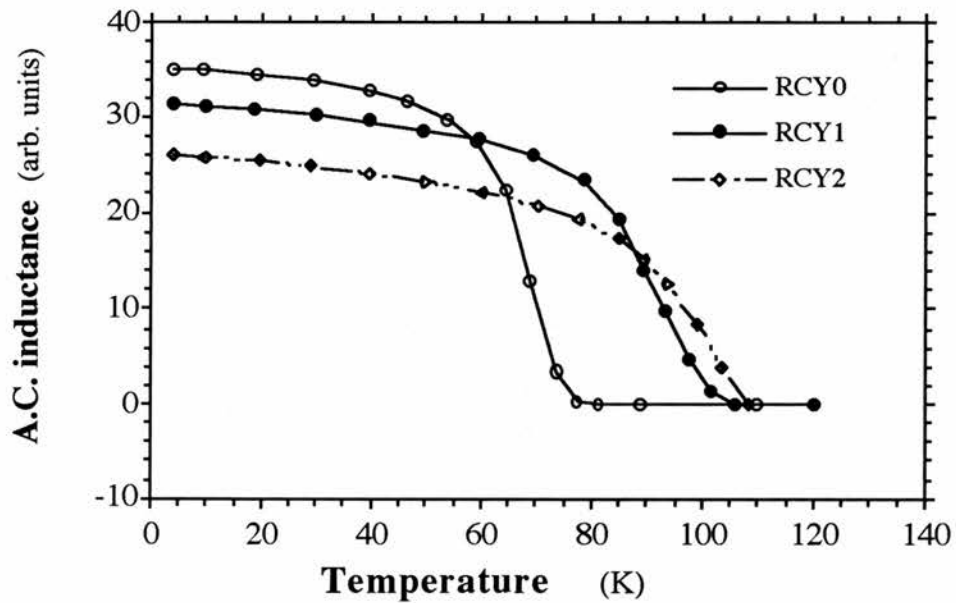


Figure 5.7 A.C. inductance vs temperature for the samples of RCY\*.

**Table 5.5.** The superconducting volume fraction on RCY\* series (for  $0 \leq * \leq 2$ ) compares with the results from ref. (1). All fraction value are in units of percent.

y in (Tl <sub>0.5</sub> Pb <sub>0.5</sub> )Sr <sub>2</sub> (Y <sub>y</sub> Ca <sub>1-y</sub> )Cu <sub>2</sub> O <sub>7-<math>\delta</math></sub>	this work	Liu's work <sup>1</sup>
0.0	53.5	55
0.1	47.8	37
0.2	39.6	33

### § 5.3 Thallium NMR at 1.5 K

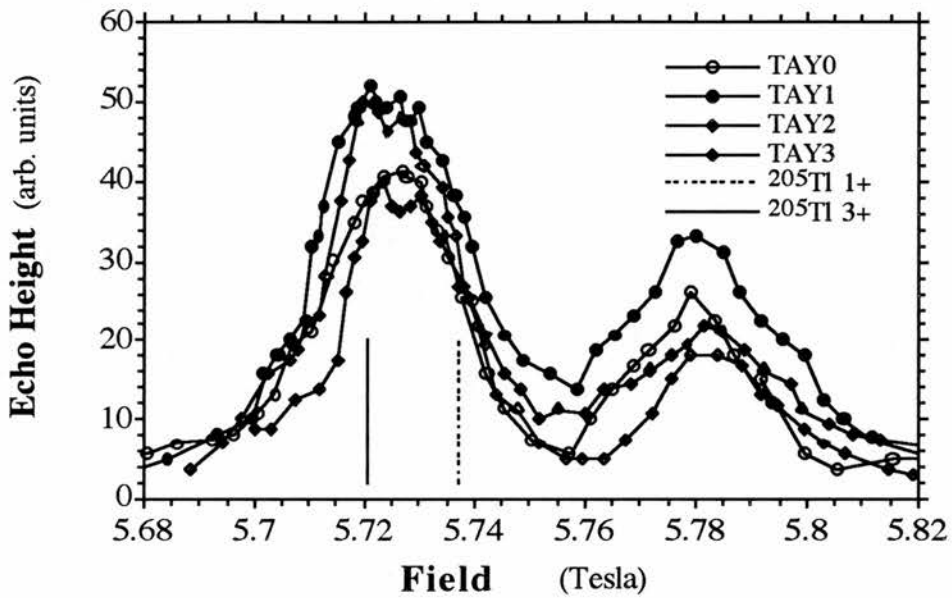
There are two isotopes of thallium in nature. Thallium-205 and thallium-203 are 70.5% and 29.5% natural abundant, respectively. Both have spin half. The NMR spectra of the both isotopes should, therefore, be free from the quadrupole effects. We have performed the NMR spectra on both isotopes at 1.5 K, measured by a field-swept spin-echo technique at 141 MHz. We could only obtain a usable signal from the samples of TAY0, TAY1, TAY2, and TAY3, and we present in Figure 5.8 (a) one set of spectra for the NMR sample aligned with its c axis parallel to the applied field  $\mathbf{B}$ , and (b) another set with the alignment axis perpendicular to the magnetic field.

As we can see from Figure 5.8, there is a considerable breadth to the lines, about 0.3 to 0.4 Tesla. If we calculate the location of the <sup>205</sup>Tl peak at this frequency, the median Tl<sup>3+</sup> position from liquids NMR is at 5.721 T ( $\gamma = 154.856 \text{ rad s}^{-1} \text{ T}^{-1}$ ) and the corresponding Tl<sup>1+</sup> is at 5.737 T ( $\gamma = 154.424 \text{ rad s}^{-1} \text{ T}^{-1}$ ). Comparing Figure 5.8 (a) and (b), we recognize that the peaks in the c parallel to  $\mathbf{B}$  data set lie at slightly higher

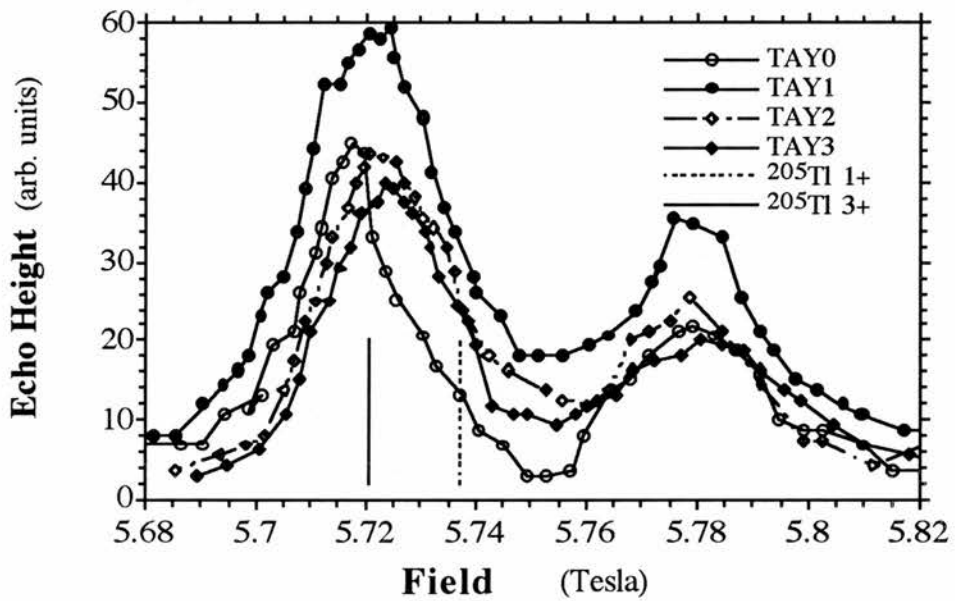
field and that there is not much change in breadth for  $c$  parallel to, as compared with  $c$  perpendicular to  $\mathbf{B}$ . There is one exception to this latter statement, where for  $c$  perpendicular to  $\mathbf{B}$  the TAYO sample has a markedly narrower profile for the  $^{205}\text{Tl}$  peak. However, if we compare the  $^{203}\text{Tl}$  peaks (right hand peaks), there is no such narrower profile. Therefore, we think that this narrower profile for the  $^{205}\text{Tl}$  peak on TAYO is possibly due to experimental error.

The thallium NMR data has exhibited very broad lines, shifted diamagnetically with respect to  $\text{Tl}^{3+}$ , which we take as our reference position<sup>7</sup>. The shift and the broadening we take as due to the bulk sample diamagnetism, and the flux line lattice in the superconducting state. Perhaps equally as important as the data presented in Figure 5.8 is the point that we could not get usable thallium spectra from any of the other samples across the entire homogeneity range.

The non-observability of Tl resonance in the  $y > 0.5$  range of concentration we ascribed initially to the antiferromagnetic polarization of these samples (see Figure 4.1). The Tl is in a lattice position where the magnetic fields from neighbouring antiferromagnetically aligned copper spins do not cancel each other out; the Tl resonance is shifted drastically. However, it is also possible that the thallium resonance would not be observed even in the absence of antiferromagnetism. We shall be proposing reasons later for the reduction in observability of the yttrium (§ 5.4), copper (§ 5.5), lead (§ 5.6) resonances at large  $y$ ; the same, or a related, reasons might also wipe out the thallium resonance. Thus, whilst antiferromagnetism can be invoked to explain the absence at 1.5 K of thallium NMR for  $y > 0.5$ , this cause would be unlikely as an explanation of the absence of thallium NMR from  $y = 0.4$  and  $y = 0.5$ . In contrast, the yttrium/calcium defect model advanced later as an explanation of the fall-off in copper NMR intensity at room temperature could be plausibly extended to thallium NMR and explain the lack of signal for all samples with  $y > 0.3$  at 1.5 K. More discussion will appear in Chapter 6.



(a)



(b)

Figure 5.8 The thallium resonance, taken at 1.5 K, for TAY\* series ( $0 \leq * \leq 3$ ). (a) the partially aligned  $c$  axis parallel to the field direction, and (b) the  $c$  axis perpendicular to the field.

## § 5.4 Yttrium-89 NMR

We have performed yttrium NMR on samples of YAY\* series with both the partially aligned c-axis parallel and perpendicular to the applied magnetic field  $\mathbf{B}$  at room temperature. However, YAY0 has no yttrium, so that there is no yttrium NMR on YAY0. Also, probably because of a too diluted yttrium concentration, the signal-to-noise rate was too low to obtain a worthwhile signal from YAY1 sample. Figure 5.9 shows the yttrium NMR spectra on YAY2 to YAY8 at room temperature for c-axis parallel to the field  $\mathbf{B}$ .

Clearly, there are two peaks for all samples for c-axis parallel to  $\mathbf{B}$ . However, there is only one peak for the c-axis perpendicular to  $\mathbf{B}$ . To explain this phenomenon, we performed a series of angle  $\theta$  dependent spectra on YAY5 shown in Figure 5.10, where  $\theta$  is the angle between the aligned c-axis and the applied field  $\mathbf{B}$  direction. As we can see from Figure 5.10, as the angle  $\theta$  changes from  $0^\circ$  (c-axis parallel to  $\mathbf{B}$ ) to  $90^\circ$  (c-axis perpendicular to  $\mathbf{B}$ ), the right hand peak is disappearing and the left hand peak remains in same position. Why does this happen? In § 5.1, the X-ray data has shown that the powder samples are partially aligned; for most of the YAY\* series samples are less than a third aligned (see Table 5.2). Therefore, a large amount of the powders still remains in a random orientation. The result is that when the sample is situated with its c-axis parallel to  $\mathbf{B}$ , the right hand peak of the spectra is contributed by the aligned fraction and the left one is contributed by the random fraction. Since the peak position of the random powder is at  $\theta = 90^\circ$  (see Figure 2.4), the peak position from the contribution of the aligned fraction will be the same, when the c-axis is perpendicular to  $\mathbf{B}$ , as contributed from the random fraction so that there is only one peak. A similar behaviour has been observed in the YBCO sample shown Figure 5.11 from ref. 4. Since the YBCO sample was aligned much better than Tl sample was, the right hand peak is much stronger in the YBCO sample for the c-axis parallel to  $\mathbf{B}$  than in the Tl sample.

The temperature and composition variation and magnitude of the position of this powder spectrum peak (Figure 5.12(a)), which is the only peak observed when c-axis is oriented perpendicular to  $\mathbf{B}$ , is in some contrast to the typical data in YBCO. In YBCO Alloul *et al*<sup>8</sup> have demonstrated that control of the hole-doping of the planes can be attained by variation of the oxygen stoichiometry. There the most obvious effect on the NMR of a change of hole-doping is the emergence of a strong temperature dependence in the shift of the yttrium resonance, with lower temperature giving a smaller magnitude of shift. In our thallium compounds, however, Figure 5.12(a) shows only a small change of shift with composition. The temperature variation is such that the magnitude of the shift gets smaller at lower temperature (recall that Alloul *et al*<sup>8</sup> and Balakrishnan *et al*<sup>9</sup> have demonstrated that the true origin of the shift is at about +200 PPM relative to a one molar solution of  $\text{YCl}_3$ ).

Figure 5.12(b) shows the second yttrium line (the right-hand peaks in Figure 5.9) as a function of  $y$ , the yttrium concentration, in the temperature range 160 to 193 K; this is the signal from the aligned fraction of our samples. Here the shifts are bigger and more concentration dependent. Again, the shifts get smaller (in magnitude) as the temperature is lowered. In the paramagnetic part of the phase diagram,  $y = 0.6, 0.7, 0.8$ , the shifts are only weakly temperature dependent.

As can be seen from Figures 5.9, 5.12(a) and (b), there are some systematic absences of data points for YAY9 and YAY10. This is because they are not detectable at room temperature. We presume that it is caused by the strong antiferromagnetic correlation on Cu-O planes causing a broad frequency spread at the yttrium site. To prove this point, we did the following experiment. As we know, the antiferromagnetic material, should have a Néel temperature. Above the Néel temperature, this material becomes a paramagnet, so we should be able to observe an NMR signal above the Néel temperature. We have monitored the yttrium NMR at the temperature of 220 K, 293 K (room temperature) 320 K, 344 K, and 370 K on YAY9 sample. For temperatures of

220 K, 293K, and 320 K, the signals were unobservable. At 344 K, the NMR signal just becomes discernible from the noise. At 370 K, we measured a good NMR spectrum. In Figure 5.13, we present three spectra at the temperatures of 320 K, 344 K, and 370 K, respectively. Therefore, the Néel temperature for the  $y = 0.9$  sample is around 340 K. For the  $y = 1.0$  sample, the Néel temperature may even be higher. Presumably, therefore, the yttrium signals for the YAY8, YAY7, and YAY6 samples would also disappear if we were to cool them below 160 K.

The yttrium linewidths are about 2 kHz over the whole concentration range apart from those itemized above where signals become unobservable. We have some preliminary spin-lattice relaxation data on the YAY3 sample between the two temperatures 160 K and 293 K, taken on the orientation-independent peak. This has a Korringa-like  $T_1T$  dependence on temperature, with a value of  $4200 \pm 500$  s K.

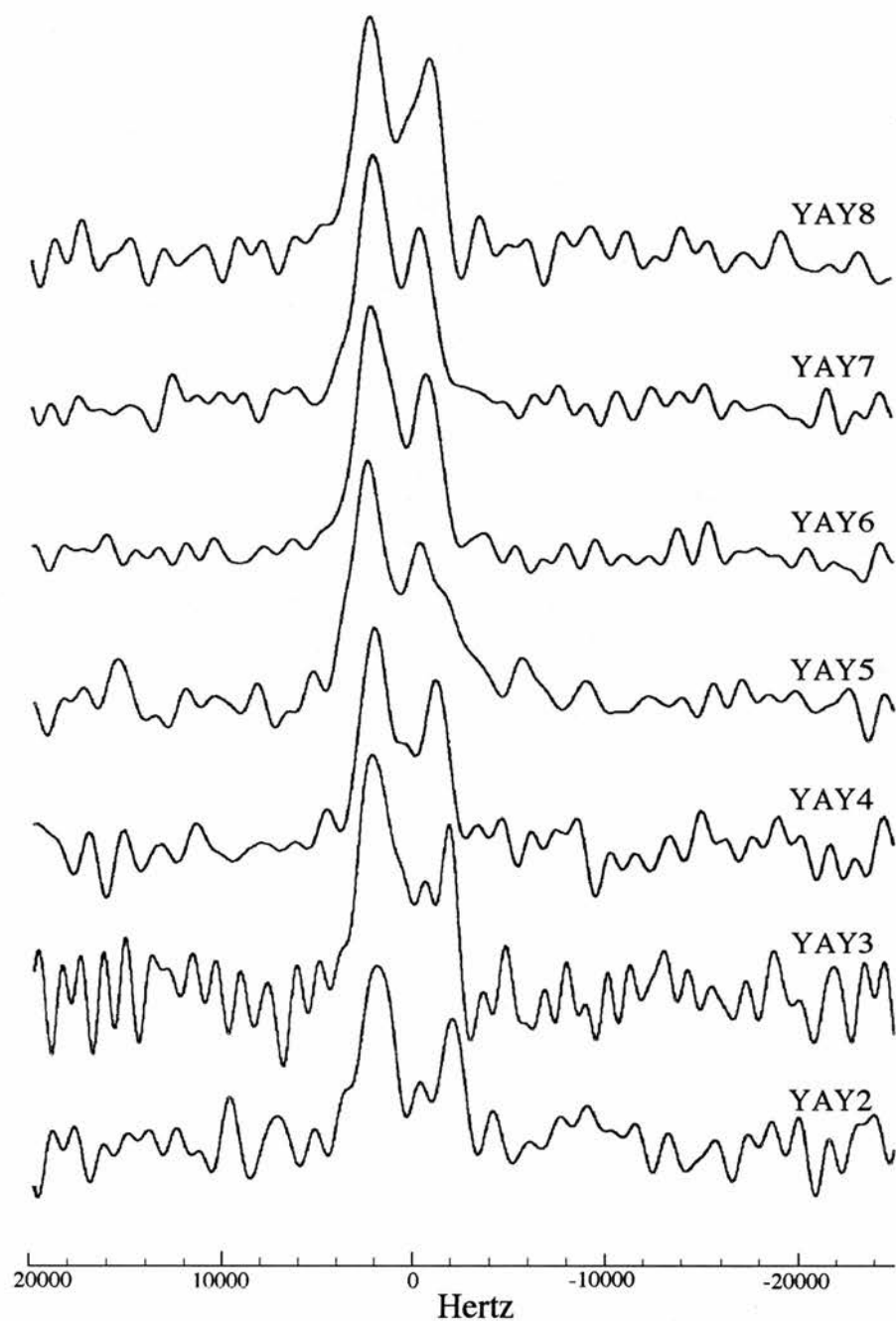


Figure 5.9 *The yttrium NMR spectra on YAY\* ( $2 \leq * \leq 8$ ) series, with c-axis parallel to the applied magnetic field direction.*

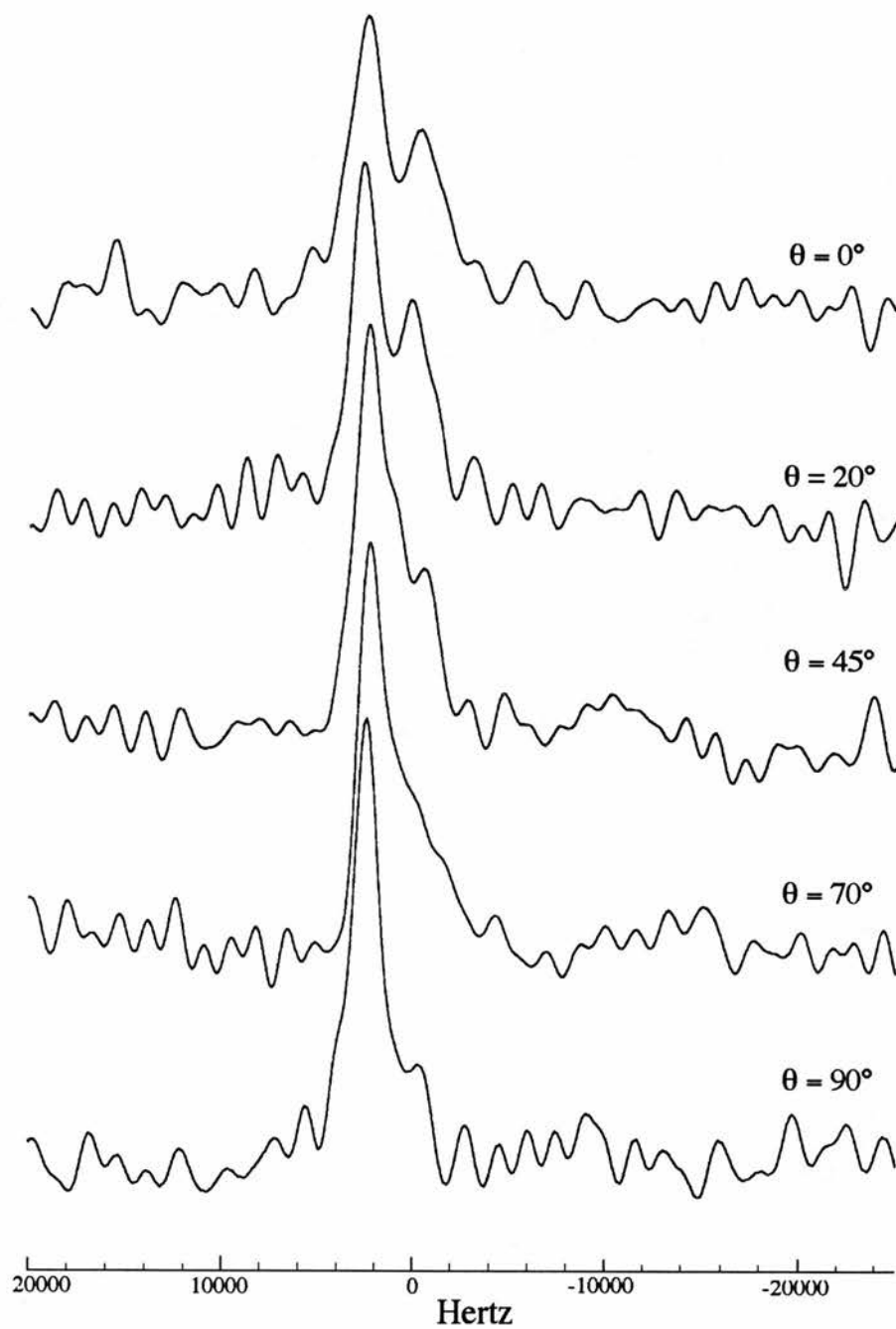


Figure 5.10 *The yttrium NMR spectra for YAY5 taken as a function of the angle of the c-axis with respect to the field direction.*

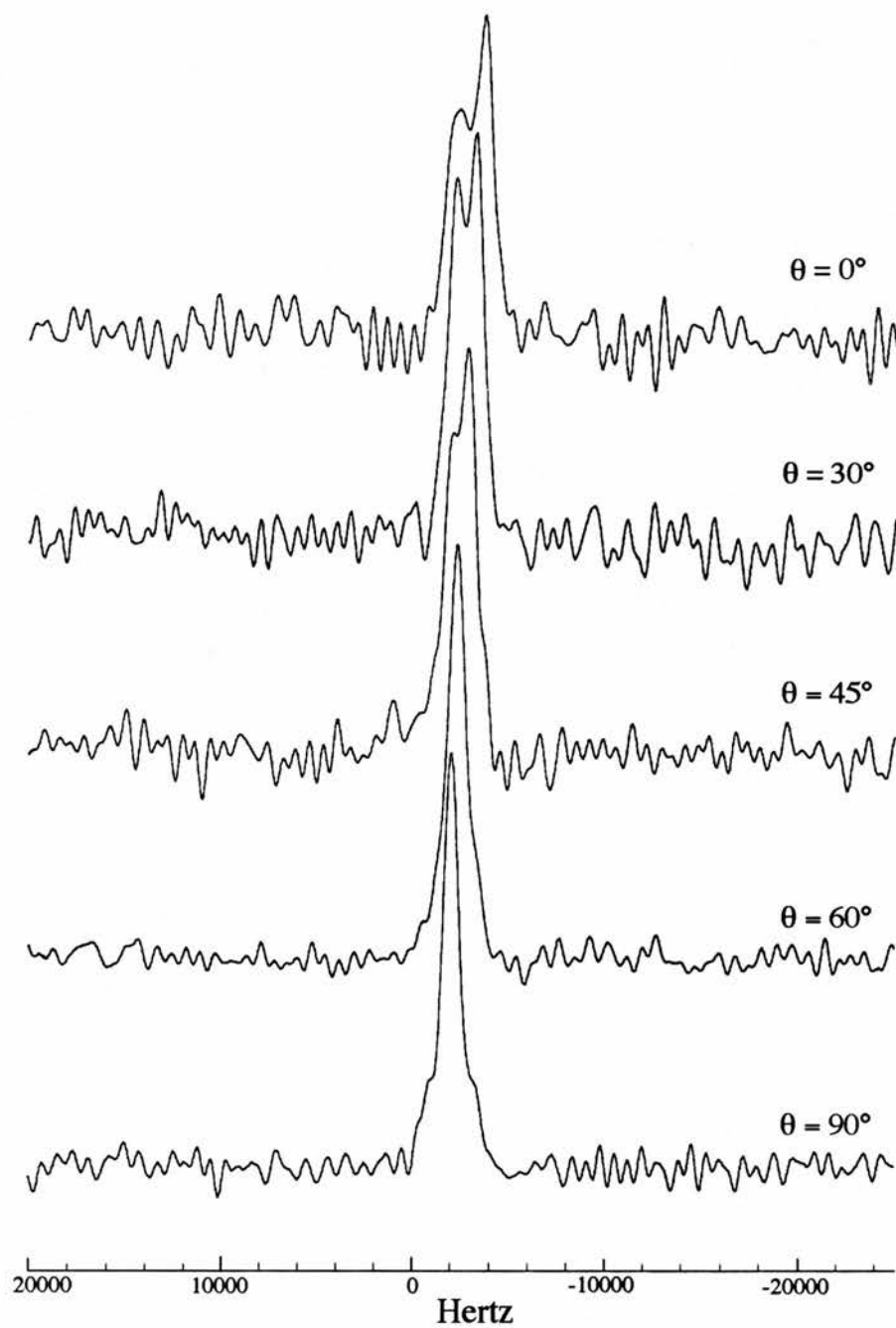


Figure 5.11 *The yttrium NMR spectra for the YBCO sample taken as a function of the angle of c-axis with respect to the field  $B$ . (After Webster<sup>5</sup>)*

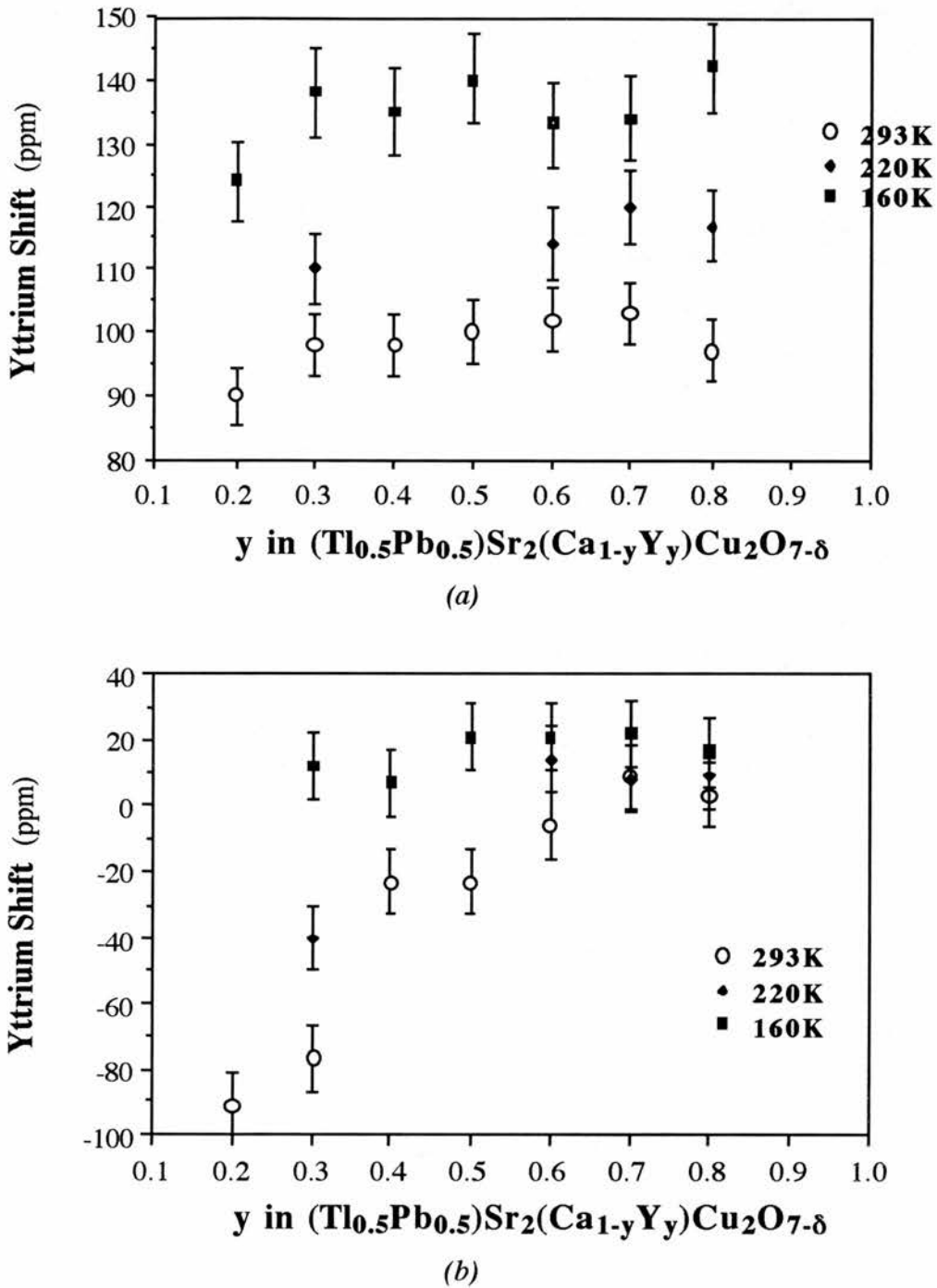


Figure 5.12 The position of the left-hand peak (a) and the right-hand peak (b) of Figure 5.9, the random powder peak of  $\text{YAY}^*$  plotted as a function of  $y$  at three temperatures. The ordinate numbers refer to the position of the peak as referenced to a 1 molar solution of  $\text{YCl}_3$ . The  $c$ -axis is here parallel to  $\mathbf{B}$ .

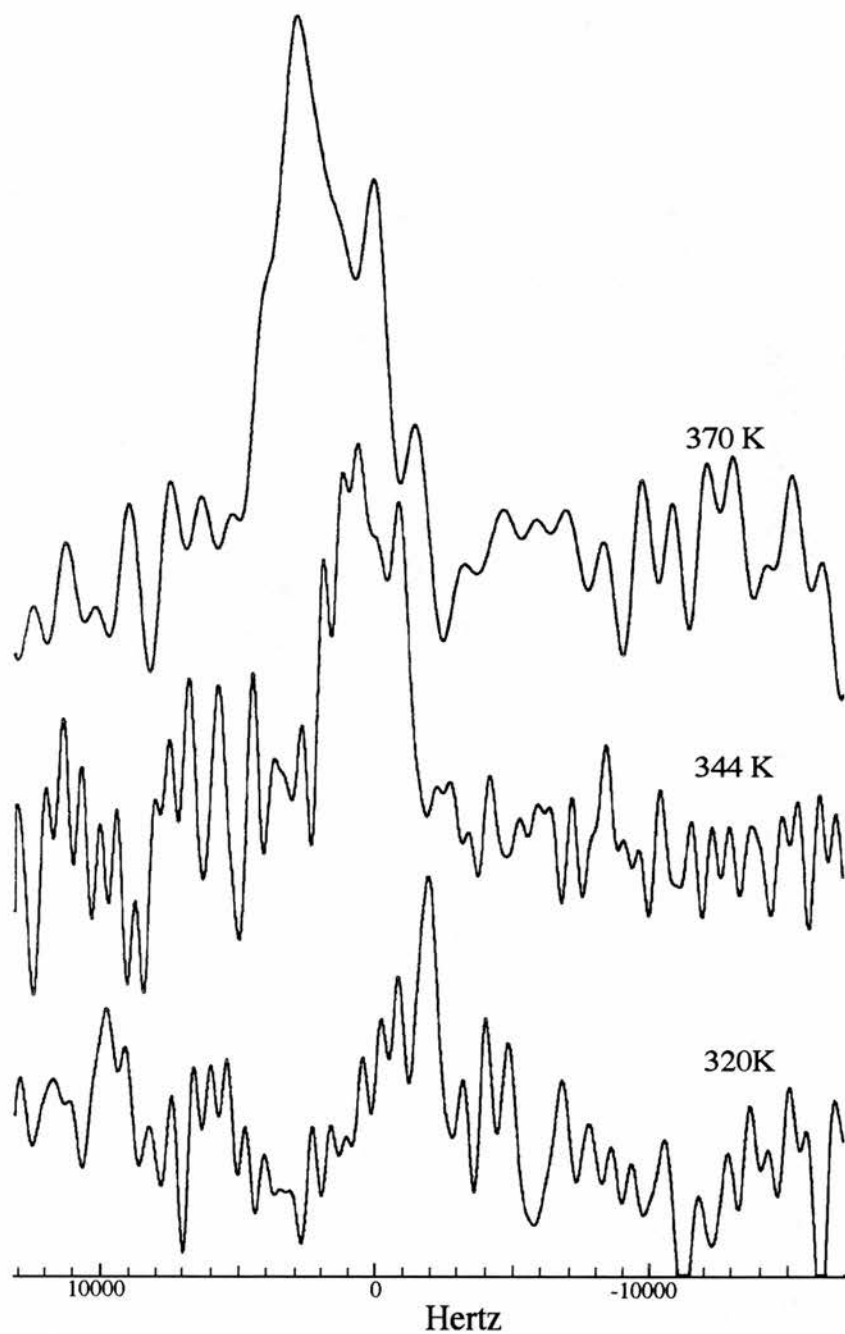


Figure 5.13 *The yttrium NMR spectra for YAY9 at three different temperatures.*

## § 5.5 Copper NMR and NQR

### § 5.5.1 NMR on CAY\* Series

Initially, we measured Cu NMR on the series of CAY\*. The spectra change by only a small amount when the c-axis of our partially aligned sample is placed perpendicular to the applied field  $\mathbf{B}$ . One seems hardly to observe the copper resonance from the aligned fraction of this series of samples.

After checking the alignment with X-rays, we found that the alignment fraction of this series samples is lower than thought initially. We then aligned another series samples (NCAY\*) and obtained better alignment, as shown by X-rays (see the first section of this Chapter).

### § 5.5.2 NMR on NCAY\* Series

As an example, Figure 5.14 shows the copper-63 NMR spectra on partially aligned sample (NCAY0) with different angles between the marked line on the sample and the applied magnetic field  $\mathbf{B}$ . The marked line lies near the actual aligned c-axis direction ( $\pm 10^\circ$ ). As one can see from the diagram, the spectra still hardly show any evident orientation dependence. This indicates that the alignment fraction is somehow less than we estimated from the X-ray data. One possible explanation is that there is some aggregation of particles within the sample, forming large disoriented regions to which the X-rays are not sensitive. Thus the X-rays preferentially sample well-dispersed, and therefore well-aligned, regions of the sample.

In order to observe the orientation dependence of the aligned fraction, we set another series of samples in zero magnetic field (other conditions were the same as for the aligned samples), labelled as RCY\*, where R stands for random. We then measured

the NMR spectra on each of these randomly oriented samples. The spectrum for RCY0 is shown in Figure 5.14 (bottom). Assuming the partially aligned spectra were composed of spectra from an aligned fraction and the random fraction, and also assuming that the random fraction spectra have the same shape as the random sample's spectra, we therefore have:

$$S_a = S_p - \rho \times S_r \quad (5.9)$$

where  $S_a$  is the 'pure' aligned spectrum in one direction,  $S_p$  is the spectrum obtained from the experimental data of the partially aligned sample (NCAY\*) in that direction,  $S_r$  is the spectrum from the experimental data of the random sample (RCY\*), and  $\rho$  is a factor depending on the degree of alignment in the particular sample. To obtain the optimum values of  $\rho$ , we adjusted its value until the best base lines of  $S_a$ , the 'pure' aligned spectra emerged. (where 'the best line' means that each data point on the base line should be above, but as near as possible to, zero, and the value of  $\rho$  should not vary with orientation, *i.e.*  $\rho$  can only have one value for each particular sample). The results of this deconvolution procedure for the samples of  $y = 0.0, 0.1, 0.2, \dots 0.7$  are shown in Figures 5.15, 5.16, 5.17, ... 5.22, respectively. Clearly, the resonance frequency (the peak position) is orientation dependent. We list in Table 5.6 the values of the fitting parameter,  $\rho$ , obtained by this procedure.

The signal to noise ratio was very poor for the NCAY8 sample, so we did not measure the orientation spectra. Again, we could not detect a copper spin echo signal on the samples of  $y = 0.9$  and  $1.0$ .

As can see from Figure 5.19 for NCAY4 spectra, there are two peaks in some orientation spectra. Comparing all of the spectra, we think that the difference from  $y = 0.4$  to others is the impurity phase which has been shown in X-rays (see Figures 5.1, 5.2 and 5.3).

**Table 5.6.** Listing of the fitting parameter,  $\rho$ , in equation (5.9).

Samples	$\rho$
NCAY0	0.855
NCAY1	0.939
NCAY2	0.8
NCAY3	0.75
NCAY4	0.67
NCAY5	0.84
NCAY6	1.0
NCAY7	1.0

### § 5.5.3 $T_1$ and $T_2$ of Cu NMR

We attempted to measure spin-lattice relaxation time  $T_1$  of Cu NMR using the program called XDNMRT1.PC. This ‘comb-echo’ sequence is useful when  $T_2 \ll T_1$  for very broad resonance lines; unfortunately we found it very difficult on our sample to effectively saturate the Cu nuclear magnetisation with the comb. We could not obtain a worthwhile value of  $T_1$ . From our measurement, we could only conclude that the  $T_1$  must be shorter than milliseconds.

The spin-spin relaxation time  $T_2$  has been measured on NCAY\* ( $0 \leq * \leq 8$ ) series samples at room temperature. Figure 5.23 shows some of the experimental data (spin

echo area as a function of  $\tau$ , the time between two pulses shown in Figure 3.9). The solid lines in Figure 5.23 are the exponential fitting curve. The equation of the fitting curve is:

$$S = S_0 \exp\left(-\frac{2\tau}{T_2}\right) \quad (5.10)$$

As can see, all the lines

obey the exponential law beautifully. The computer calculates the fitting parameters ( $S_0$  and  $T_2$ ).

In Figure 5.24, we plot  $T_2$  as a function of  $y$  the yttrium concentration. Evidently,  $T_2$  decreases as the yttrium concentration is increased across the whole detectable region. One possible explanation is that as  $y$  increases the antiferromagnetic interaction is getting stronger, so broadening the spectra and shortening the  $T_2$ .

#### § 5.5.4 Copper NQR

We have performed copper nuclear quadrupole resonance on this system. Figure 5.25 shows the NQR spectrum on  $y = 0.0$  (YAYO) sample. The quadrupole resonance frequency is about 21.0 MHz. Unfortunately, the NQR signal are very weak for the  $y = 0.1$  and  $0.2$  samples; the resonance frequencies however were about 20.8 MHz for both, which agrees with Zhdanov *et. al.*<sup>10</sup>. For the rest of the samples, the signal were too weak to observe by this technique.

Since the spectrum is very broad, to obtain better precision, we differentiated the spectrum. The resonance line should lie on the point where the derivative equals to 0 (see Figure 5.25, the dashed line is the derivative for the solid curve).

## § 5.6 Lead NMR

### § 5.6.1 NMR Spectra

Initially, we measured the lead NMR on NCAY0 sample with two orientations and on the RCY0 sample (see Figure 5.26). Clearly, the resonance frequency for c-axis parallel to the magnetic field  $\mathbf{B}$  is smaller than that for c-axis perpendicular to  $\mathbf{B}$ . Since the resonance frequency for reference ( $\text{Pb}(\text{NO}_3)_2$  solution) is at 104.321MHz, the Knight shift is positive, but the axial shift (see equation (2.23b)) is negative. Since all the samples are only partially aligned, we cannot regard the resonance frequencies in Figure 5.26 as the real ones for the particular orientation. To obtain the true resonance frequency, we attempted to follow the method as we did on copper NMR. However, we could not deconvolute worthwhile spectra to show the resonance frequencies. The reason for this failure is that the spectra have too small an angular dependence compared with the spectra width; after subtracting, experimental error dominates the spectral shape.

Figure 5.27 shows lead NMR spectra on the samples of RCY\* series ( $0 \leq * \leq 8$ ) at room temperature. Figures 5.28 and 5.29 present the resonance frequency and the integrated area of the spectra obtained from Figure 5.27 as a function of the yttrium composition content,  $y$ , respectively. As can see from Figure 5.28, the resonance frequency (Knight shift) of the random sample is decreasing as  $y$ , the yttrium concentration, is increased in the metal region ( $0.0 \leq y \leq 0.5$ ). However, in the non-metal region ( $y \geq 0.6$ ), Knight shift is almost independent as  $y$  changes. The behaviour of the intensity of the integrated area of the spectrum as a function of  $y$  also can be classified into two groups as shown in Figure 5.29, *i.e.* the metal region and the non-metal region. In both regions the intensity of the integrated area is decreasing as  $y$  is increased. However, it drops rapidly when the phase changes. We have noticed that in

the metal region the integrated area of  $y = 0.4$  (RCY4) is much smaller expected an effect, which might be caused by the impurity phase.

### § 5.6.2 $T_1$ and $T_2$ of Lead NMR

We have also attempted to measure spin-lattice relaxation time  $T_1$  of Pb NMR. Again, the similar reason as for Cu (see § 5.5.3), we could not obtain a worthwhile value of  $T_1$ . However, comparing with the copper measurement, the value of  $T_1$  is bigger.

The spin-spin relaxation time ( $T_2$ ) of Pb NMR has been measured at room temperature. Figure 5.30 shows spin echo area as a function of  $\tau$ , the time between two pulses just as for Cu. However, the data no longer fits to the exponential curve (the Lorentzian function equation 5.10). It can be fitted to a Gaussian function as:

$$S = S_0 \exp \left[ -\frac{1}{2} \left( \frac{2\tau}{T_{2G}} \right)^2 \right] \quad (5.11)$$

where  $T_{2G}$  characterizes the relaxation.

Using the computer to fit the experimental data to obtain the best fitting curves shown in Figure 5.30 where the separate points are experimental data and the solid lines are the best fitting curves, we can obtain the parameters  $S_0$  and  $T_{2G}$  from the computer.  $T_{2G}$  as a function of yttrium concentration is plotted in Figure 5.31.

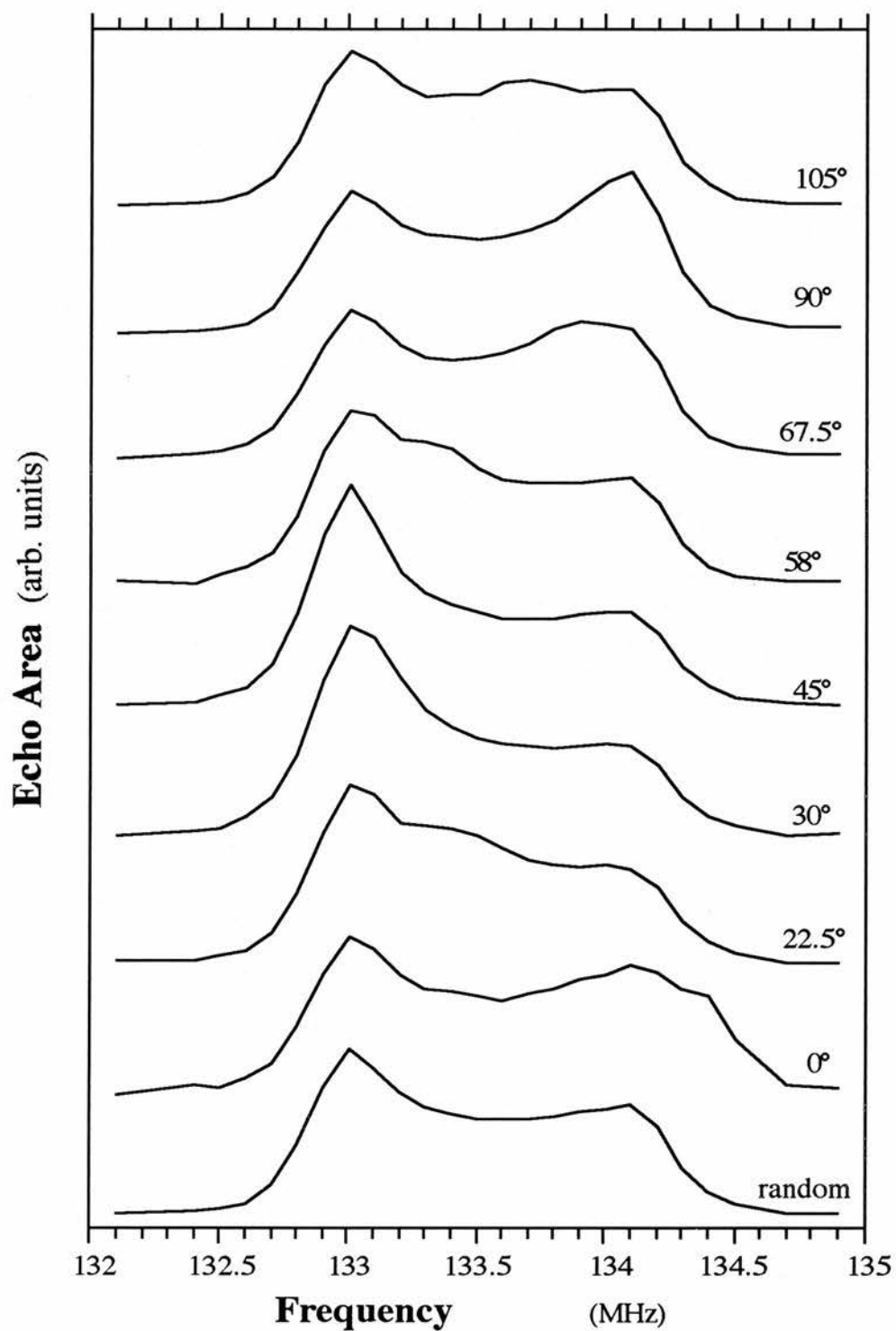


Figure 5.14 *Copper-63 NMR spectra on both partially aligned and random samples of NCA $Y^*$  series at room temperature.*

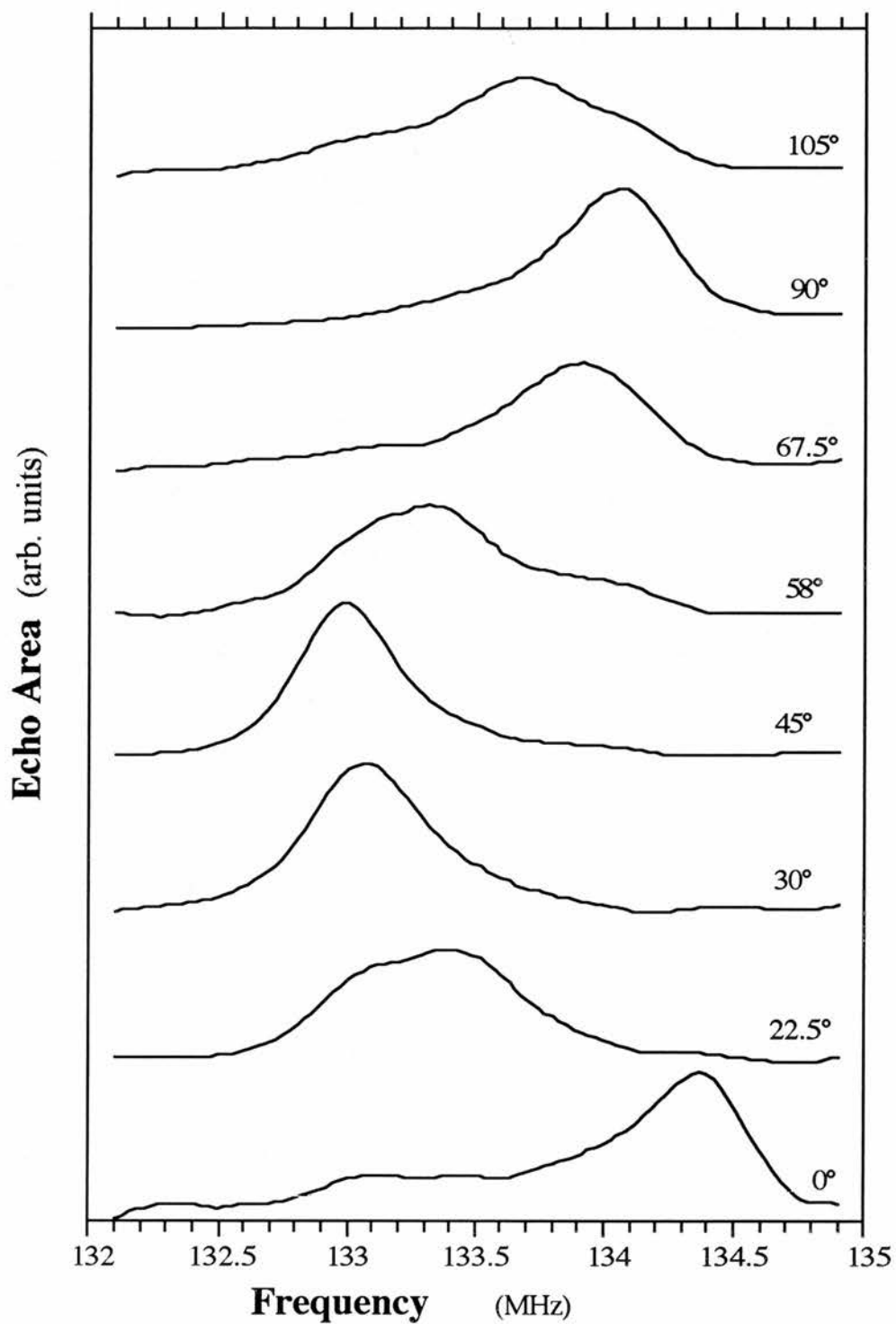


Figure 5.15 The 'pure' aligned spectra obtained by subtracting the random fraction from the partially aligned spectra on NCAYO at RT.

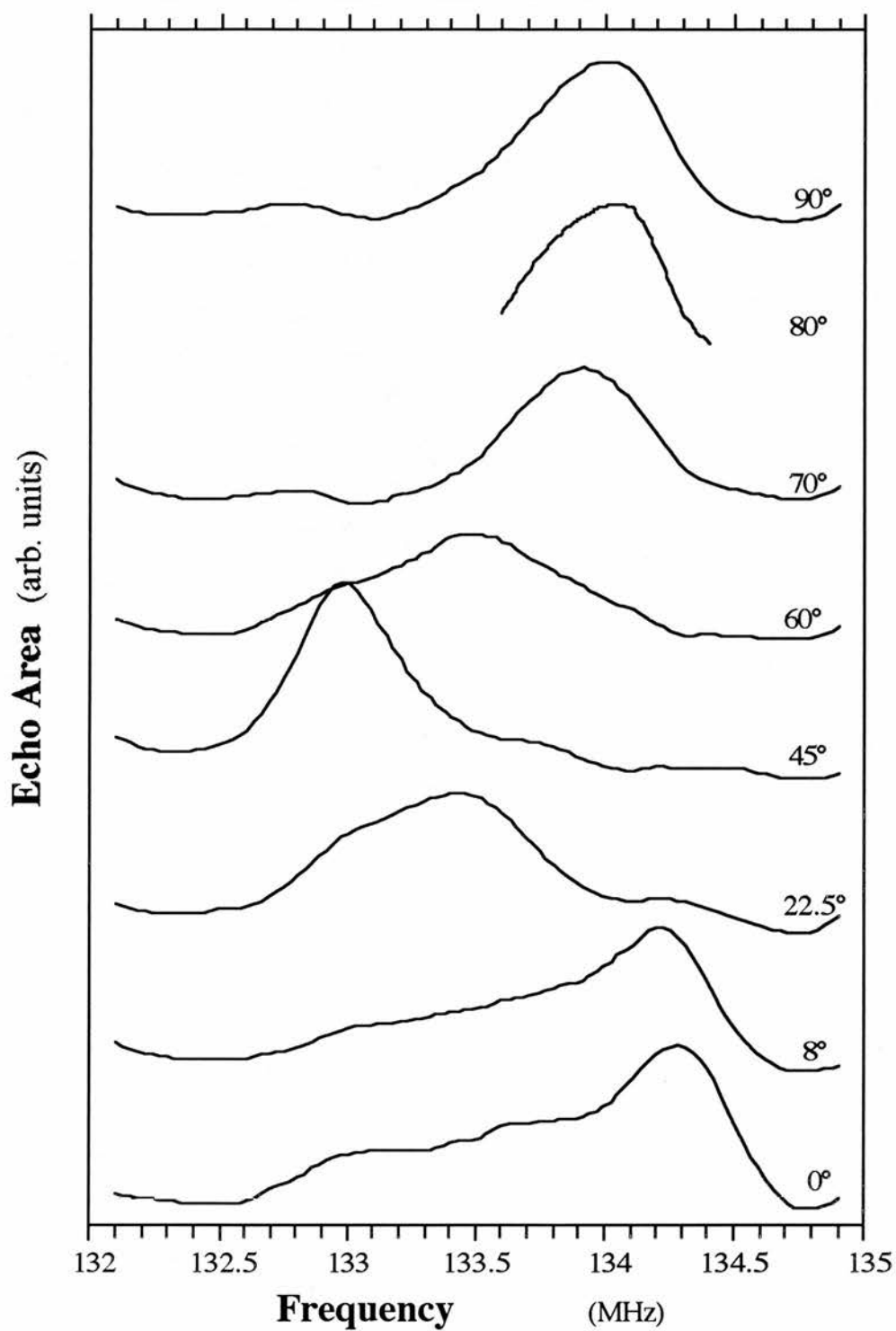


Figure 5.16 *The 'pure' aligned spectra obtained by subtracting the random fraction from the partially aligned spectra on NCAY1 at RT.*

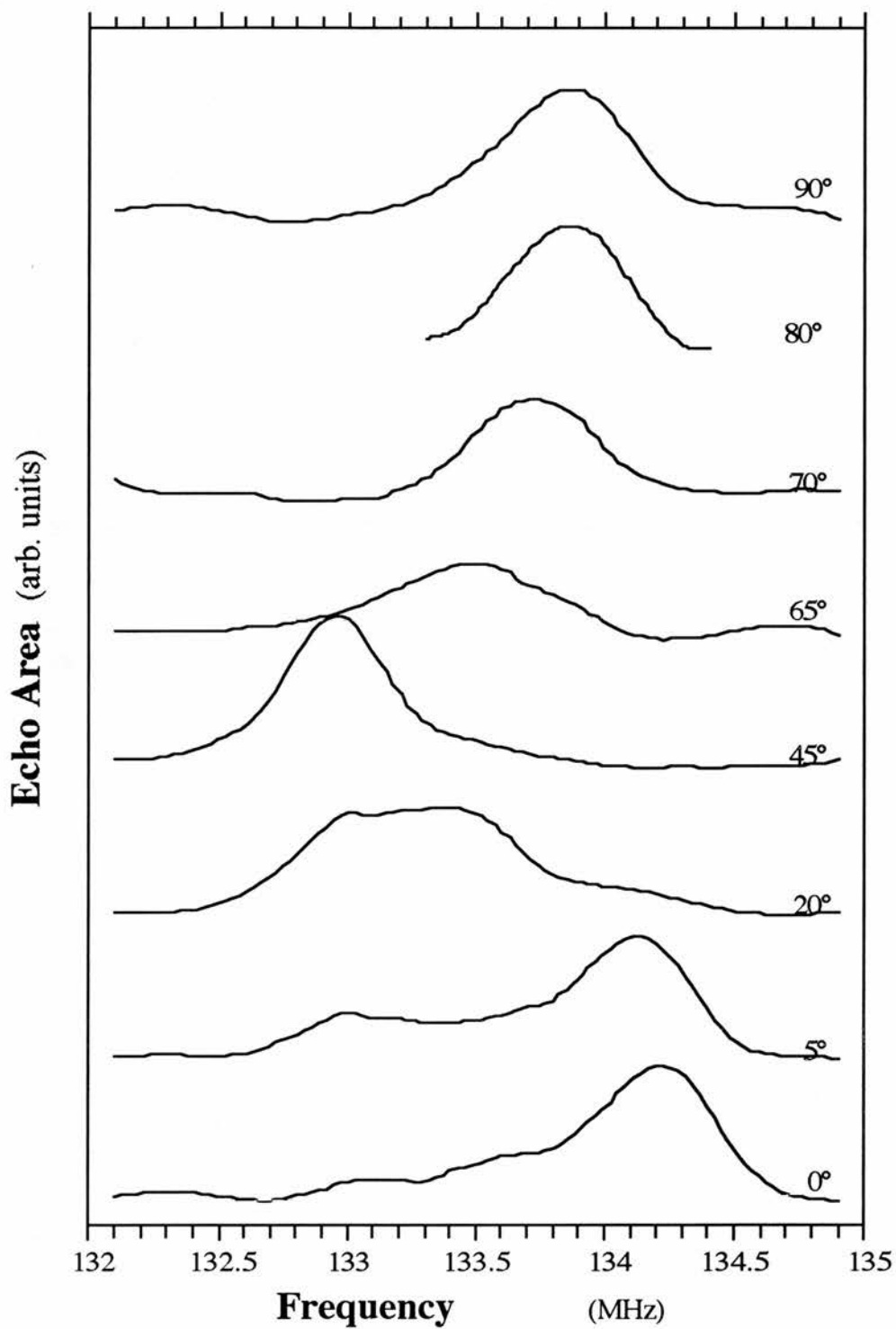


Figure 5.17 The 'pure' aligned spectra obtained by subtracting the random fraction from the partially aligned spectra on NCA Y2 at RT.

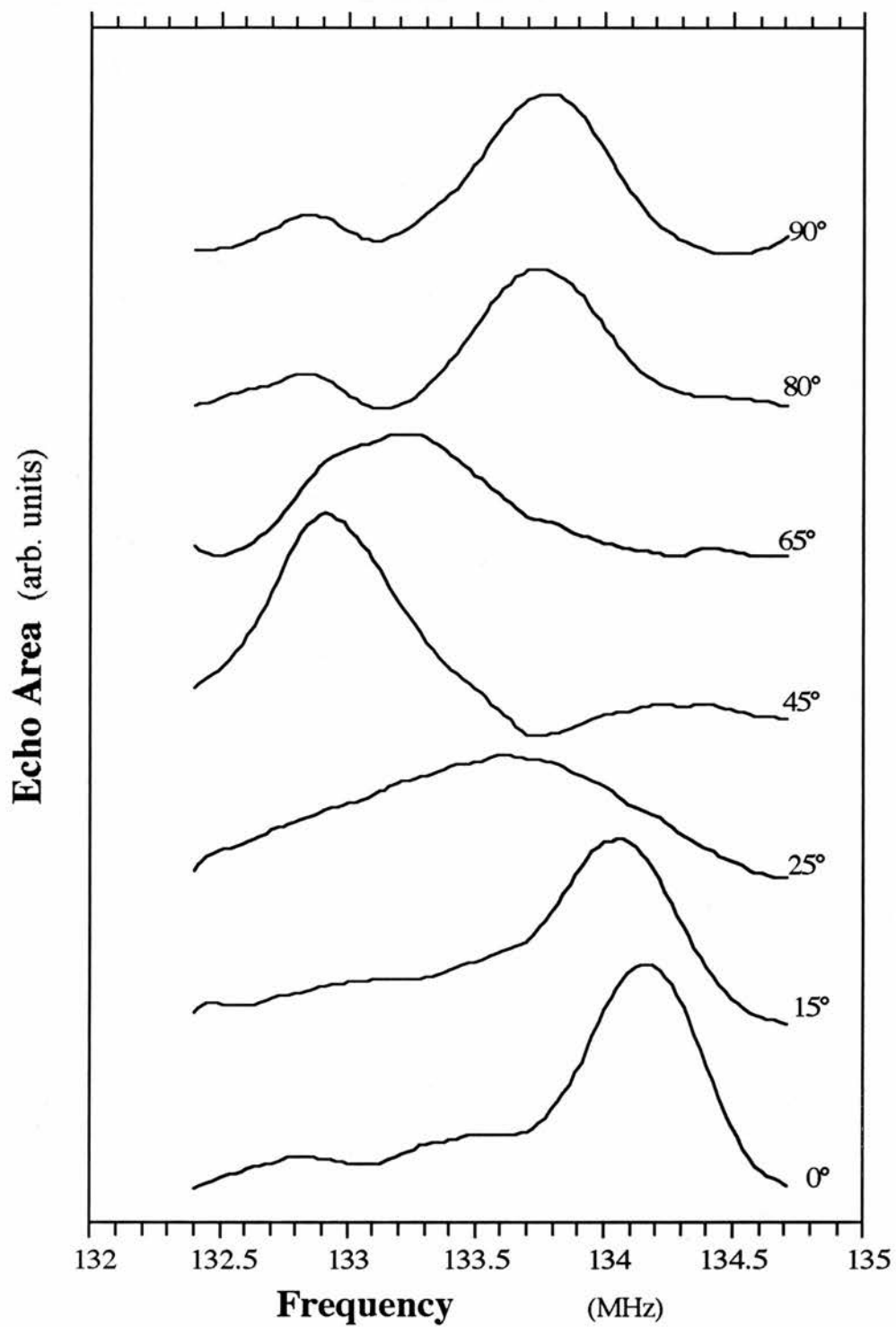


Figure 5.18 The 'pure' aligned spectra obtained by subtracting the random fraction from the partially aligned spectra on NCA Y3 at RT.

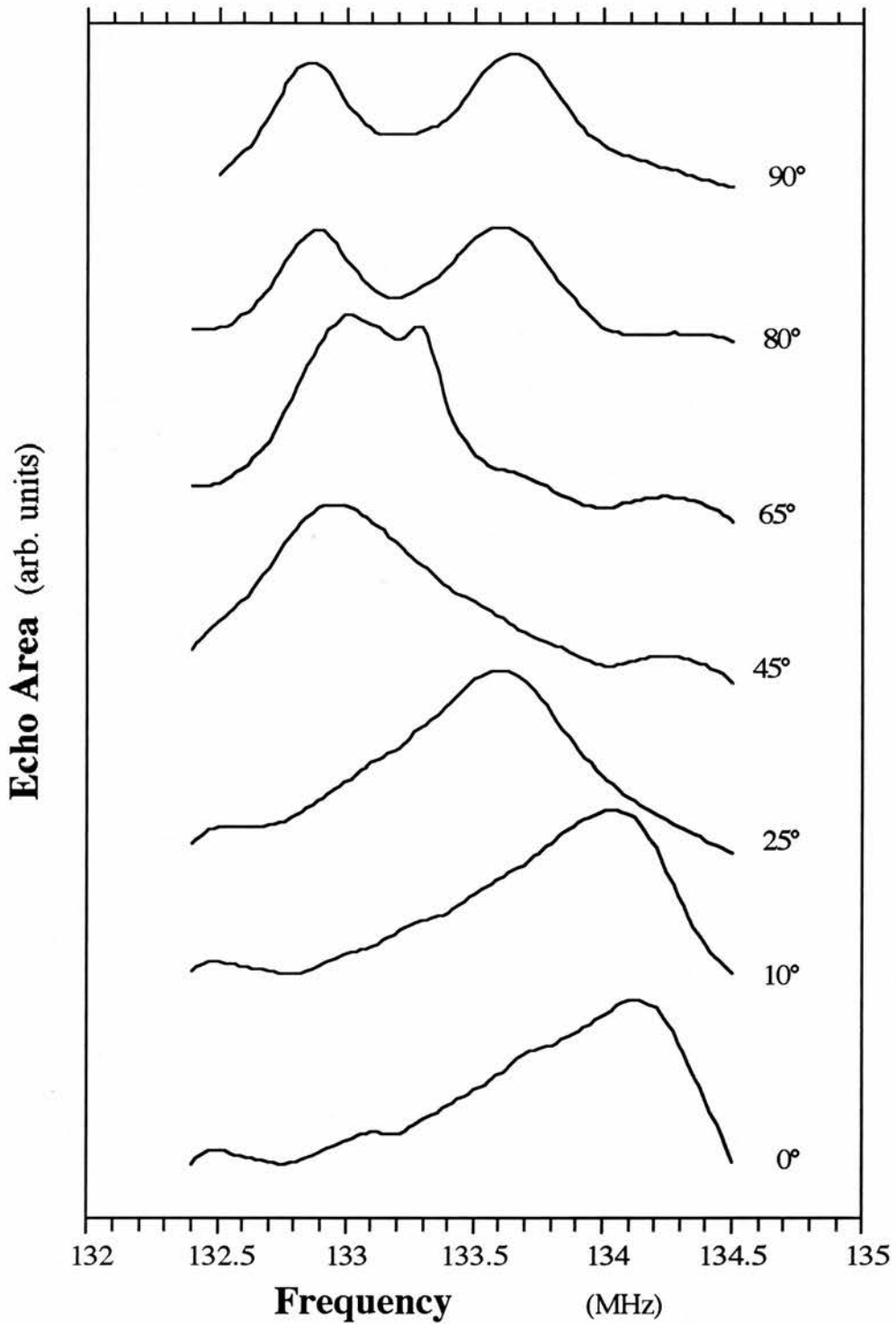


Figure 5.19 The 'pure' aligned spectra obtained by subtracting the random fraction from the partially aligned spectra on NCA4 at RT.

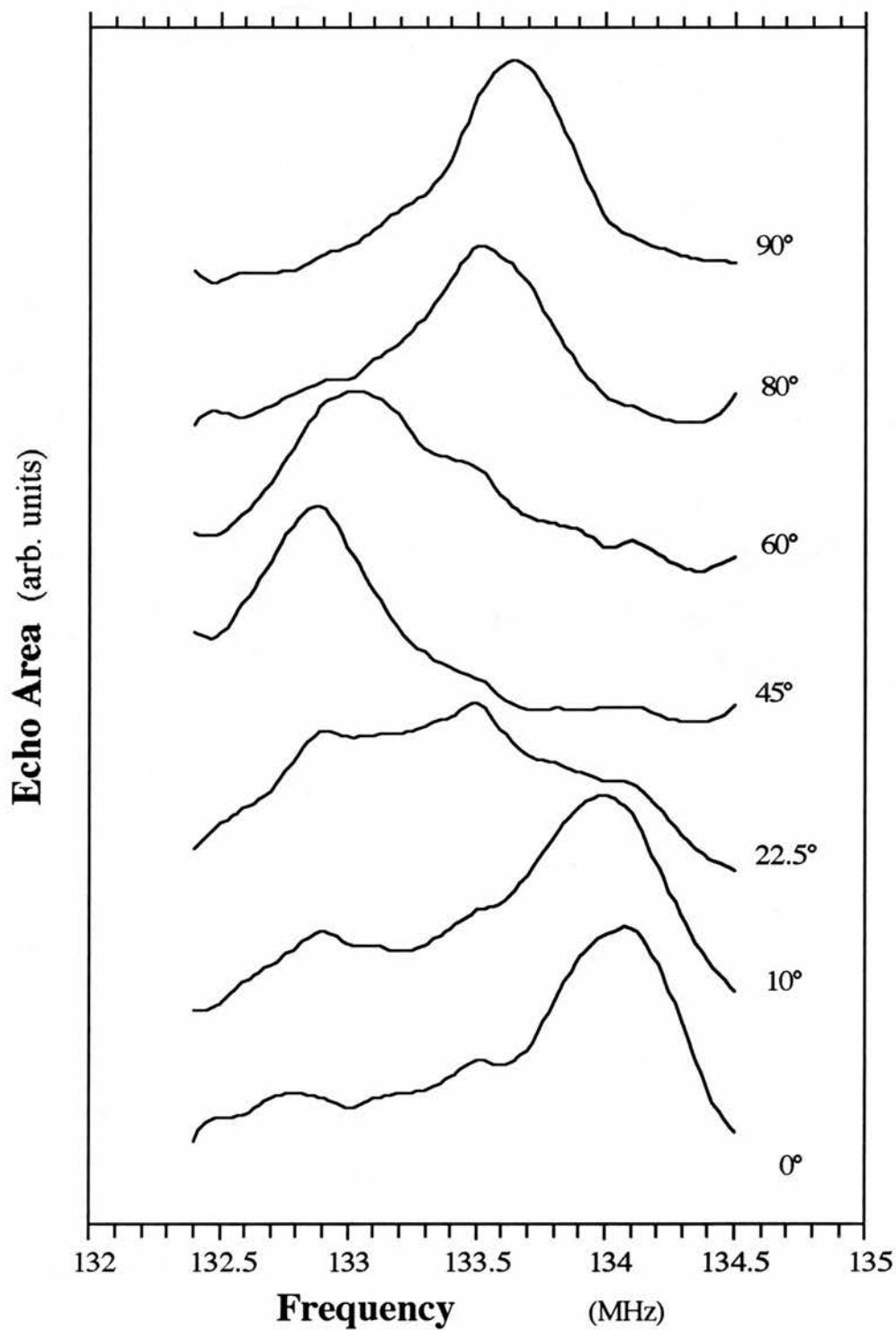


Figure 5.20 The 'pure' aligned spectra obtained by subtracting the random fraction from the partially aligned spectra on NCAY5 at RT.

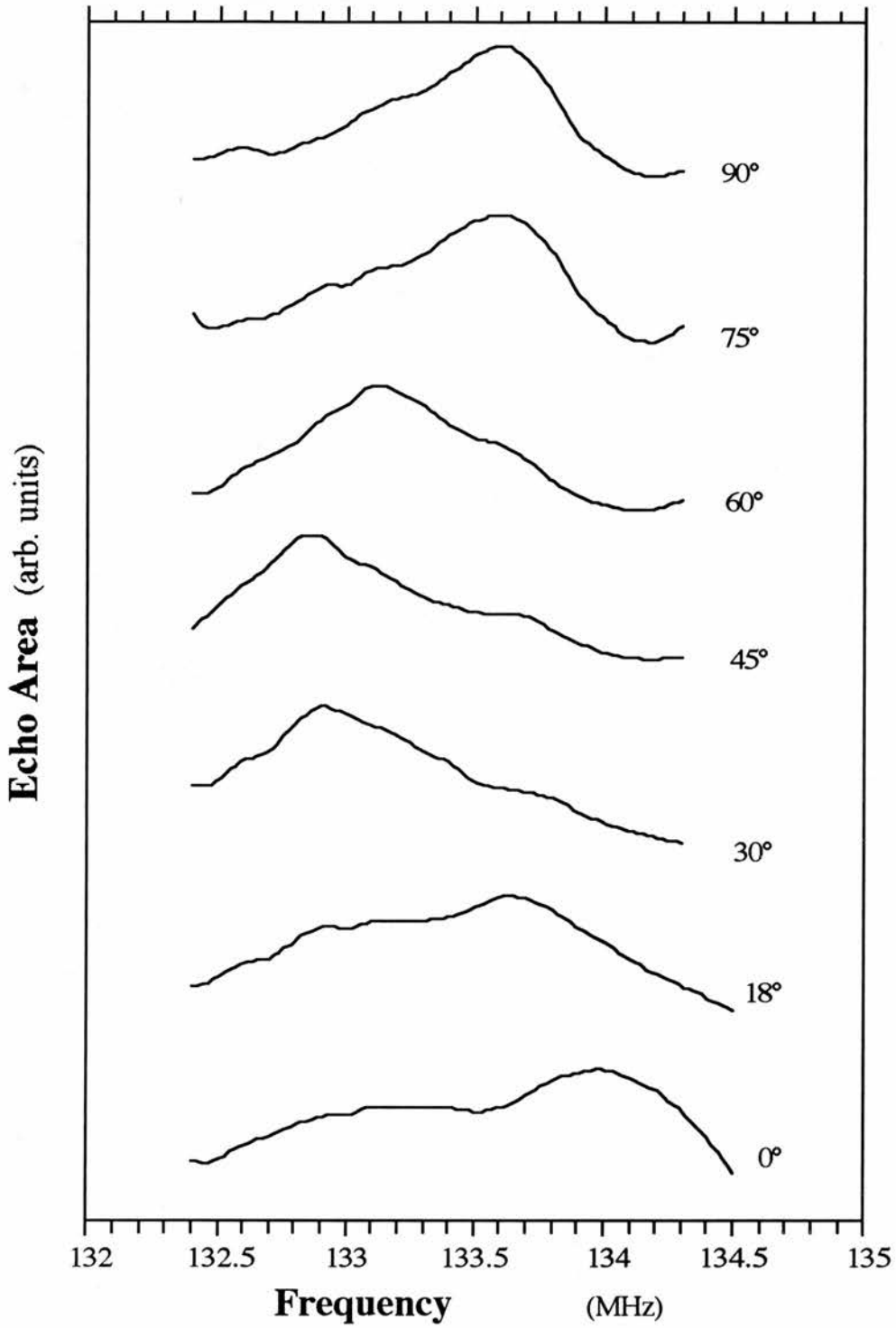


Figure 5.21 The 'pure' aligned spectra obtained by subtracting the random fraction from the partially aligned spectra on NCAY6 at RT.

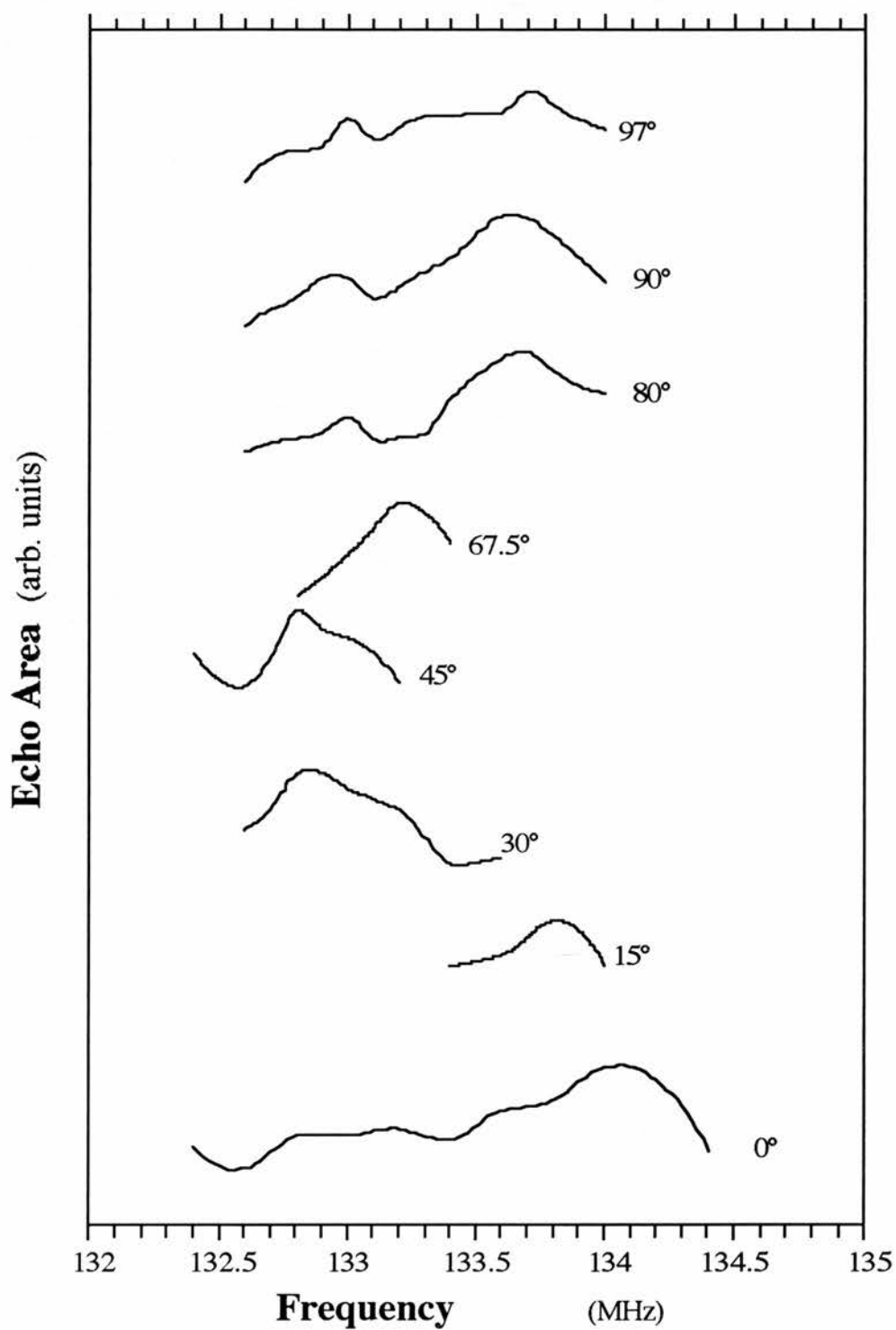


Figure 5.22 The 'pure' aligned spectra obtained by subtracting the random fraction from the partially aligned spectra on NCA7 at RT.

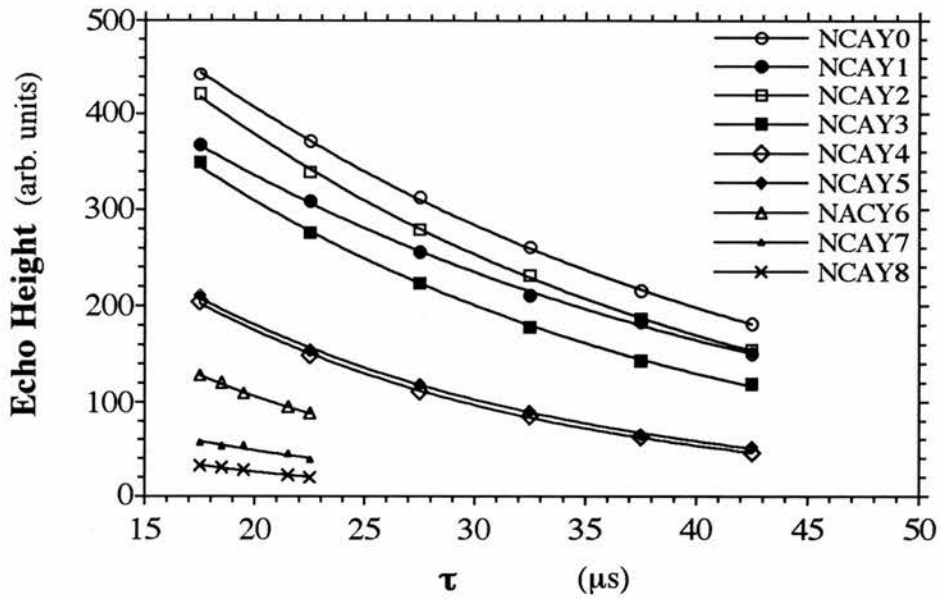


Figure 5.23 *Copper NMR  $T_2$  measurement at RT, the separate points are experimental data and the solid lines are exponential fitting curves.*

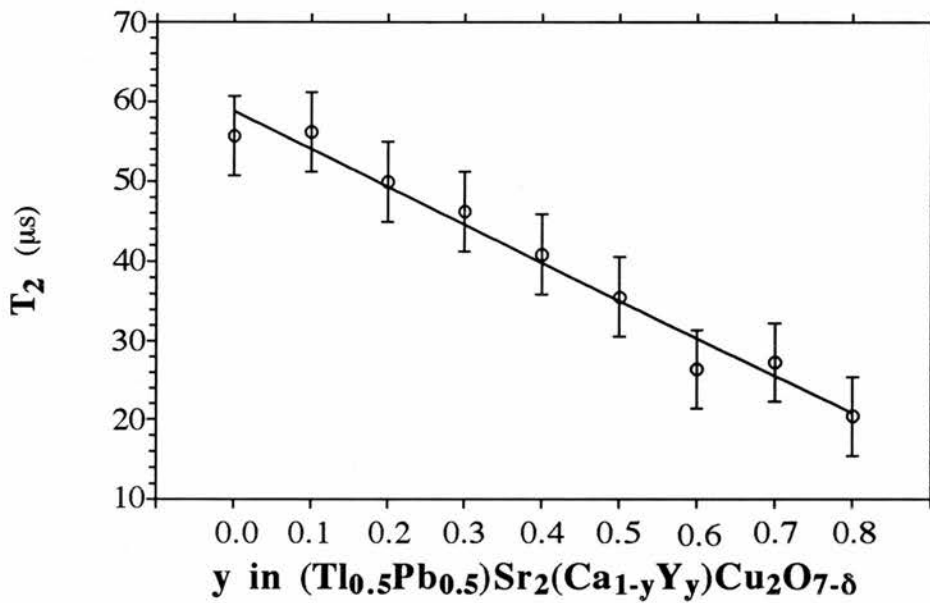


Figure 5.24 *Copper spin-spin relaxation time  $T_2$  as a function of  $y$ , the yttrium concentration at RT.*

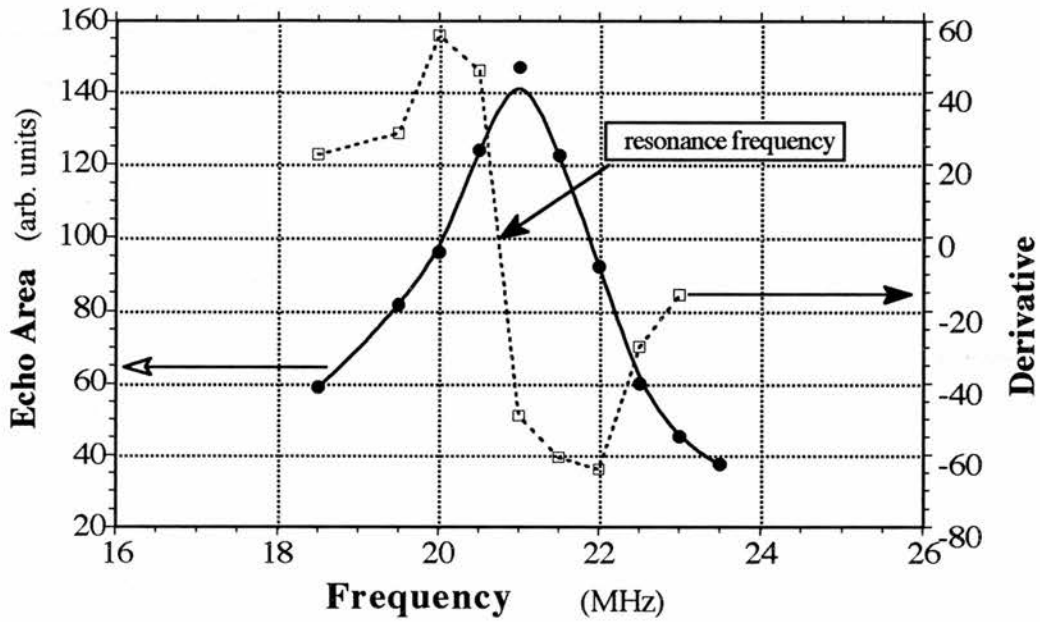


Figure 5.25 *Copper-63 NQR spectrum on YAY0 sample (the solid line) at RT. The dashed line is the derivative for the solid curve (spectrum).*

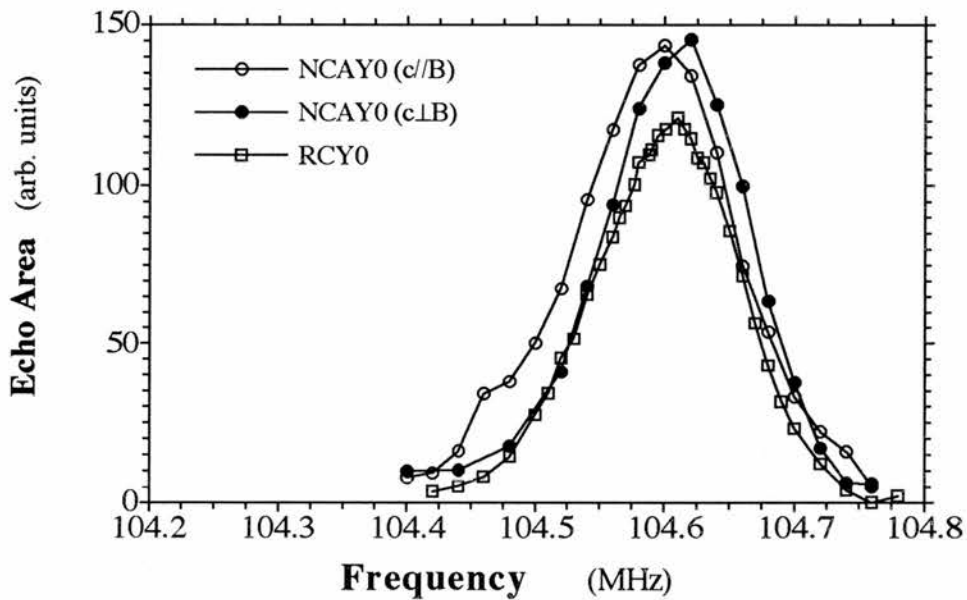


Figure 5.26 *Lead NMR spectra on NCAY0 with  $c$ -axis parallel to  $B$  and  $c$ -axis perpendicular to  $B$ , and RCY0 sample at 11.74 T and RT.*

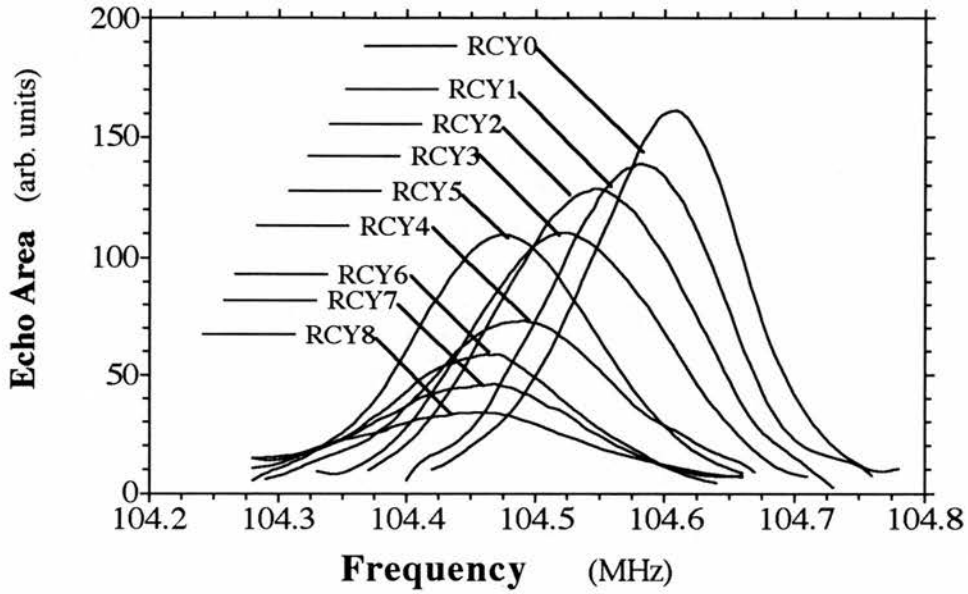


Figure 5.27 Lead NMR spectra on the samples of RCY\* series at RT.

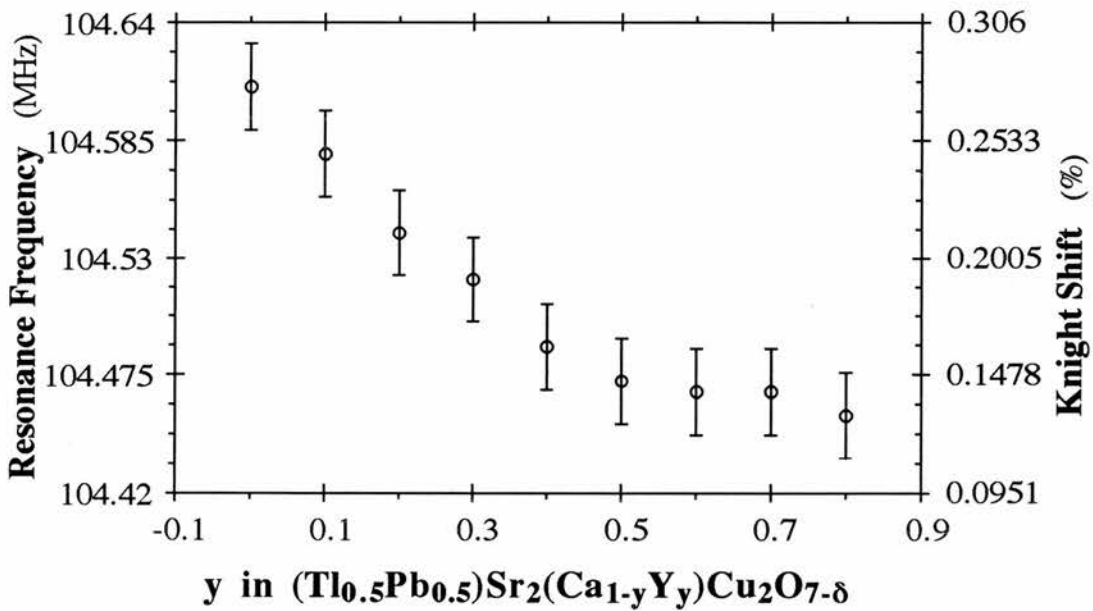


Figure 5.28 Resonance frequency (Knight shift) of the random powder samples as a function of yttrium concentration at RT.

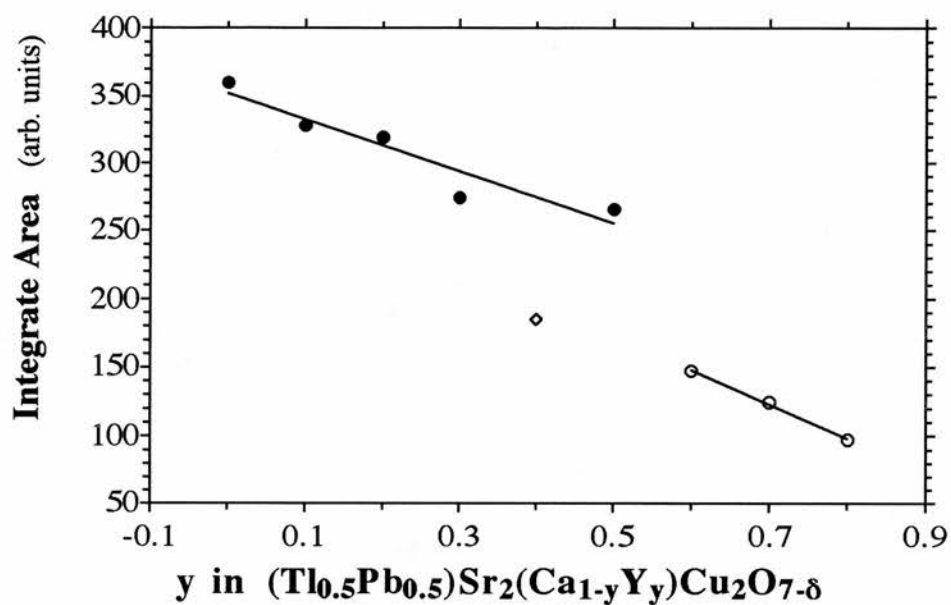


Figure 5.29 The integrated area of the spectra versus  $y$ , the yttrium concentration.

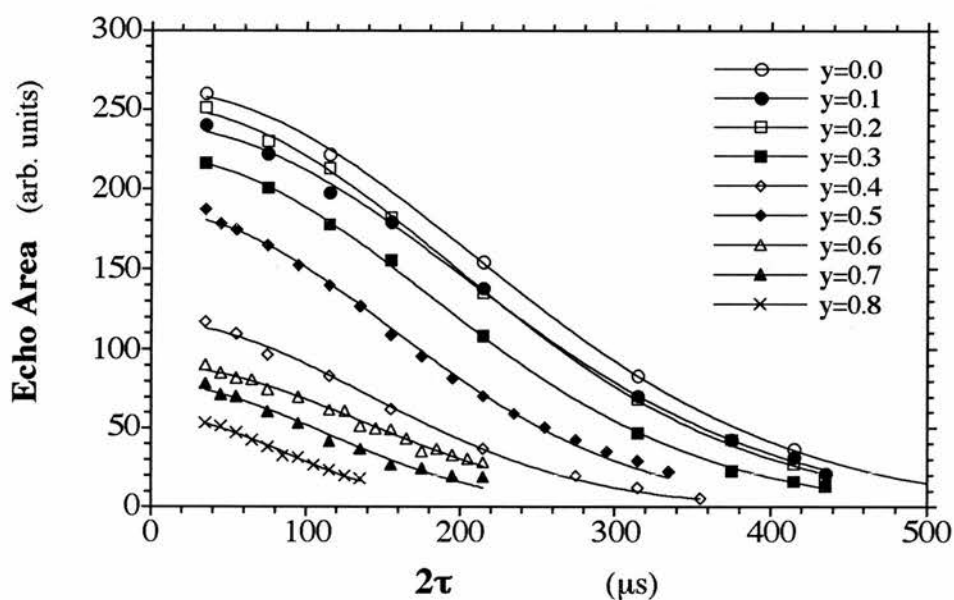


Figure 5.30 Spin-spin relaxation time,  $T_2$  of Pb NMR measurement at RT. The separate points are experimental data and the lines are Gaussian function fitting curves (see text).

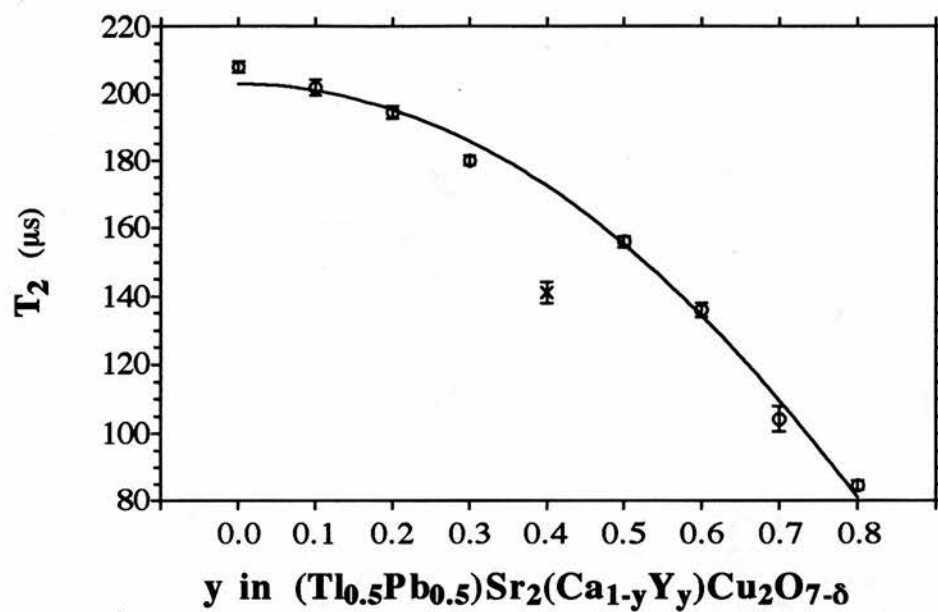


Figure 5.31  $T_2$  of Pb NMR obtained from Figure 5.30 as a function of  $y$ , the yttrium concentration.

## References

- 1 Liu R.S., Edwards P.P., Huang Y.T., Wu S.F., and Wu P.T., *J. Solid State Chem.* **86**, 334 (1990)  
Liu R.S., and Edwards P.P., *Material Science Forum* ed. by Pouch J.J. et al. NASA (1992)  
Liu R.S., *PhD Thesis*, University of Cambridge, UK (1992)
- 2 Liu R.S., private conversation. (1992)
- 3 Lusnikov A., Miller L.L., McCallum R.W., and Mitra S., *J. Appl. Phys.* **65**, 3136 (1989)
- 4 Tunstall D.P., Dai G.P., Webster W.J., Booth H., Arumugam S., Liu R.S., and Edwards P.P., *Supercond. Sci. Technol.* **6**, 33 (1993)
- 5 Webster W.J., *PhD Thesis*, University of St. Andrews, UK (1993)
- 6 Song Y.-Q., Lee M., Halperin W.P., Tonge L.M., and Marks T.J., *Phys. Rev. B* **44**, 914 (1991)
- 7 Hentsch F., Winzek N., Mehring M., Mattausch H., and Simon A., *Physica C* **158** 137 (1989)
- 8 Alloul H., Ohno T., and Mendels P., *Phys. Rev. Lett.* **63** 1700 (1989).
- 9 Balakrishnan G., Dupree R., Farnan I., Paul D. Mc., and Smith W. E., *J. Phys. C: Solid State Phys.* **21** L848 (1988)
- 10 Zhdanov Iu. I., Aleksashin B.A., Mikhalyov K.N., Lavrentjev V.V., Verhovskii S.V., Yakubovskii A.Y., Ozhogin V.I., Shustov L.D., and Myasoedov A.B., *Physica C* **183** 247 (1991).

## Chapter 6

# Data Analysis & Discussion

### § 6.1 Introduction

In last chapter, we have presented all the experimental results which included thallium, yttrium, copper, and lead NMR in the  $(\text{Tl}_{0.5}\text{Pb}_{0.5})\text{Sr}_2(\text{Y}_y\text{Ca}_{1-y})\text{Cu}_2\text{O}_{7-\delta}$  series samples. As can be seen, we have made NMR experiments on as many ions as we can. All the rest of ions ( $\text{Sr}^{2+}$ ,  $\text{Ca}^{2+}$ , and  $\text{O}^{2-}$ ) are only detectable with great difficulty. In this Chapter, we intend to further analyse and discuss these results. Since most of the samples are aligned, it is also necessary to discuss the alignment.

### § 6.2 Alignment

Crystals of all high  $T_c$  superconductors exhibit structures with non-cubic symmetry<sup>1</sup>, and physical properties are highly anisotropic. However, the growth of large single crystals of high  $T_c$  superconductor is difficult. Often the size of available single crystals is too small to be useful for some experiments. In this case the production of polycrystals with identical grain orientation may suffice for some experiments. Alignment of crystalline grains of YBCO was first made by Farrell *et al*<sup>2</sup>. Since then, the method has been widely employed and particularly useful for NMR and NQR experiments.

In this section, we would like to discuss the following questions:

- i) Why can powders be aligned in a magnetic field?
- ii) Why is the Tl-based sample usually more difficult to align than YBCO system?
- iii) Why do X-rays show different degree of alignment from NMR results?

If a crystal possessing anisotropy in its magnetic susceptibility ( $\chi$ ) is placed in a magnetic field  $\mathbf{H}$ , it will tend to rotate to an angle minimising its energy in the field, this occurs when the axis of maximum  $\chi$  is parallel to  $\mathbf{H}$ . For the High- $T_c$  cuprate superconductors, the crystal structures are usually orthorhombic or tetragonal (relation of the lattice constants is  $a \leq b < c$ ), and c-axis is usually the axis of maximum  $\chi$ . For example, in  $\text{YBa}_2\text{Cu}_3\text{O}_{7-\delta}$ , the anisotropy which is defined as,

$$\Delta\chi = \chi_{//} - \chi_{\perp} \quad (6.1)$$

above  $T_c$  (about  $1 \times 10^{-4} \text{ Cm}^3/\text{mol}$ )<sup>3</sup> is positive and is probably due to anisotropy in the Van Vleck paramagnetic susceptibility of the Cu-O layers<sup>4</sup>, where  $\chi_{//}$  and  $\chi_{\perp}$  are the susceptibilities parallel and perpendicular to the c-axis, respectively. When the powder sample is placed in a magnetic field, if the size of the powders is small enough to consider the powder as a single crystal, the powder will rotate until the c-axis is parallel to the magnetic field  $\mathbf{H}$ . Therefore, the powders will be all aligned with their c-axis parallel to each other. After the Stycast is set at room temperature, the powders cannot move any more and keep their aligned orientation.

Under almost exactly the same conditions, the alignment of the Tl-base materials is much worse than one of the YBCO materials<sup>5</sup>. The possible reason is that the anisotropy  $\Delta\chi$  (equation 6.1) of the Tl-base sample is smaller than for YBCO material. Unfortunately, we do not have the data to prove this point yet.

We have noticed that the result of the degree of alignment from X-ray diffraction is different to the result shown in copper NMR, which shows less alignment. To find out

the reason, we took the samples to be investigated by electron microscope. We found that although the size of the powders is very small (less  $5\mu\text{m}$ ), after mixing with Stycast some of the powders are clustered into big particles so that sizes of some of the particles are great than  $100\mu\text{m}$ . X-ray sensitivity is limited to the surface of the sample, NMR characterization is uniformly sensitive to all the crystallites throughout.<sup>6</sup> This will lead to some unaligned fraction inside of the big clustered particles being not detected by X-rays, but detected by the NMR experiment. Therefore, the X-ray spectra show better alignment.

### § 6.3 Thallium NMR

Since thallium has spin  $I = 1/2$ , *i.e.* any quadrupolar interactions which could mask features like the Knight shift are absent, thallium NMR has been of interest to many groups throughout the world. Most thallium NMR has been performed on two types of high- $T_c$  superconductors, namely in the  $\text{TlBa}_2\text{Ca}_{n-1}\text{Cu}_n\text{O}_{2n+3+\delta}$  superconductors with one TlO-layer<sup>*e.g.* 7</sup> or in the  $\text{Tl}_2\text{Ba}_2\text{Ca}_{n-1}\text{Cu}_n\text{O}_{2n+4+\delta}$  system with two TlO-layers<sup>*e.g.* 6,8,9,10,11,12</sup>.

In general, information can be obtained from thallium NMR as follows: (i) the London penetration depth can be directly obtained from a fit of the theoretical lineshape to the NMR spectrum<sup>6,8(a)</sup>; (ii) if the thallium site is in the Ca-layers, it can be detected by thallium NMR (a defect line may be obtained)<sup>8(c,d)</sup>; (iii) studying the temperature dependence of the thallium Knight shift and relaxation time,  $T_1(1)$  (in the normal site), shows strong antiferromagnetic correlations similar to Cu(2) in YBCO materials, indicating a spin gap. The  $T_1(2)$  (defect line) behaves like  $^{89}\text{Y}$  in YBCO superconductors<sup>8(e)</sup>.

What sort of information can be obtained from our thallium NMR results? Since we did not measure any temperature variation spectra nor in the normal state (above  $T_c$ ), we cannot draw any conclusions needing temperature dependence. However, since our Tl NMR was performed at 1.5 K, far below  $T_c$ , we can obtain information on the penetration of flux from the line shape (see § 2.6). From *equation 2.26* pointed by Pincus *et.al.*<sup>13</sup>, we can rewrite the penetration depth  $\lambda$  as a function of the second moment of the field distribution  $(\overline{\Delta h^2})^{1/2}$ ,

$$\lambda \approx \left[ \frac{\varphi_0}{(\overline{\Delta h^2})^{1/2} \sqrt{16\pi^3}} \right]^{1/2} \quad (6.2)$$

where  $\varphi_0 = hc/2e = 2.068 \times 10^{-15}$  Tesla  $\cdot$  m<sup>2</sup> is the quantum of flux. Table 6.1 shows the results of the second moment,  $(\overline{\Delta h^2})^{1/2}$ , derived from Tl NMR spectra, and the penetration depth calculated from *equation 6.2*.

**Table 6.1.** the results of the second moment,  $(\overline{\Delta h^2})^{1/2}$ , derived from Tl NMR spectra, and the penetration depth,  $\lambda$ .

samples	$(\overline{\Delta h^2})^{1/2}$ (Tesla)	$\lambda$ (Å)
TAY0	0.013±0.005	780±150
TAY1	0.011±0.005	870±200
TAY2	0.014±0.005	760±140
TAY3	0.013±0.005	780±150

As seen from the table, in the experimental error range, the penetration depth is roughly constant as  $y$ , the yttrium concentration changes. The values of the penetration depth are somewhat smaller than those measured by M. Mehring *et.al.*<sup>8(a)</sup> on  $Tl_2Ba_2CuO_6$  at 4.26 Tesla and 20 K (1700Å).

Since the spectra are very broad (see Figure 5.8), we could not obtain an accurate shift. Under the experimental error, the shift are more or less a constant as  $y$ , the yttrium concentration varies. This is possibly true, because the Knight shift may tend to zero at such low temperature (4.2 K), only orbital shift remaining, which may be the same for the different compounds in this system.

According to the site occupancy refinements from the neutron diffraction data, there are maybe about 10% Tl(Pb) occupancy of Cu/Y sites (see §4,3). The exist of thallium occupancy on yttrium site can lead to an extra line (see reference (8.b & c)). However, we did not observe such an extra line. The reason might be that our experiment is not sensitive enough to detect such a weak and broad signal. Also since the main line is very broad, the defect line must be under the main line region, so that it is difficult to distinguish the weak defect line from the main line (if there is any defect line, the intensity of the line is only about or less 10% of the main line. Our experimental error may be about 10%).

## § 6.4 Yttrium NMR

The yttrium nucleus as an NMR probe for the study of High- $T_c$  cuprate superconductors has both strong advantages and disadvantages. One advantage is that Y is a spin-half nucleus (like thallium), and thus has no electric quadrupole moment. The other is that  $^{89}Y$  isotope is 100% abundant. There are two primary disadvantages of the Y nucleus. First,  $^{89}Y$  has a small gyromagnetic ratio, giving a resonance frequency of only about 24 MHz in a 11.75 Tesla field, quite small as compared to  $^{63}Cu$  (130 MHz)

and  $^{207}\text{Pb}$  (104 MHz). (The relative NMR sensitivity and signal-to-noise at a fixed magnetic field varies with the gyromagnetic ratio raised to approximately the third power.) The second disadvantage is that Y, nestled between adjacent  $\text{CuO}_2$  planes (see the structure shown in Chapter 1 Figure 1.5 and Chapter 4 Figure 4.2), is generally thought to be an element of less importance to superconductivity, since one may replace Y by rare earth metals without substantially changing  $T_c$ <sup>14</sup>. However, we shall see that Y NMR has provided quite interesting results and indirect information about the  $\text{CuO}_2$  planes.

In § 5.4, we have presented the yttrium NMR results. Since a lot of yttrium NMR measurements have been performed on the well-known compound YBCO, to obtain useful information from the results, we compare our results with those of Webster<sup>15</sup> and Alloul *et. al*<sup>16</sup>.

Comparing Figures 5.10 and 5.11, clearly, not only the resonance line position is at a different place *i.e.* the shift is different, but the line width is also very different. (These two experiments were made under some conditions). To make our results comparable with those of Alloul *et. al.* on YBCO system, the isotropic shifts of  $^{89}\text{Y}$  NMR at room temperature have been computed using *equation (2.23a)*

$$K_{iso} = \frac{1}{3}(K_{//} + 2K_{\perp}) \quad (6.3)$$

where  $K_{//}$  and  $K_{\perp}$  are the magnetic shifts obtained when c-axis parallel and perpendicular to  $\mathbf{B}$ , the applied magnetic field, respectively. In Figure 6.1a we plot the isotropic shifts of the thallium system as a function of y, the yttrium concentration. Figure 6.1b shows the yttrium NMR shifts at room temperature of the YBCO system adapted from ref. 16 (a). The shifts in both Figures 6.1a & 6.1b have been subtracted from 200 PPM, the true origin of the shift relative to a one molar solution of  $\text{YCl}_3$  see § 5.4.

One may ask why the line width of the yttrium the Tl-1212 system is broader than those of the YBCO system (the half-intensity widths of the Tl-1212 system are about 2 KHz, those of the YBCO are about 1.2 KHz in the metallic region), while the Knight shifts of the Tl system (in a range of -120 to -160 ppm) is smaller than those of YBCO system (in a range of -180 to -300 ppm)?

To answer these questions, we carefully compared crystal structure of these two systems shown in Chapter 2. We found that the distance between yttrium and oxygen, which lies on Cu-O plane, is larger in thallium system than in YBCO; conversely, the distance between yttrium and Cu-O plane is smaller in thallium system than in YBCO. The yttrium is closer to the oxygen site in YBCO, which may lead to larger yttrium Knight shifts, because yttrium couples with oxygen more strongly. Because there is an anti-ferromagnetic correlation in Cu-O plane, the result of yttrium being nearer to Cu-O plane in thallium materials may cause a broad line width.

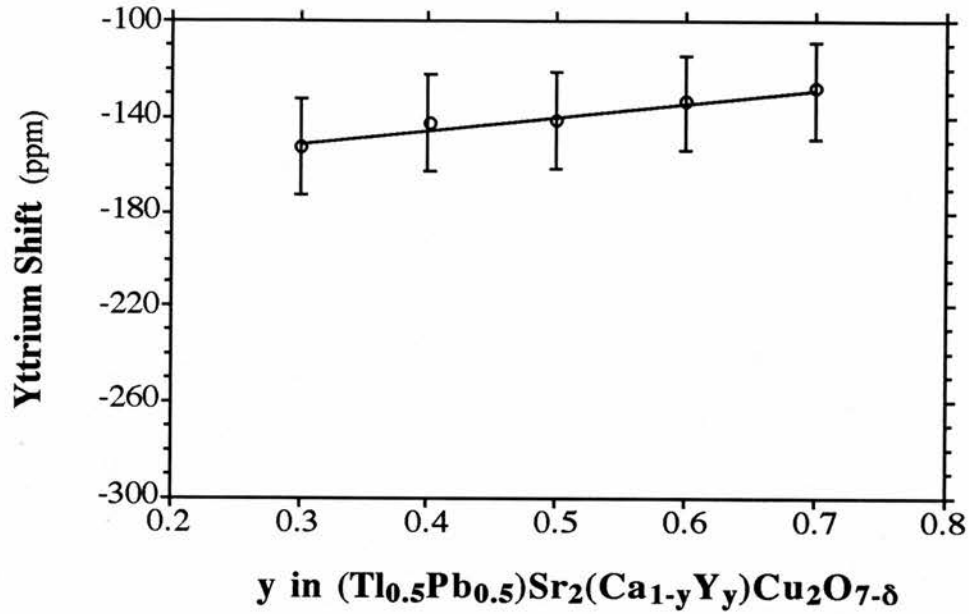


Figure 6.1(a) *Isotropic Knight shifts as a function of y, the yttrium concentration in the  $(Tl_{0.5}Pb_{0.5})Sr_2(Y_yCa_{1-y})Cu_2O_{7-\delta}$  system.*

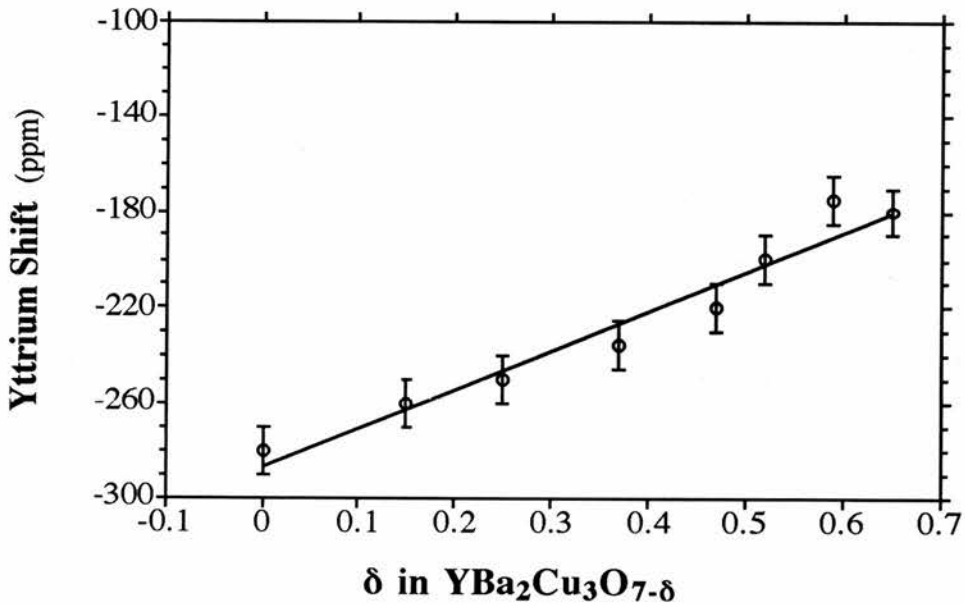


Figure 6.1(b) *Isotropic Knight shifts as a function of  $\delta$ , the oxygen stoichiometry in the  $YBa_2Cu_3O_{7-\delta}$  system adapted from ref. 16 (a).*

## § 6.5 Analysis of The Copper NMR Results

### § 6.5.1 Theoretical Curve Fitting

Copper NMR results have been presented in § 5.5. To obtain further information about copper NMR from these results, one needs to analyse the data using a theory. Before to do so, we should work out the resonance frequency for each spectrum. Since the spectra are broad, to obtain better precision, we differentiated the spectra as was done on copper NQR see § 5.5.4 and Figure 5.25. In Figure 6.2, we plot the resonance frequency, for the sample NCAY0, obtained from Figure 5.15 as a function of the angle  $\Theta$ , between the marked line on the sample and the direction of applied magnetic field (the open circles are experimental data).

If we consider that the copper nuclear system only has Zeeman, Knight shift and quadrupole interactions, and since this Tl-1212 system is tetragonal in structure (*i.e.*  $\eta = 0$ ), in this case, the angle function of resonance frequency should fit the equation (2.25), which we rewrite as:

$$\nu = \nu_0 [1 + a(3\mu^2 - 1) + \frac{b}{\nu_0^2}(1 - \mu^2)(1 - 9\mu^2)] \quad (6.4)$$

where  $\mu = \cos \theta = \cos (\Theta - \theta')$ ,  $\theta$  is the angle between c-axis and  $\mathbf{B}$ ,  $\Theta$  is the angle between  $\mathbf{B}$  and the marked line (which was a line marked on the sample thought as the c-axis),  $\theta'$  is the angle between the marked line and c-axis.

We use the computer to fit the experimental data to extract the parameters  $\nu_0$ ,  $a$ ,  $b$  and  $\theta'$ , and the best fitting curves are shown in Figure 6.2 (the solid line). A similar procedure was made on the other samples in the NCAY\* series shown in Figures 6.3 to 6.9, respectively. As one can see from these figures, all the fitting curves fit excellently

the experimental data, with the correlation coefficients in the range of 0.99 ~ 0.999. In Table 6.3, we list these fitting parameters. One should mention here that we could not detect a copper spin echo signal on the samples NCAY9 and NCAY10. The signal to noise ratio was very poor for the NCAY8 sample, so we did not do the orientation spectrum of NCAY8. Although we have presented the error bar for each data set, since these errors only reflect the computer fitting error. Actually each resonance frequency has its own error see Figures 6.2 - 6.9. In particular, for NCAY6 and NCAY7, since the signals are very broad and weak see in Figures 5.21 and 5.22, the errors of the resonance frequencies may be quite large, which will lead to even larger errors for the fitting parameters. We will discuss mainly the  $y=0$  to 0.5 samples (the metallic range of the system).

**Table 6.3** A list of fitting parameters.

sample	$\nu_0$ (MHz)	$a$ ( $\times 1000$ )	$b$ (MHz) <sup>2</sup>	$\theta'$ (Degrees)
NCAY0	133.82 $\pm$ 0.03	2.10 $\pm$ 0.24	82.0 $\pm$ 4.5	-6.1 $\pm$ 0.8
NCAY1	133.79 $\pm$ 0.03	2.17 $\pm$ 0.28	76.25 $\pm$ 4.9	-5.8 $\pm$ 1.3
NCAY2	133.65 $\pm$ 0.02	2.23 $\pm$ 0.14	69.55 $\pm$ 2.1	-6.7 $\pm$ 0.8
NCAY3	133.59 $\pm$ 0.04	2.14 $\pm$ 0.26	63.05 $\pm$ 5.1	1.9 $\pm$ 1.6
NCAY4	133.51 $\pm$ 0.03	2.26 $\pm$ 0.15	58.40 $\pm$ 3.7	1.8 $\pm$ 1.4
NCAY5	133.44 $\pm$ 0.02	2.27 $\pm$ 0.12	59.01 $\pm$ 2.2	-0.3 $\pm$ 0.9
NCAY6	133.44 $\pm$ 0.05	2.18 $\pm$ 0.46	61.48 $\pm$ 7.3	-4.7 $\pm$ 2.5
NCAY7	133.48 $\pm$ 0.03	2.59 $\pm$ 0.23	66.45 $\pm$ 4.1	-2.3 $\pm$ 1.4
YBCO	133.65 $\pm$ 0.02	2.37 $\pm$ 0.14	179.8 $\pm$ 3.0	-8.7 $\pm$ 0.4

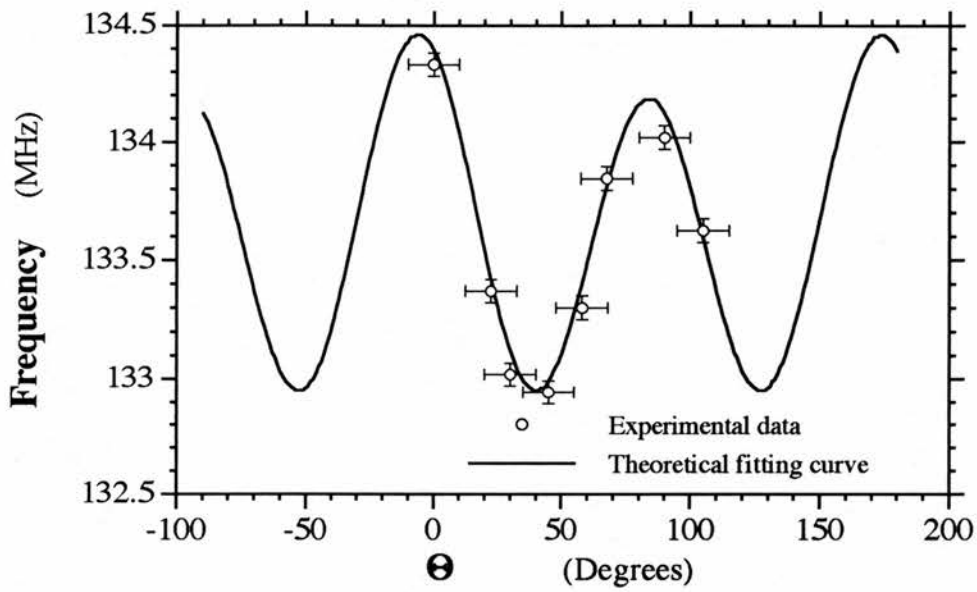


Figure 6.2 *Copper nuclear resonance frequency as a function of the angle,  $\Theta$ . The open circles are experimental data. The solid line is theoretical fitting curve using equation (6.4). The sample is NCAY0.*

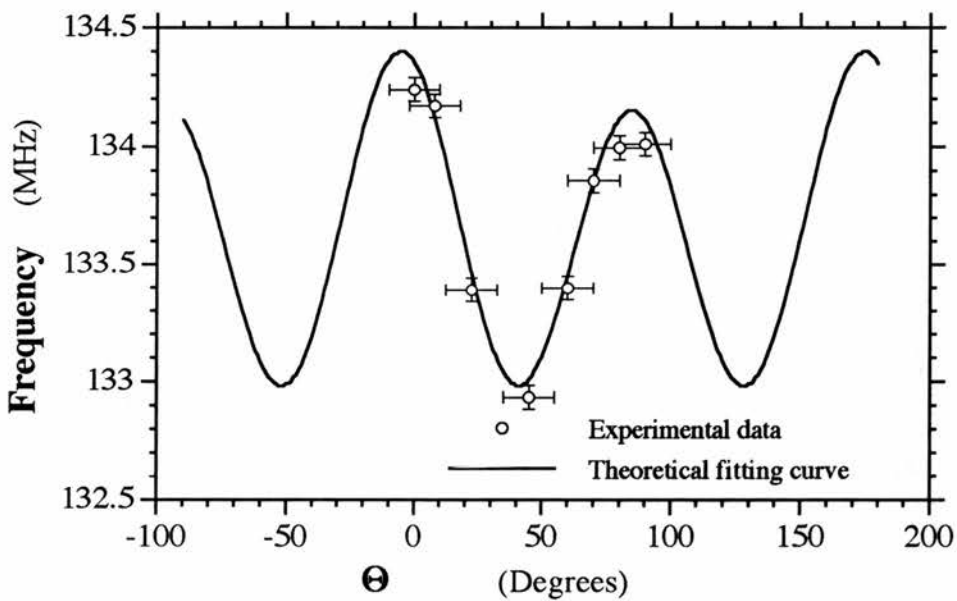


Figure 6.3 *As Figure (6.2). The sample is NCAY1.*

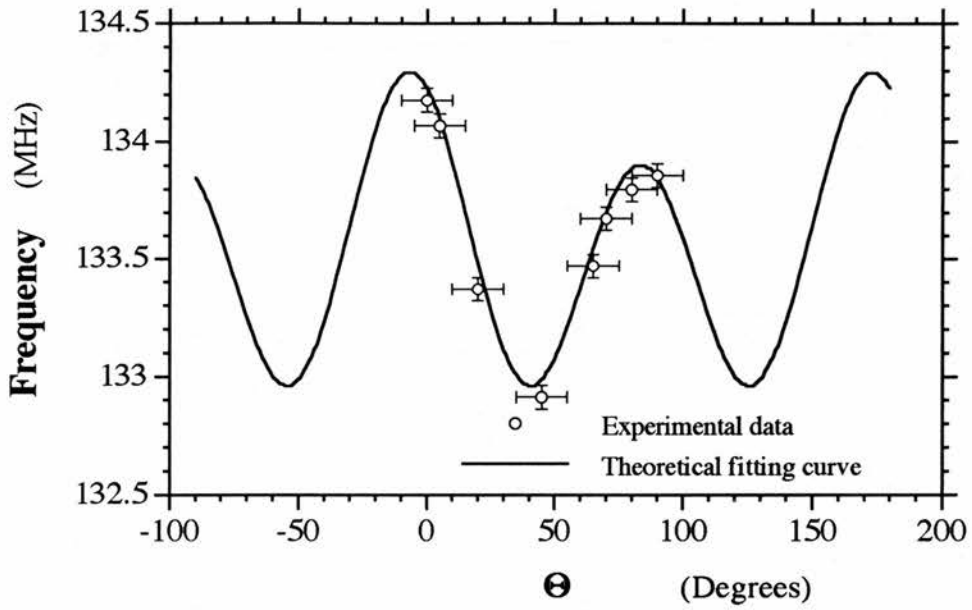


Figure 6.4 As Figure (6.2).The sample is NCAY2.

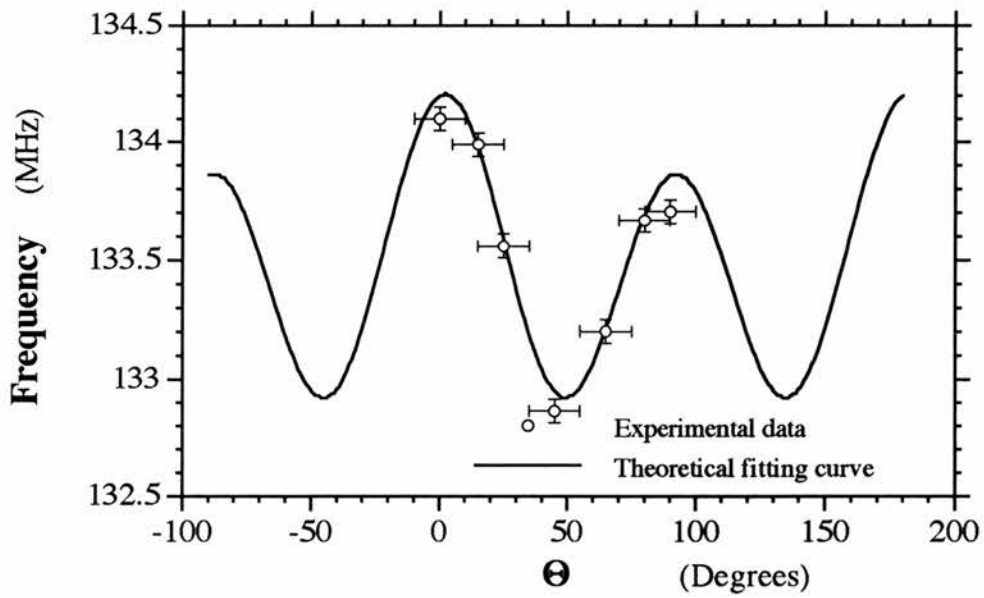


Figure 6.5 As Figure (6.2).The sample is NCAY3.

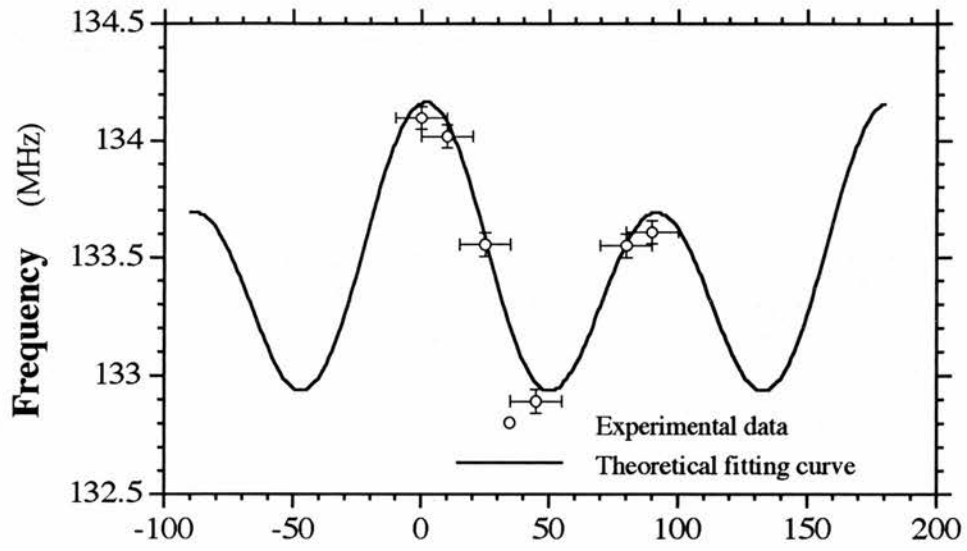


Figure 6.6 As Figure (6.2).The sample is NCAY4.

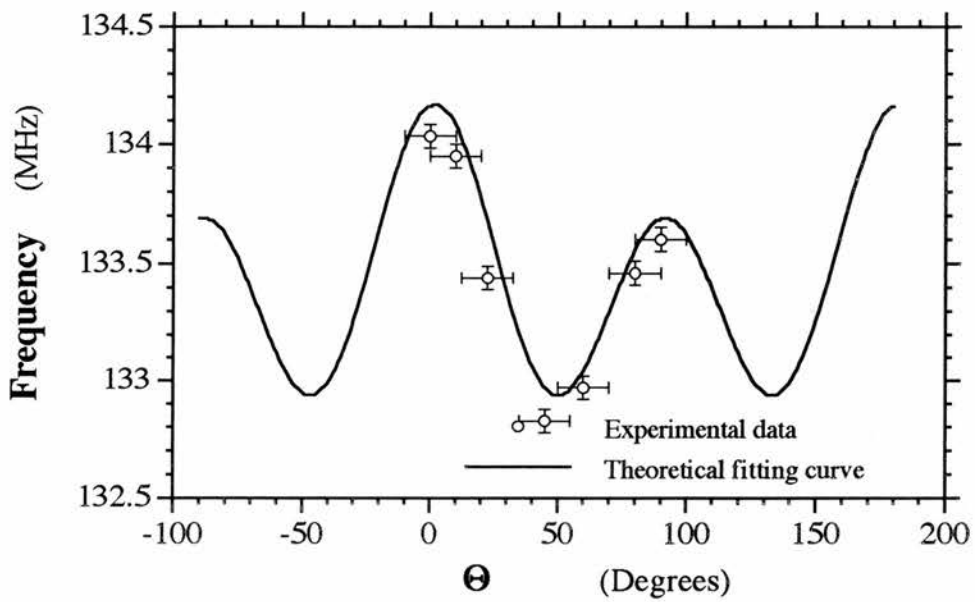


Figure 6.7 As Figure (6.2).The sample is NCAY5.

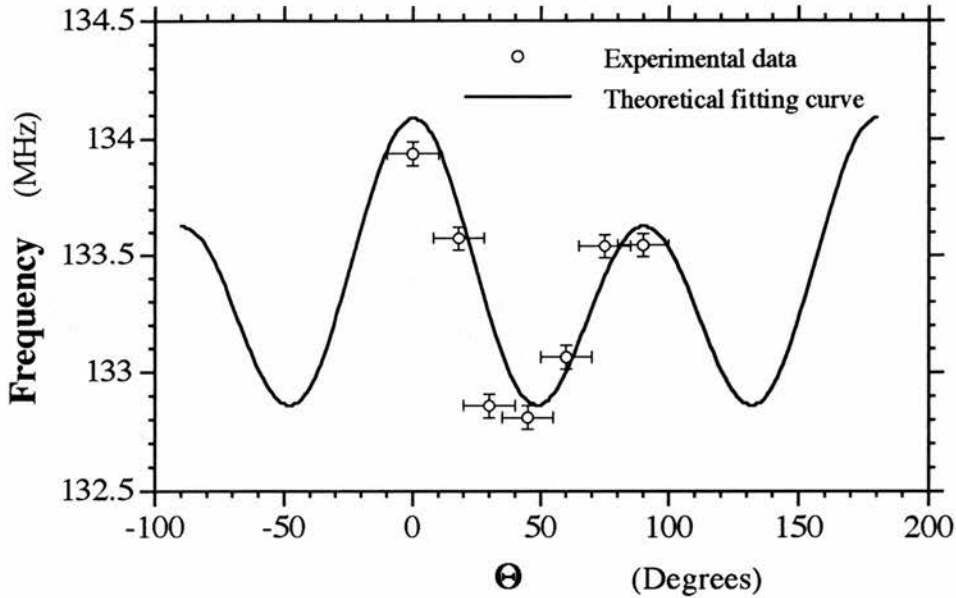


Figure 6.8 As Figure (6.2).The sample is NCAY6.

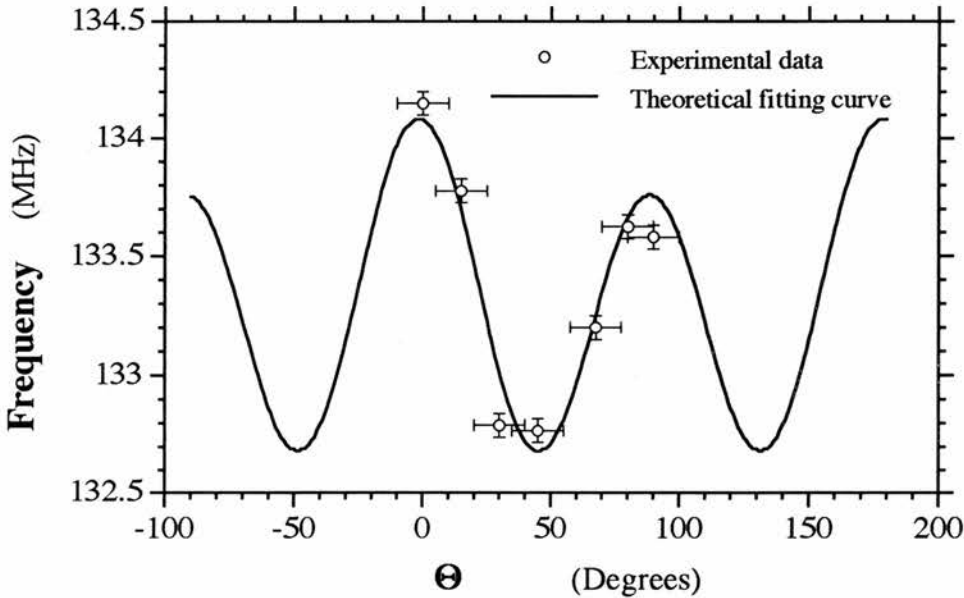


Figure 6.9 As Figure (6.2).The sample is NCAY7.

### § 6.5.2 Knight Shift Components

From equations (2.23a), (2.23b), and (2.25a), we have:

i) the isotropic Knight shift,  $K_{iso}$ :

$$K_{iso} = \frac{\nu_0 - \nu_{ref}}{\nu_{ref}} \quad (6.5)$$

where  $\nu_{ref} = 132.569$  MHz.

ii) the axial Knight shift,  $K_{ax}$ :

$$K_{ax} = a(1 + K_{iso}) \quad (6.6)$$

iii) the c-axis parallel to **B** Knight shift,  $K_{//}$ :

$$K_{//} = K_{iso} + 2K_{ax} \quad (6.7)$$

iv) the c-axis perpendicular to **B** Knight shift,  $K_{\perp}$ :

$$K_{\perp} = K_{iso} - K_{ax} \quad (6.8)$$

Using these equations and the parameters given in Table 6.3, we are able to calculate out the Knight shift components,  $K_{iso}$ ,  $K_{ax}$ ,  $K_{//}$  and  $K_{\perp}$ . They are plotted as a function of  $y$ , the yttrium concentration, in Figures 6.10, 6.11, and 6.12, respectively.

If we follow Mila and Rice's discussion<sup>17</sup>, the magnetic shift should be separated into a spin part and an orbital part. The total Knight shift  $K_{tot}^{\alpha}$  can be written as:

$$K_{tot}^{\alpha} = K_{orb}^{\alpha} + K_s^{\alpha} \quad (6.9)$$

where  $\alpha = a, b, c$  is the direction of the field. In terms of the susceptibilities, we have:

$$K_{tot}^{\alpha} = (\gamma_e \gamma_n \hbar^2)^{-1} \left[ A_{orb} \chi_{orb}^{\alpha} + (A_s^{\alpha} + 4B) \chi_s \right] \quad (6.10)$$

where  $\gamma_e$  and  $\gamma_n$  are the electron and nuclear gyromagnetic ratios, respectively,  $\chi_{orb}^{\alpha}$  and  $\chi_s$  are the orbital and spin susceptibilities, respectively,  $A_{orb}$  and  $A_s^{\alpha}$  are the nuclear-orbital coupling constant and nuclear-electron spin coupling constant, B is the transferred hyperfine coupling constant and the factor 4 is because each Cu has 4 nearest copper neighbours. The nuclear-electron spin coupling constant  $A_s^{\alpha}$  includes the contact ( $A_c$ ), core polarization ( $A_{cp}$ ), dipolar ( $A_{dip}^{\alpha}$ ), and spin-orbit ( $A_{so}^{\alpha}$ ) contributions. [Here if any term has a superscript  $\alpha$ , that means this term is anisotropic, conversely, others are isotropic.]

First, we try to work out which part of the shift is changing as calcium is being substituted by yttrium. The axial shift stays stable as yttrium concentration changes, as shown in Figure 6.11. Importantly, this indicates that the substitution of calcium by yttrium only varies the *isotropic part* of the total magnetic shift shown in Figure 6.10. The very simplest interpretation of the trends in Figures 6.10 and 6.11 would be that only the isotropic term,  $4B\chi_s$ , of *equation (6.10)* is controlling the variation of  $K_{iso}$  (Figure 6.10), and that, further, the absence of variation of  $K_{ax}$  (Figure 6.11) implies that  $\chi_s$  is constant over the composition range (since  $A_s^{\alpha}$  is anisotropic). This deduction places the origin of the  $K_{iso}$  variation then as a variation of B, the transferred hyperfine interaction. Figure 6.13 is an attempt to provide further support to this idea; in this graph the correlation between isotropic shift and copper-copper distance on the  $\text{CuO}_2$  plane (on which B should depend) is explored, with  $y$  as an implicit parameter. [A note of caution is necessary here; the move from  $y = 0.0$  to  $y = 0.5$  clearly takes the septenary superconductor from over-doped, through optimal doping at  $y = 0.2$ , to under doped, and this should have implications for the magnitude of  $\chi_s$  (the above analysis has deduced that  $\chi_s$  remains constant).]

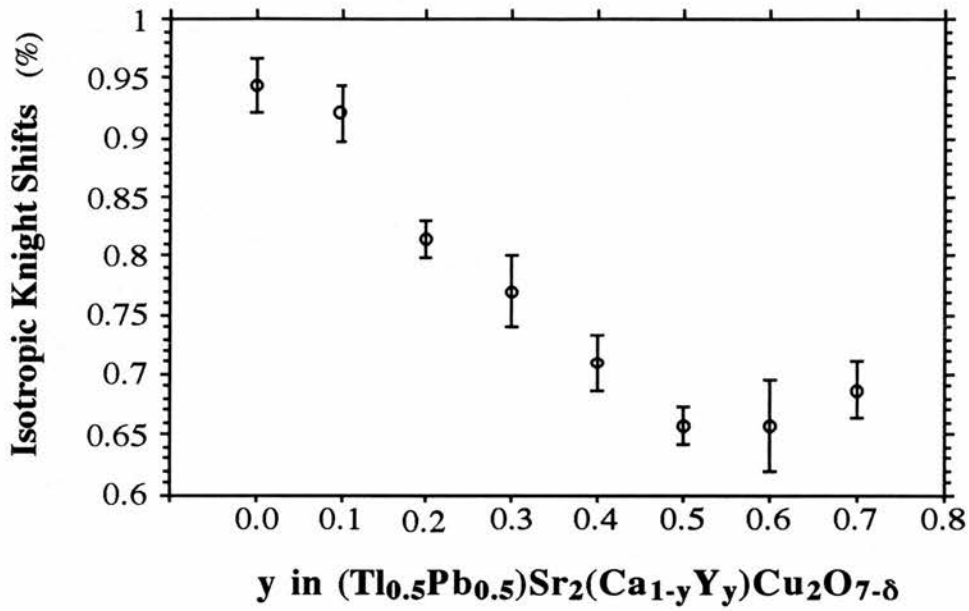


Figure 6.10 The isotropic Knight shift component as a function of  $y$ , the yttrium concentration in  $(Tl_{0.5}Pb_{0.5})Sr_2(Ca_{1-y}Y_y)Cu_2O_{7-\delta}$  system.

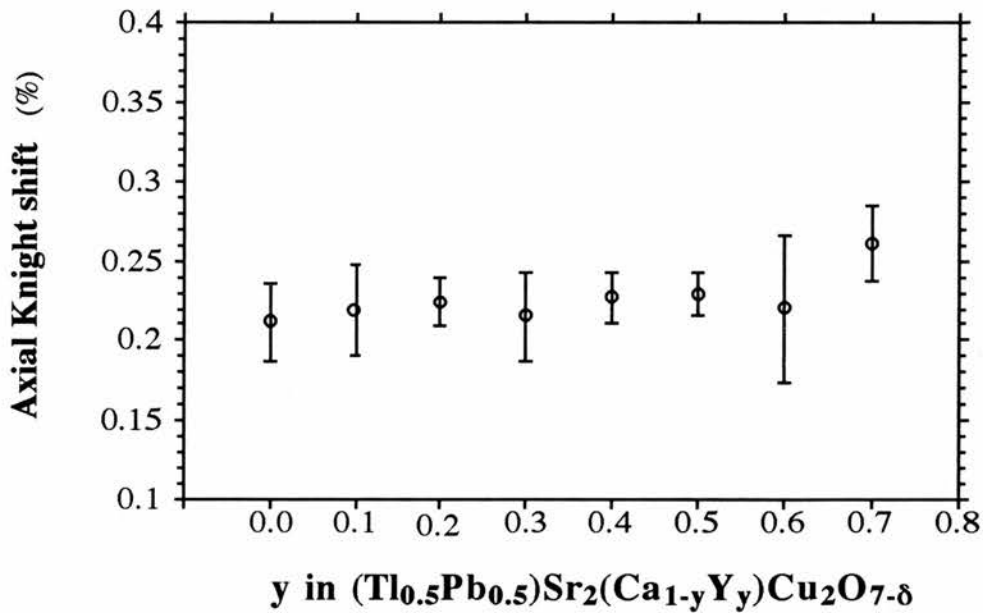


Figure 6.11 The axial Knight shift component as a function of  $y$ , the yttrium concentration in  $(Tl_{0.5}Pb_{0.5})Sr_2(Ca_{1-y}Y_y)Cu_2O_{7-\delta}$  system.

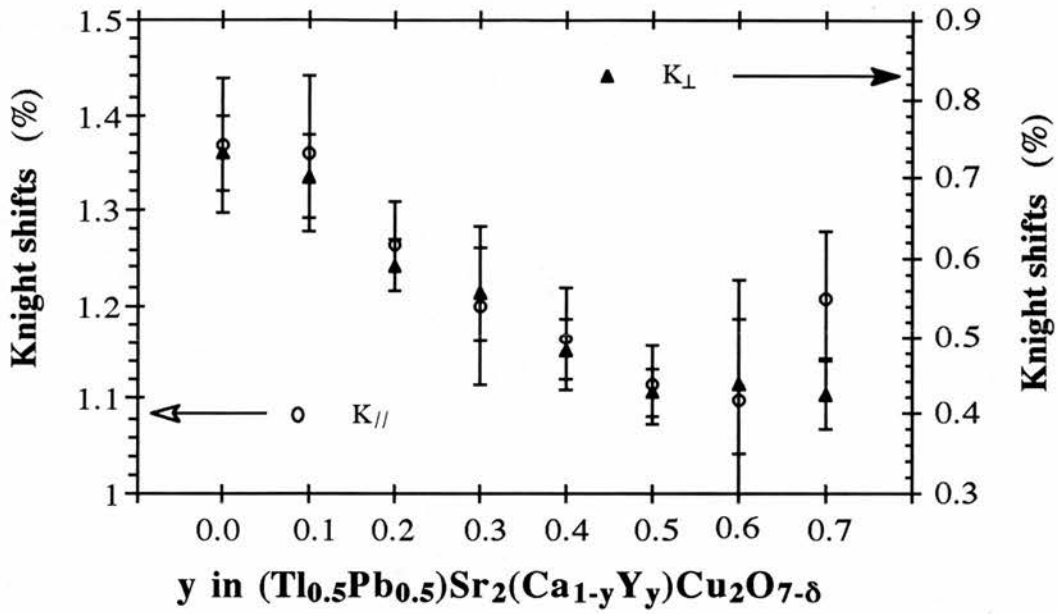


Figure 6.12 The Knight shift components ( $K_{||}$  &  $K_{\perp}$ ) as a function of  $y$ , the yttrium concentration in  $(Tl_{0.5}Pb_{0.5})Sr_2(Ca_{1-y}Y_y)Cu_2O_{7-\delta}$  system.

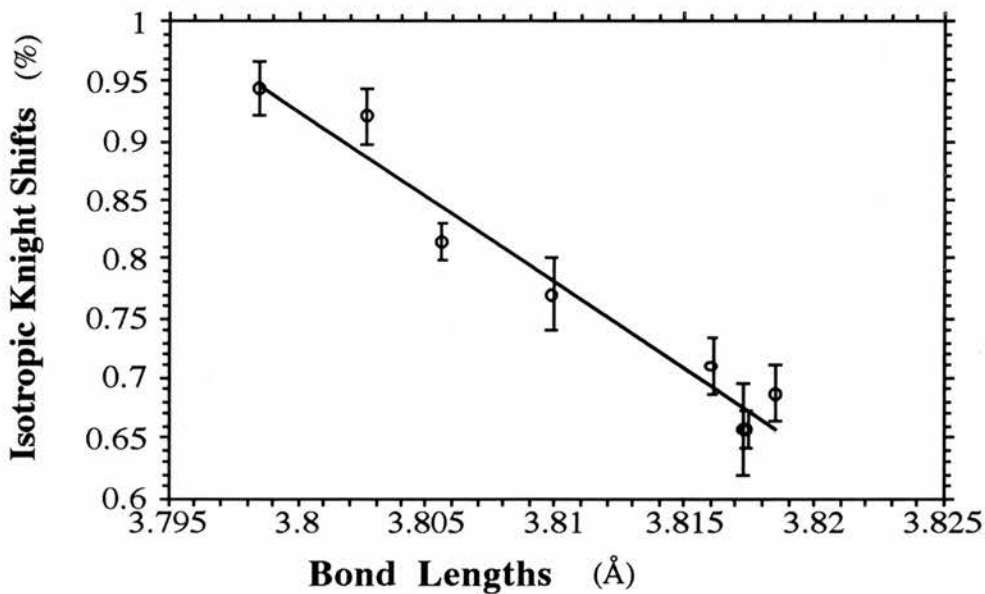


Figure 6.13 The isotropic Knight shift component as a function of  $a$ , the lattice constant in  $(Tl_{0.5}Pb_{0.5})Sr_2(Ca_{1-y}Y_y)Cu_2O_{7-\delta}$  system.

### § 6.5.3 Quadrupole Coupling Constant

As seen from Figure 5.25, we have performed copper NQR on  $y=0.0$  sample. Unfortunately, the NQR signal is too weak to measure on the others. From the NMR experiments, clearly, there are electric quadrupole interactions in the other samples as well as the one of  $y=0.0$ . Fortunately, we can calculate out the quadrupole resonance frequency  $\nu_Q$  from the parameter  $b$  given in Table 6.3. Modifying equation (2.25), we have:

$$\nu_Q = \sqrt{\frac{16b}{3}} \quad (6.11)$$

The quadrupole constant (Figure 6.14) depends upon the crystal physical structure and the charge distribution of the respective compound. Yu *et. al.*<sup>18</sup>, using the FLAPW method, have indicated the extraordinary sensitivity of quadrupole interactions to minor repopulations of admixed states; the theory is not yet sufficiently quantitative to discuss the origins of our observed trends.

### § 6.5.4 Checking the Deconvolution Method on $\text{YBa}_2\text{Cu}_3\text{O}_{7-\delta}$

As a check, we repeated the same experiment under the same conditions on  $\text{YBa}_2\text{Cu}_3\text{O}_{7-\delta}$  ( $\delta$  is near to 0). Figure 6.15 shows the orientation dependent spectra. Because of the good alignment of the YBCO sample, we did not need to subtract the random fraction as did on the Tl-1212 system. In Figure 6.16, we plotted the resonance frequency as a function of the angle  $\Theta$ , and the solid line is the theoretical fitting curve using equation (6.4). The fitting parameters have been presented in Table 6.3. We obtained a quadrupole resonance frequency of 31.0 MHz from the copper NMR experiments, which is in very good agreement with the experimental measurement

(copper NQR) of 31.2 MHz at room temperature. The Knight shift components are also in good agreement with the data obtained by Takigawa et al.<sup>19</sup>, Brinkmann<sup>20</sup> and Webster<sup>15</sup> (see Table 6.4).

**Table 6.4.** By our method we obtained the Knight shift on  $YBa_2Cu_3O_{7-\delta}$ . This table shows a comparison between our results and Takigawa et al.<sup>19</sup> and Brinkmann<sup>20</sup> and Webster<sup>15</sup>. All shift values are in units of percent.

	Our results	Takigawa et al's	Brinkmann	Webster
$K_{\perp}$	$0.576 \pm 0.03$	$0.607 \pm 0.01$	$0.5 \pm 0.2$	$0.5 \pm 0.04$
$K_{//}$	$1.293 \pm 0.045$	$1.269 \pm 0.005$	$1.2 \pm 0.4$	$1.24 \pm 0.03$

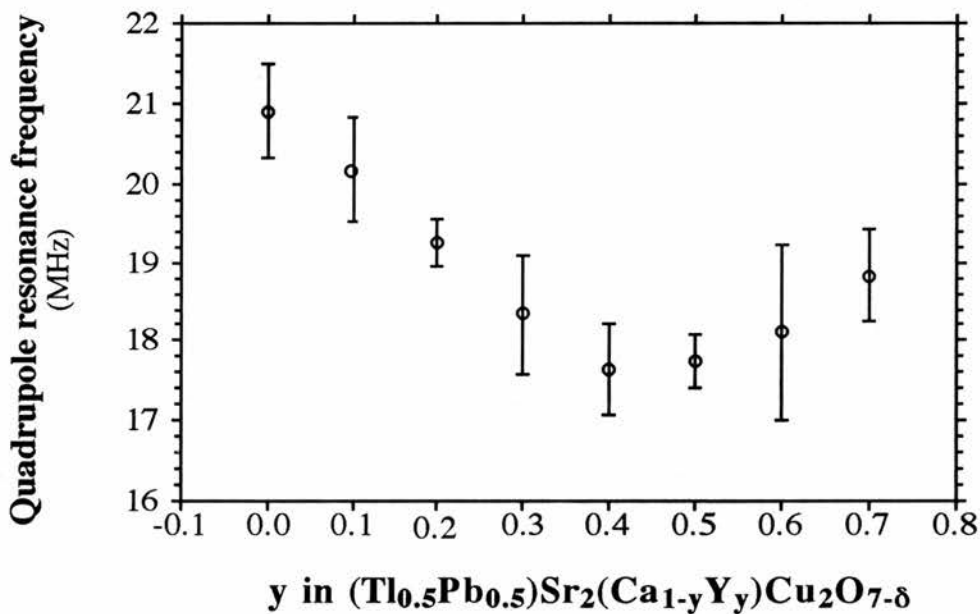


Figure 6.14 Copper-63 quadrupole resonance frequency (calculated from NMR data) as a function of  $y$ , the yttrium concentration.

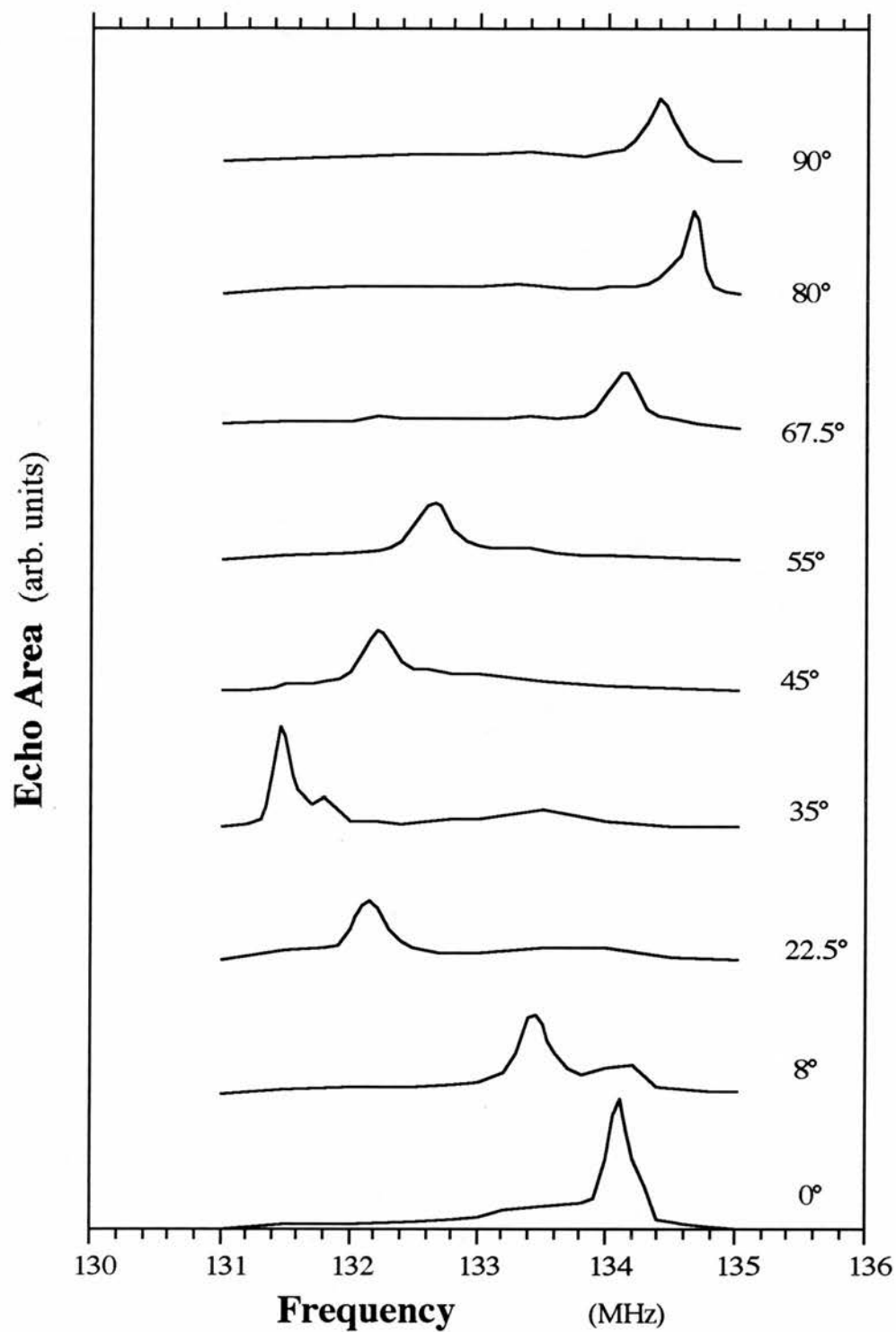


Figure 6.15 *Copper-63 NMR spectra on the aligned sample of  $\text{YBa}_2\text{Cu}_3\text{O}_{7-\delta}$  ( $\delta \sim 0.05$ ) which shows a clear orientation dependence.*

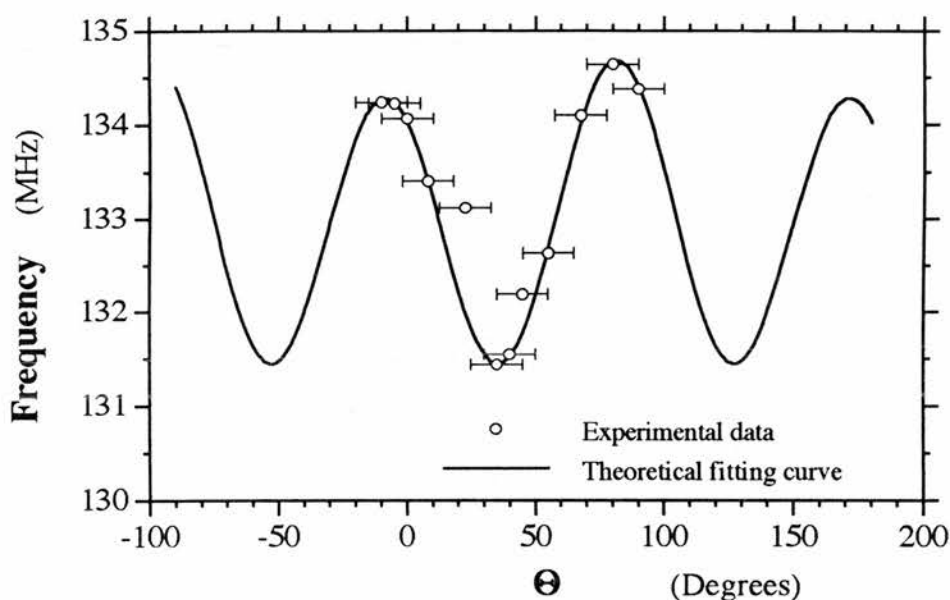


Figure 6.16 The resonance frequency as a function of  $\Theta$ , between the marked line on the sample and the direction of the applied magnetic field, on the aligned sample of YBCO.

### § 6.5.5 A Comparison Between Tl-1212 System and YBCO System

If we compare the copper NMR and NQR results between the Tl-1212 system and YBCO, we note that the Knight shifts for the two system are in the same range while the quadrupole resonance frequencies are significantly different, being around 21 MHz for Tl-samples and about 31 MHz for YBCO. Comparing the two systems, the hole concentration on the Cu-O plane is different between the two system, about one hole per unit cell for YBCO, less than half a hole per unit cell for the Tl system. Yu *et. al.*<sup>18</sup> have shown via the theoretical calculation of quadrupole interactions by the FLAPW method that very small redistributions of electron populations around 'semi-core' copper states can have a dramatic influence. Therefore, the differences of the hole concentration on

CuO<sub>2</sub> plane of course will lead to a redistribution of electron populations around 'semi-core' copper states which cause the difference of the quadrupole constant.

The copper NMR linewidth is about three times broader, and the NQR linewidth is almost 10 times broader, in the Tl system than in YBCO (see Table 6.5). Again we speculate with two possible reasons: (i) structural disorder might be the first reason which cause the spectra broaden. (ii) the smaller hole concentration might lead to stronger antiferromagnetic correlation which also can cause the spectra to broaden. A strong magnetic field would suppress both of these effects, so that the NMR spectra would be expected to be less broad than the NQR spectra.

*Table 6.5. The copper linewidths of NMR and NQR on  $(Tl_{0.5}Pb_{0.5})Sr_2(Ca_{1-y}Y_y)Cu_2O_{7-\delta}$  are compared with which on  $YBa_2Cu_3O_{7-\delta}$ . All the values of the linewidths are in units of KHz.*

	$(Tl_{0.5}Pb_{0.5})Sr_2(Ca_{1-y}Y_y)Cu_2O_{7-\delta}$ y = 0.0	$YBa_2Cu_3O_{7-\delta}$
NMR‡	350 ± 50	120 ± 20
NQR	3200 ± 200	340 ± 50

‡ The data was taken on the spectra for c parallel to **B**

### § 6.5.6 Conclusions

We have established a trend in the variation of the quadrupole coupling constant and the copper Knight shift components across the compositional range of our thallium-based cuprate superconductor. We have also discussed possible reasons for the trends. We highlight the following points.

- (i) We have established a method for deconvoluting overlapping spectra from partially aligned samples.
- (ii) We measure a constant axial component of Knight shift across the compositional range.
- (iii) We measure a decreasing isotropic component of Knight shift across the compositional range. This may be caused by the transferred hyperfine coupling getting weaker as yttrium replaces calcium, correlating with the trends in Cu-O distance revealed by neutron diffraction.
- (iv) The quadrupole coupling constants of the Tl samples are only about two thirds of those in YBCO, which may be correlated with the hole concentration.
- (v) Both NMR and NQR spectra are broader in comparison with YBCO sample. This might be caused by the stronger antiferromagnetic correlation or the structural disorder in the thallium system.

## § 6.6 Lead Knight Shifts

What is the valence state of lead in this system? Has it valence II or IV or both? Initially, from the phase diagram (Figure 4.1), it seems that lead should have the IV valence state, since when Pb replaces Tl, the behaviour is that of electrons being doped in [since along the x-axis just like along the y-axis (see Figure 4.1) the system moves from an over-doped state to an under-doped state through the optimum]. However thallium has two valence states *i.e.* 1+ and 3+. Therefore, if thallium was in a 1+ state, lead could be in 2+ state. However, if this was the case, the copper would have a valence state of over 3+ (if you keep both Sr and Ca at 2+ as they are should be). This case cannot be right. So, lead must be in the 4+ state.

According to a reference book by Brevard and Granger<sup>21</sup>, the shift for Pb (IV) is about +0.5% and for Pb (II) is in the range from -0.6% to +0.32%. From our NMR experimental results (Figure 5.28), the shifts of lead in this system are varying from +0.28% to +0.13% as the yttrium concentration changes. It seems that the shifts were in the range of Pb (II) not Pb (IV) shift. Therefore, the lead in this system might be in 2+ valence state. However, this result is in contradiction with the argument in last paragraph. One may suggest that lead could have both 2+ and 4+ states in this system. If this was the case, since the Pb (IV) shift is noticeable different to Pb (II), we should be able to observe another resonance at around 104.8 MHz. However we have not observed any other resonances in the frequency range of 103.55 MHz to 105.5 MHz.

Actually, the shift stated in the reference book<sup>21</sup> is the shift in liquid, *i.e.* this shift is chemical shift caused mainly by orbital interactions, not Knight shift. As we have analysed in the first paragraph of this section, lead in this system has to be in the 4+ valence state. Therefore, the +0.5% in shift of Pb (IV) becomes zero of Knight shift, *i.e.* Knight shift of lead in this system are varying from -0.22% to -0.37% as yttrium concentration changes.

If lead or thallium is in a fixed valence state, there should be no conducting electrons overlapping the sites. Thus, lead or thallium ions should have a fixed shift, *i.e.* the shift should not change as yttrium concentration changes, with no Knight shift. Then, why do we obtain a Knight shift from lead measurements and why does it change with yttrium concentration? We can find the answer from next section.

## § 6.7 One Component Model

For all High- $T_c$  cuprate superconductors, there are  $\text{CuO}_2$  "planes" which have been believed to be the locus of superconductivity. The crucial issue for normal state is the nature of the charge and spin degrees of freedom. Initially, this issue was often debated in terms of two pictures *i.e.* "one component"<sup>22</sup> and "two component"<sup>23</sup>. However, more and more scientists now believe the one component picture advanced by Millis, *et. al.*<sup>24</sup>, Monien *et. al.*<sup>25</sup>, Pennington *et. al.*<sup>26,27</sup>, Barrett *et. al.*<sup>28,29</sup>, and Bulut *et. al.*<sup>30,31,32</sup>. These authors have demonstrated that the temperature dependence of the Knight shift can be plotted as a universal curve for  $^{63}\text{Cu}(2)$ ,  $^{17}\text{O}(2,3)$  and  $^{89}\text{Y}$  Knight shift in YBCO system, thus demonstrating that all hyperfine interactions of these nuclei are caused by the same type of electron spins, which was termed a single spin fluid model (*i.e. the one component model*). This behaviour has also been verified by Brinkmann group<sup>33,34</sup>.

Mehring<sup>35</sup> has concluded that the hyperfine interaction Hamiltonians not only on copper, oxygen (in  $\text{CuO}_2$  plane) and yttrium nuclear sites but also the  $\text{Cu}(1)$  in YBCO and  $\text{Tl}(\text{Pb})$  in a  $\text{Tl}(\text{Pb})\text{O}$  layer compounds can be written in a similar form with different coupling constant but the same spin source.

We do not have the temperature dependence of  $^{63}\text{Cu}$  shifts and  $^{207}\text{Pb}$  shifts to analyse data as other groups did, *e.g.* Brinkmann group<sup>33,34</sup>, Takigawa group<sup>36</sup>, and Dupree group<sup>37,38</sup> *etc.* We can perform a similar analysis to ascertain whether there is a direct correlation between the room temperature shift results for the  $^{63}\text{Cu}$ ,  $^{89}\text{Y}$ , and  $^{207}\text{Pb}$  nuclei as a function of  $y$ , the yttrium concentration, in the  $\text{Tl}-1212$  system.

Figure 6.17 shows a plot of the room temperature  $^{89}\text{Y}$  isotropic Knight shift against the room temperature  $^{63}\text{Cu}$  isotropic Knight shift, with the implicit variation of yttrium concentration. Clearly, there is an approximately linear relation between the  $^{89}\text{Y}$  isotropic Knight shift and  $^{63}\text{Cu}$  isotropic Knight shift.

Figure 6.18 shows a plot of the room temperature  $^{207}\text{Pb}$  Knight shift against the room temperature  $^{63}\text{Cu}$  isotropic Knight shift, with the implicit variation of yttrium concentration. The  $^{207}\text{Pb}$  Knight shift is corresponding to the random powder spectral lineshape and has been subtracted 0.5%, the chemical shift, (see last section). Clearly, there is also an approximately linear relation between the  $^{207}\text{Pb}$  Knight shift and  $^{63}\text{Cu}$  isotropic Knight shift.

Both  $^{89}\text{Y}$  shift and  $^{207}\text{Pb}$  shift having the linear relation with  $^{63}\text{Cu}$  shift leads us to suppose that the one component model also applies in the Tl-1212 system, at least at room temperature.

Moving on to consider why  $^{207}\text{Pb}$  shifts in the Tl-1212 system change with yttrium concentration varying, according to the one component spin fluid theory, although it has a fix valence state in Tl(Pb)O plane, it has a transferred hyperfine interaction with copper in the Cu-O plane mediated by the bridging oxygen (O3, see Figure 4.2a). Therefore, we can observe a Knight shift on the lead site and the shifts also change when the spin susceptibility changes on copper site.

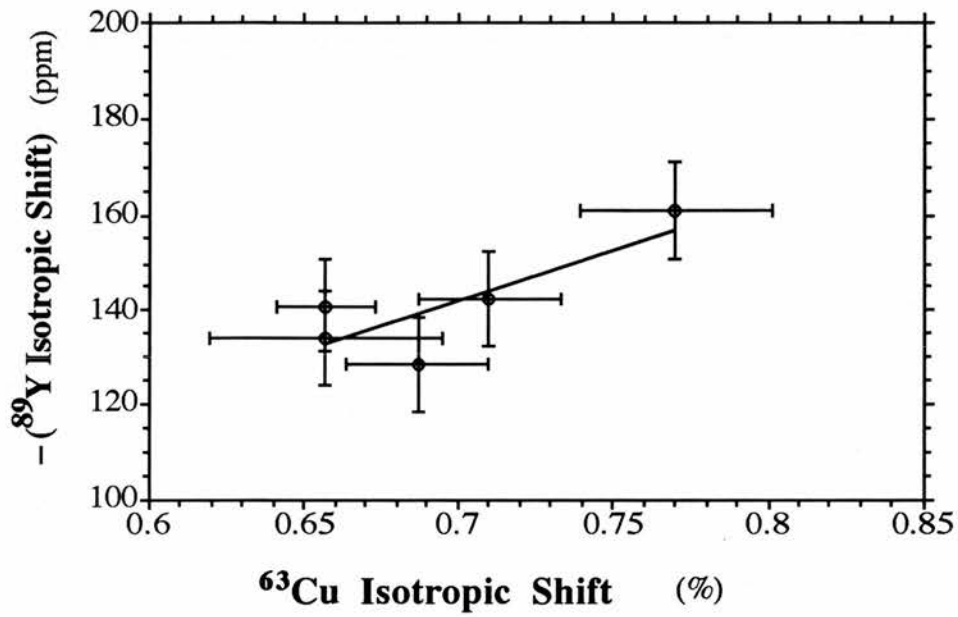


Figure 6.17 Correlation of  $^{89}\text{Y}$  shift with  $^{63}\text{Cu}$  shift at room temperature, with yttrium concentration as the implicit variable.

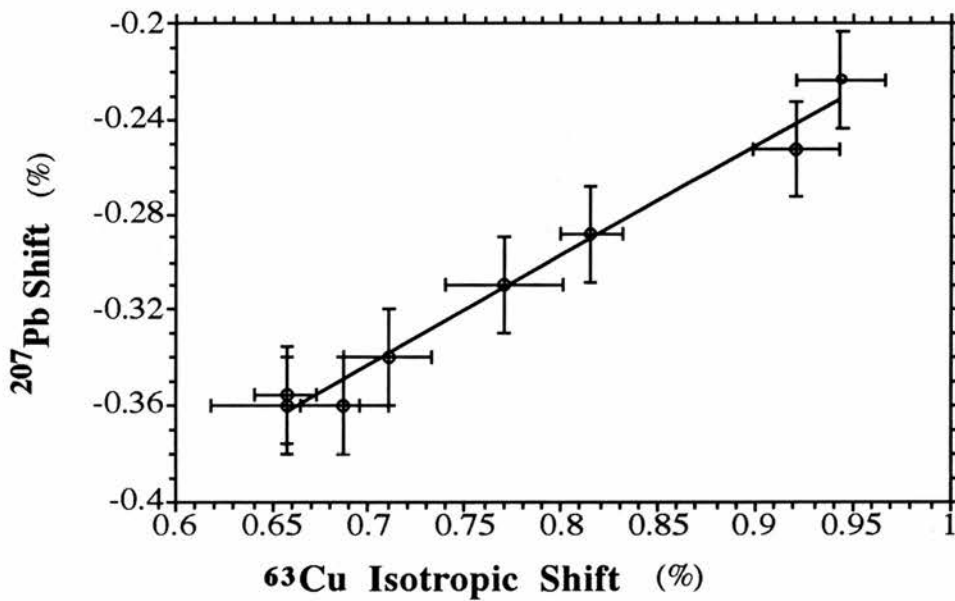


Figure 6.18 Correlation of  $^{207}\text{Pb}$  shift with  $^{63}\text{Cu}$  shift at room temperature, with yttrium concentration as the implicit variable.

## § 6.8 Spin-spin Relaxation time $T_2$

The spin-spin relaxation times,  $T_2$ , have been measured on the nuclei of copper and lead at room temperature shown in § 5.5.3 and § 5.6.2, respectively. The behaviours of the spin-spin relaxation of this two nuclei are quite different. There are three differences: (i) the time dependences of the signal intensities, the relaxations of all the copper nuclei in this system, are exponential. All the lead decays are rather Gaussian see Figures 5.23 and 5.30, respectively, (ii)  $T_2$ 's of copper nuclei (Figure 5.24) are much shorter than those of lead (Figure 5.31), (iii) the yttrium concentration dependences of the  $T_2$ 's of these two nuclei are different; the function for copper nuclei is linear but that for lead is a parabola, shown in Figures 5.24 and 5.31, respectively.

Pennington *et al*<sup>26</sup> have reported the transverse NMR relaxation of chain [Cu(1)] and plane [Cu(2)] nuclei in a single crystal of  $YBa_2Cu_3O_{7-\delta}$  ( $T_c = 90$  K) in the normal state. They have demonstrated the existence of a strong indirect spin-spin coupling between Cu(2) nuclei, and shown that it can be explained using a model in which the Cu(2) atoms possess electronic magnetic moments which are exchange coupled to one another. They calculate out that the effective coupling constant,  $J_{\text{eff}}$ , as about  $1100 \text{ cm}^{-1}$ .

For checking and comparison, we also did transverse relaxation time measurements on YBCO (the same sample on which we measured the copper shifts § 6.5.4). Figure 6.17 shows one of the measurements at room temperature and 134.2 MHz at which the resonance for Cu(2) and with c-axis parallel to  $\mathbf{B}$ , the magnetic field. In this figure, the solid line is a fitted line. However, it neither simply fitted the exponential function (see *equation (5.10)*), nor fitted the Gaussian function (see *equation (5.11)*). It can be described by a function as:

$$S = S_0 \exp \left[ - \left( \frac{2\tau}{T_{2L}} \right) - \frac{1}{2} \left( \frac{2\tau}{T_{2G}} \right)^2 \right] \quad (6.12)$$

where  $T_{2L}$  and  $T_{2G}$  are time constants for Lorentzian and Gaussian parts of the relaxation. Using this equation to fit the curve in Figure 6.19, the computer gives us the parameters  $S_0$ ,  $T_{2L}$  and  $T_{2G}$ . The values of  $T_{2L}$  and  $T_{2G}$  are  $118 \pm 5 \mu\text{s}$  and  $172 \pm 5 \mu\text{s}$ , respectively. These values are in good agreement with the results of Song and Halperin<sup>39</sup>. Both references 22 and 23 have demonstrated that in this case, the  $T_{2L}$  is caused by spin-lattice relaxation via Redfield theory<sup>40</sup>, denoted as a time constant,  $T_{2R}$ .

We are unable to calculate out the time constant  $T_{2R}$  for either copper nuclei or lead nuclei in the Tl system, since we do not have values of the spin-lattice relaxation time for them. However, analysing the data of lead NMR  $T_2$  measurements in Tl-1212 system, since there is no exponential component, if as Pennington *et. al.*<sup>26</sup> point out, spin-lattice relaxation leads to an exponential decay, the Redfield effect on lead must be very small, *i.e.*  $T_{2R}$  is large compared with  $T_{2G}$  caused by spin-spin coupling. We have noticed that the copper decay function has no Gaussian component. From the experimental data, we cannot obtain the components of  $T_{2R}$  and  $T_{2L}$  which is caused by spin-spin coupling.

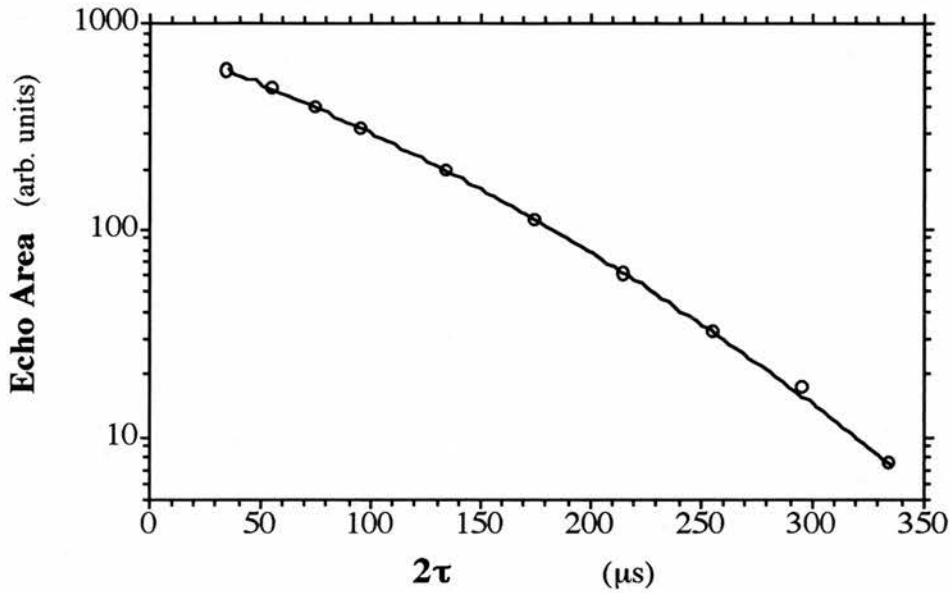


Figure 6.19 *Spin-spin relaxation time of copper-63 NMR measurement of YBCO sample at room temperature and 134.2 MHz at which the resonance for Cu(2) and with c-axis parallel to  $\mathbf{B}$ , the magnetic field.*

## § 6.9 Defect Model

Over all in view our experiments results, we found that we could detect signals neither on the  $y = 0.9$  and  $1.0$  samples for yttrium NMR, lead NMR, and copper NMR at room temperature nor the thallium NMR in the  $y > 0.3$  range of yttrium concentration at low temperature  $1.5$  K. We have investigated the sample of  $y = 0.9$  by yttrium NMR and obtained a Néel temperature of about  $340$  K. We suggest that if a sample is in antiferromagnetic state, we would not be able to observe any NMR signal. If this is the case, we then can think that we are unable to detect the thallium NMR in the  $y > 0.5$

range of yttrium concentration, because they are in an antiferromagnetic state at this temperature (1.5 K). We can therefore say that the Neel temperatures for these samples ( $0.6 \leq y \leq 0.8$ ) are in between 1.5 K and 160 K, since we do observe yttrium NMR signals at 160 K. However, this cause would be unlikely as an explanation of the absence of thallium NMR from  $y = 0.4$  and  $y = 0.5$ , since these samples are in superconducting state. Moreover, we must also consider the progressive reduction in copper and lead NMR intensity, as measured by the integrated area of copper, lead resonances, respectively, as a function of  $y$ .

Here, we can attempt to explain the progressive reduction of copper NMR intensity on a microscopic model where, unless a copper nucleus has the four neighbouring yttrium/calcium sites occupied by at most one yttrium ion, the copper resonance is wiped-out. We have included such a theoretical model in Figure 6.20, where the experimental data is taken from our Cu NMR on CRY\* ( $0 \leq y \leq 0.7$ ) series measurements, the solid line is of  $f(x) = nC_x p^x q^{n-x}$ ,  $p$  is the yttrium fraction,  $q$  is the calcium fraction,  $C$  is a binomial coefficient, and  $n = 4$ , the number of near-neighbour yttrium/calcium sites to a typical copper site.  $f(0) + f(1)$  therefore represents the probability of, at most, one yttrium occupying one of the four available neighbouring site.

Although no detailed one-to-one correspondence can be established on the basis of our data, there appears to be support here for a model whereby particular local combinations of yttrium/calcium substitution on yttrium sites both wipes out the NMR from the adjacent copper spins and creates a void in the superconducting network (see § 5.2). This is reminiscent of the sensitivity of the superconducting fraction in lithium titanate to the stoichiometry of the lithium concentration<sup>41</sup>.

The fact that we cannot see any thallium resonance above  $y = 0.3$  leads us to suppose that the origin of problem might be magnetic, *i.e.* the presence of two yttrium, say, in the nearest neighbour group of four yttrium/calcium sites to a particular copper, leads to a local magnetic moment, wiping out the thallium, lead and copper resonances.

On the basis of our data we suggest that the introduction of yttrium for calcium introduces electronic disorder, which wipes out superconductivity (and probably metallic character) from associated fractions of the material. This disorder has a related effect on copper NMR, probably because of associated quadrupolar effects. There may also be, associated with the disorder regions, magnetic localization, which destroys the thallium NMR at low temperature and lead NMR at room temperature.

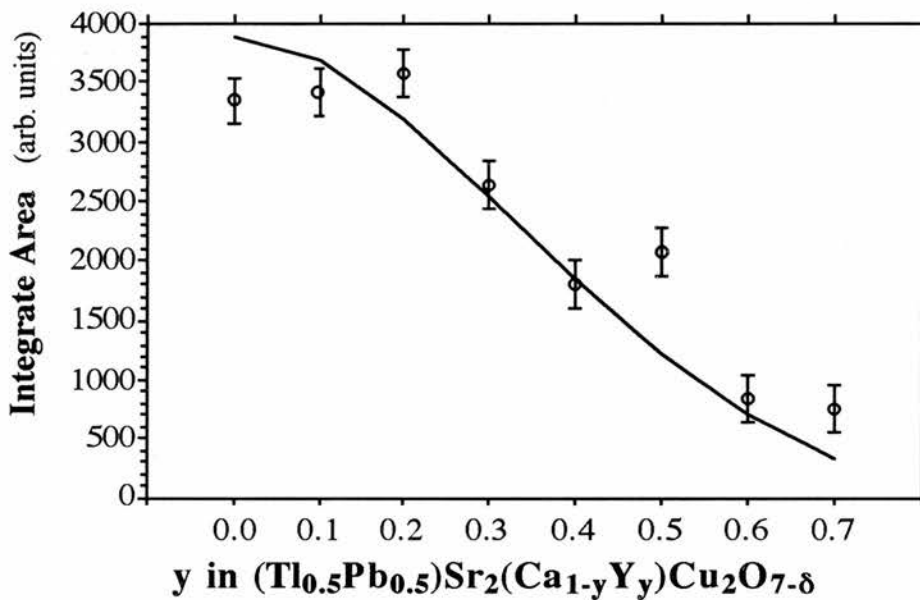


Figure 6.20 The integrated area of the copper spectra (on CRY\* series samples), in  $(\text{Tl}_{0.5}\text{Pb}_{0.5})\text{Sr}_2(\text{Y}_y\text{Ca}_{1-y})\text{Cu}_2\text{O}_{7-\delta}$ , plotted against  $y$  (the data points with integral error bars). Also plotted are the theoretical points (solid line) that emerge from a simple defect model for copper 'wipe-out' (see text).

## References

- 1 Muller K.A., and Bednorz J.G., *Science* **237**, 1133 (1987).
- 2 Farrell D.E., Chandrasekhar B.S., DeGuire M.R., Fang M.M., Kogan V.G., Clem J.R., and Finnemore D.K., *Phys. Rev. B* **36** 4025 (1987).
- 3 Fukuda K., Shamoto S., Sato M., and Oka K., *Solid State Commun.* **65**, 1323 (1988).
- 4 Lusnikov A., Miller L.L., McCallum R.W., and Mitra S., *J. Appl. Phys.* **65**, 3136 (1989)
- 5 Webster W.J., *PhD Thesis*, University of St. Andrews, UK (1993).
- 6 Song Y.-Q., Lee M., Halperin W.P., Tonge L.M., and Marks T.J., *Phys. Rev. B* **44**, 914 (1991).
- 7 Poddar A., Mandal P., Ray K.G., Das A.N., Ghosh B., Choudhury P., and Lahiri S.K., *Physica C* **159** 226 (1989).
- 8 (a) Mehring M., Hentsch F., Mattausch Hj., and Simon A., *Z. Phys.B-condensed Matter* **77**, 355 (1989).  
 (b) Hentsch F., Winzek N., Mehring M., Mattausch Hj., and Simon A., *Physica C* **158** 137 (1989).  
 (c) Hentsch F., Winzek N., Mehring M., Mattausch Hj., Simon A., and Kremer R., *Physica C* **165** 485 (1990).  
 (d) Winzek N., Hentsch F., Mehring M., Mattausch Hj., Kremer R., and Simon A., *Physica C* **168** 327 (1990).  
 (e) Winzek N., and Mehring M., *Appl. Magn. Reson.* **3**, 535 (1992).
- 9 Rajarajan A.K., Gopalakrishnan K.V., Vijayaraghavan R., and Gupta L.C., *Solid State Commun.* **69**, 213 (1989)

- 10 Fujiwara K., Kitaoka Y., Asayama K., Katayama-Yoshida H., Okabe Y., and Takahashi T., *J. Phys. Soc. Jpn.* **57**, 2893 (1999)
- 11 Kitaoka Y., Ishida K., Ohsugi S., Fujiwara K., Zheng G.-q. and Asayama K., *Appl. Magn. Reson.* **3**, 549 (1992).
- 12 Brom H.B., Moonen J.T., and Reefman D., *Appl. Magn. Reson.* **3**, 597 (1992).
- 13 Pincus P., Gossard A.C., Jaccarino V. and Wernick J.H., *Phys. Lett.* **13** 21 (1964)
- 14 Markert J.T., Dalichaouch, and Maple M.B., in *Physical Properties of High Temperature Superconductors Vol I*, Ed. Ginsberg D.M., World Scientific, Singapore, (1989).
- 15 Webster W.J., *PhD Thesis*, University of St. Andrews, UK (1993)
- 16 (a) Allol H., Mendels P., Collin G., and Monod P., *Phys. Rev. Lett.* **61** 746 (1988)  
 (b) Allol H., Ohno T., and Mendels P., *Phys. Rev. Lett.* **63** 1700 (1989)
- 17 Mila F., and Rice T.M., *Physica C* **157**, 561 (1989).
- 18 Yu J, Freeman A J, Podloucky R, Herzig P, and Weinberger P *Phys. Rev.* **B 43** 532 (1991)
- 19 Takigawa M., Hammel P.C., Heffner R H, Fisk Z., Smith J.L., and Schwarz R.B., *Phys. Rev.* **B 39** 300 (1989).
- 20 Brinkmann D., *Z. Naturforsch* **45 a** 393 (1990).
- 21 Brevard C., and Granger P., "Handbook of High Resolution Multinuclear NMR" A Wiley-Interscience Pul. p208 (1981)
- 22 In a one component picture, one thinks of the electron spins in Cu d orbitals and holes on the sublattice of planar oxygen p orbitals as being in some way hybridized into a single system.

- 23 In a two component picture, one thinks of these two subsystems are relatively independent.
- 24 Millis A.J., Monien H., and Pines D., *Phys. Rev. B* **42** 167 (1990)
- 25 Monien H., and Pines D., and Takigawa M., *Phys. Rev. B* **43** 258 (1991)
- 26 Pennington C. H., Durand D. J., Slichter C. P., Rice J. P., Bukowski E. D., and Ginsberg D. M., *Phys. Rev. B* **39** 274 (1989).
- 27 Pennington C. H., Durand D. J., Slichter C. P., Rice J. P., Bukowski E. D., and Ginsberg D. M., *Phys. Rev. B* **39** 2902(1989).
- 28 Barrett S.E., Durand D. J., Pennington C. H., Slichter C. P., Friedmann T.A., Rice J. P., and Ginsberg D. M., *Phys. Rev. B* **41** 6283(1990)
- 29 Barrett S.E., Martindale J.A., Durand D. J., Pennington C. H., Slichter C. P., Friedmann T.A., Rice J. P., and Ginsberg D. M., *Phys, Rev. Lett.* **66** 108 (1991)
- 30 Bulut N., Hone D., Scalapino D.J., Bickers N.E., *Phys, Rev. Lett.* **64** 2723 (1990)
- 31 Bulut N., Scalapino D.J., *Phys, Rev. Lett.* **67** 2898 (1991)
- 32 Bulut N., Scalapino D.J., *Phys, Rev. Lett.* **68** 706 (1992)
- 33 Zimmerman H., Mali M., Roos R., Brinkmann D., Karpinski J., Kaldis E., and Rusiecki S., *Physca C* **159** 681 (1989)
- 34 Mali M., Mangelschots I., Zimmerman H., and Brinkmann D., *Physca C* **158** 137 (1989), & *Physca C* **175** 581 (1991)
- 35 Mehring M., *Appl. Magn. Reson.*, **3** 383 (1992).
- 36 Takigawa M., Reyes A.P., Hammel P.C., Thompson J.D. Heffner R H, Fisk Z., and Ott K.C., *Phys. Rev. B* **43** 247 (1991).

- 37 Dupree R., Han Z.P., McK.Paul D., Babu T.G.N., and Greaves C., *Physica C* **179** 311 (1991)
- 38 Dupree R., and Han Z.P., *Modern Physics Letters B*, **6** 1765 (1992)
- 39 Song Y.-Q., and Halperin W.P., *Physica C* **191** 131 (1992)
- 40 Slichter C.P. *Principles of Magnetic Resonance*, 2nd ed. (Springer, Berlin, 1980).
- 41 Itoh M., Hasegawa Y., Yasuoka H., Ueda Y., and Kosuge K., *Physica C* **157** 65 (1989).

## Chapter 7

# Conclusions

### § 7.1 Summary and Conclusions

In this thesis, we report measurements of nuclear magnetic resonance (NMR) in the  $(\text{Tl}_{0.5}\text{Pb}_{0.5})\text{Sr}_2(\text{Y}_y\text{Ca}_{1-y})\text{Cu}_2\text{O}_{7-\delta}$  system as a function of  $y$ , the yttrium concentration, over the stoichiometry range encompassing the metal-superconductor-(antiferromagnetic) semiconductor transition. The powder samples were partially aligned, and the measurements included a systematic study of yttrium-89 shifts, and some relaxation data, in the temperature range 160 K to 300 K, room temperature copper-63 NMR and NQR and lead-207 NMR, as well as thallium NMR at 1.5 K. We have also carried out AC susceptibility and X-ray measurements to provide information on the electric structure, phase purity and degree of alignment of the cuprates.

Since these materials are highly magnetically anisotropic, it is useful to investigate the anisotropic properties of these materials. Although we do not have large single crystals for these experiments (it is always very difficult to grow large enough single crystals for NMR experiments, and also there is an r.f. penetration problem with single crystals), a useful method is to align the powders in a strong magnetic field. Most of our NMR experiments are performed on aligned powder samples. Although the alignment of our samples is not perfect (less than half of the powders are aligned), we still obtain quite useful information on these partially aligned powder samples, in particular, the copper NMR.

The results of  $^{63}\text{Cu}$  NMR are reported in § 5.5. Initially, we obtained the copper NMR spin echo spectra on partially aligned samples (the NCAY\* series). However, the spectra show hardly any orientation dependence, since the partially aligned samples contain too large an unoriented fraction. To observe the orientation dependence of the aligned fraction, we subtract the random fraction from the total spectra, and obtain clear orientation dependent spectra. One should point out here that we could not detect a copper spin echo signal on the samples of  $y=0.9$  and  $1.0$ , and since the signal to noise ratio was very poor for the sample  $y=0.8$ , we did not do the orientation spectra on these samples.

In § 6.5, we analyze the copper NMR results. After using the theory to fit the experimental data, we obtain the parameters, such as the isotropic Knight shift, the axial Knight shift, the  $c$ -axis parallel and perpendicular to magnetic field shift components, and the quadrupole resonance frequency.

Two experiments have been done which prove our results are very reliable. One is the copper NQR on the sample of  $y=0.0$ . We obtain a quadrupole resonance frequency of this sample around 21 MHz which is in a very good agreement with the result obtained from copper NMR experiments (20.9MHz). The other one is that we repeated the same experiments under the same conditions on the YBCO sample. We obtain a quadrupole resonance frequency of 31.0 MHz, which is in a very good agreement with the NQR experimental measurement result (31.2 MHz), and the Knight shift components also agree well with the results obtained by other groups.

Plotting the Knight shift components against  $y$ , yttrium concentration, we find that the isotropic shift component decreases with  $y$  increasing in the metallic region, while the axial shift component is almost a constant. This indicates that the substitution of calcium by yttrium only varies the isotropic part of the total magnetic shift. We argue that the variation of the transferred hyperfine interaction is the only origin of the isotropic shift variation and the spin susceptibility is constant over the composition range.

If we compare the copper NMR and NQR results between the Tl-1212 system and YBCO, we note that the Knight shifts for the two systems are in the same range while the quadrupole resonance frequencies are significantly different, being around 21 MHz for Tl-samples and about 31 MHz for YBCO. Comparing the two systems, the hole concentration on the Cu-O plane is different between the two systems, about one hole per unit cell for YBCO, less than half a hole per unit cell for the Tl system. Therefore, the differences of the hole concentration on CuO<sub>2</sub> plane of course will lead to a redistribution of electron populations around 'semi-core' copper states which cause the difference of the quadrupole constant.

The copper NMR linewidth is about three times broader, and the NQR linewidth is almost 10 times broader, in the Tl system than in the YBCO. There are two possible reasons for these descriptions: (i) structural disorder might be the first reason which causes the spectra to broaden. (ii) the smaller hole concentration might lead to stronger antiferromagnetic correlation which also can cause the spectra to broaden. A strong magnetic field would suppress both of these effects, so that the NMR spectra would be expected to be less broad than the NQR spectra.

From the yttrium NMR experiments, we learnt that the samples for  $y = 0.9$  and  $1.0$  are in antiferromagnetic states. We have one measurement of  $T_N$ , the Néel temperature, in  $y = 0.9$ , of  $350 \text{ K} \pm 10 \text{ K}$ . The evidence on this sample is that antiferromagnetism broadens the yttrium resonance beyond observability within a few degrees of the transition. We observe similar yttrium spectra over the range of samples, from  $y = 0.2$  to  $0.8$ ; for  $c$  parallel to  $\mathbf{B}$  we detect a doublet and for  $c$  perpendicular to  $\mathbf{B}$  just a single line. From a series rotation experiment, we identify it with the random powder element of the sample, and it is thus dominated by the contribution from those crystallites with  $c$  perpendicular to  $\mathbf{B}$ .

Having found that the line width of the Tl-1212 system is broader than those of the YBCO system, while the Knight shift of the Tl-1212 system is smaller than those of

YBCO system, this appears to correlate with the detailed crystal structure differences, as revealed by neutron diffraction. We found that the distance between yttrium and oxygen, which lies on Cu-O plane, is larger in thallium system than in YBCO; conversely, the distance between yttrium and Cu-O plane is smaller in the thallium system than in YBCO. The yttrium is closer to the oxygen site in YBCO, which may lead to larger yttrium Knight shifts, because yttrium couples with oxygen more strongly. Because there is an anti-ferromagnetic correlation in the Cu-O plane, the result of yttrium being nearer to the Cu-O plane in thallium materials may cause a broader line width.

In § 5.6, we report  $^{207}\text{Pb}$  NMR results. Through the orientation dependence measurements on NCAY0 ( $y = 0.0$ ) sample, a negative axial shift is observed, while a positive shift is detected with reference to a  $(\text{Pb}(\text{NO}_3)_2)$  solution. Since the samples contain a random fraction, we attempted to subtracted the random fraction following the deconvolution method as we did on  $^{63}\text{Cu}$  NMR. However, no worthwhile spectra can be obtained. The reason for this failure is that the spectra have too small an angular dependence compared with the spectral width; after subtracting, experimental error dominates the lineshapes.

The  $^{207}\text{Pb}$  NMR measurements on the random series samples (RCY\*) provided the resonance frequency and the integrated area of the spectra as a function of the yttrium concentration. The resonance frequency (or Knight shift) of the random sample is decreasing as  $y$ , the yttrium concentration, is increased in the metal region ( $0.0 \leq y \leq 0.5$ ). However, in the non-metal region ( $y \geq 0.6$ ), Knight shift is almost independent as  $y$  changes. The behaviour of the intensity of the integrated area of the spectrum as a function of  $y$  also can be classified into two groups, *i.e.* the metal region and the non-metal region. In both regions the intensity of the integrated area is decreasing as  $y$  is increased. However, it drops rapidly when the phase changes.

Referenced to  $(\text{Pb}(\text{NO}_3)_2)$  solution, the shifts of  $^{207}\text{Pb}$  in the random series samples are varying from +0.28% to +0.13% as the yttrium concentration changes.

Analysing the phase diagram (Figure 4.1), we deduce that lead should be in +4 valence state and therefore the  $\text{Pb}^{4+}$  should have a chemical shift about +0.5%. After subtracting the chemical shift, we derive the net Knight shifts for lead in this system are varying from -0.22% to -0.37% as the yttrium concentration increases.

Thallium NMR measurement is our sole NMR experiment at superconducting state (at 1.5 K) on this system. At such low temperature, there is a considerable breadth to the lines, about 0.3 to 0.4 Tesla.

Our thallium NMR linewidths can be interpreted as due to the flux line lattice, for  $y = 0.0, 0.1, 0.2, 0.3$  the penetration depth is about  $800 \pm 200 \text{ \AA}$ . There is no marked variation of the Tl resonance width with yttrium concentration; the penetration depth must be changing very little in the range of yttrium concentration for which we observe the Tl resonance at the low temperature. We cannot observe any thallium resonance signal above  $y = 0.3$ .

The non-observability of Tl resonance in the  $y > 0.5$  range of concentration we ascribed initially to the anti-ferromagnetic polarization of these samples. The Tl is in a lattice position where the magnetic fields from neighbouring antiferromagnetically aligned copper spins do not cancel each other out; the Tl resonance is shifted drastically. Whilst antiferromagnetism can be invoked to explain the absence at 1.5 K of thallium NMR for  $y > 0.5$ , this cause would be unlikely as an explanation of the absence of thallium NMR from  $y = 0.4$  and  $y = 0.5$  since both of them are at superconducting state. The lack of thallium NMR signal for all samples with  $y > 0.3$  at 1.5 K may be related to the fall-off in copper NMR intensity at room temperature explained by the yttrium/calcium defect model (see § 6.9).

In this research, we mainly concentrated on the NMR shifts measurement. Since it is also useful to obtain dynamic NMR measurements (*i.e.* relaxation times:  $T_1$ , spin-lattice relaxation and  $T_2$ , spin-spin relaxation measurements). We have attempted to

measure  $T_1$  at room temperature of both copper and lead nuclei. Unfortunately, we could not obtain worthwhile value of  $T_1$  on either nuclei, since our fastest repetition period is 5 milliseconds, and down to this value the spectra are all the same. Therefore, we could only conclude that the  $T_1$ 's of both copper-63 and lead-207 nuclei in this system at room temperature are shorter than milliseconds.

We have measured the spin-spin relaxation time,  $T_2$ , on the nuclei of copper and lead at room temperature shown in § 5.5.3 and § 5.6.3, respectively. The behaviours of the spin-spin relaxations of these two nuclei are quite different. We have found that there are three major differences. (i) The time dependences of the signal intensities. The relaxations of all the copper nuclei in this system are exponential. All the lead decays are rather Gaussian. (ii)  $T_2$ 's of copper nuclei are much shorter than those of lead. The value of  $T_2$  of copper-63 nuclei is varying from 60  $\mu\text{s}$  to 20  $\mu\text{s}$  as  $y$ , yttrium concentration, changes from 0.0 to 0.8, while the value of  $T_2$  of lead-207 nuclei is varying from 350  $\mu\text{s}$  to 100  $\mu\text{s}$ . (iii) The yttrium concentration dependences of  $T_2$ 's of these two nuclei are different. The function for copper nuclei is linear but that for lead is parabola.

There is approximately linear relation between the  $^{89}\text{Y}$  isotropic Knight shift and  $^{63}\text{Cu}$  isotropic Knight shift and between the  $^{207}\text{Pb}$  Knight shift and  $^{63}\text{Cu}$  isotropic Knight shift with the implicit variation of yttrium concentration.

The fact that both  $^{89}\text{Y}$  shift and  $^{207}\text{Pb}$  shift have a linear relation with  $^{63}\text{Cu}$  shift leads us to suppose that the single spin fluid model (*i.e. the one component model*) also applies in the Tl-1212 system, at least at room temperature.

Summarizing, we found that not only we could not detect signals neither on the  $y = 0.9$  and  $1.0$  samples for yttrium NMR, lead NMR, and copper NMR at room temperature nor the thallium NMR in the  $y > 0.3$  range of yttrium concentration at low temperature 1.5 K, but also the intensities of copper NMR and lead NMR and the superconducting fraction decrease with yttrium concentration increases.

We develop a microscopic model where, unless a copper nucleus has the four neighbouring yttrium/calcium sites occupied by at most one yttrium ion, the copper resonance is wiped-out. Although no detailed one-to-one correspondence can be established on the basis of our data, there appears to be support here for a model whereby particular local combinations of yttrium/calcium substitution on yttrium sites both wipes out the NMR from the adjacent copper spins and creates a void in the superconducting network.

On the basis of our data we suggest that the introduction of yttrium for calcium introduces electronic disorder, which wipes out superconductivity (and probably metallic character) from associated fractions of the material. This disorder has a related effect on copper NMR, probably because of associated quadrupolar effects. There may also be, associated with the disorder regions, magnetic localization, which destroys the thallium NMR at low temperature and lead NMR at room temperature.

## § 7.2 Suggestions for Further Work

To further confirm the one component model on this system, the shifts of both copper and lead NMR of temperature dependence are useful parameters to be obtained from further work. The copper NMR and lead NMR experiments at 1.5 K are also important, since these experiments can provide the orbital shift component information, and therefore one can deduce the 'pure' Knight shift components.

It would be also useful to obtain the spin-lattice relaxation time as a function of temperature on copper and lead nuclei of this system.

For comparison, it would be interesting to do the same experiments on a  $(\text{Tl}_x\text{Pb}_{1-x})\text{Sr}_2(\text{Y}_{0.2}\text{Ca}_{0.8})\text{Cu}_2\text{O}_7$  system.

## Appendix

# Publications

### § A.1 Publications in Scientific Journals

- (1) D.P.Tunstall, **G.P.Dai**, W.J.Webster, H.Booth, S.Arumugam, R.-S.Liu, P.P.Edwards, A Thallium, Yttrium, Copper NMR Study of the  $(\text{Tl}_{0.5}\text{Pb}_{0.5})\text{Sr}_2(\text{Y}_y\text{Ca}_{1-y})\text{Cu}_2\text{O}_7$  System, *Superconductor Science and Technology* **6** 33 (1993)
- (2) **G.P.Dai**, D.P.Tunstall, W.J.Webster, H.Booth, S.Arumugam, R.-S.Liu, P.P.Edwards, Yttrium NMR Study in  $(\text{Tl}_{0.5}\text{Pb}_{0.5})\text{Sr}_2(\text{Y}_y\text{Ca}_{1-y})\text{Cu}_2\text{O}_7$  System, *Proceedings of the Beijing International Conference on High  $T_c$  Superconductivity (BHTSC'92)* Eds. by Z.Z. Gan, S.S. Xie and Z.X. Zhao, (World Scientific, Singapore) 461 (1993)
- (3) **G.P.Dai**, D.P.Tunstall, R.-S.Liu, P.P.Edwards, A Study of the Orientation Dependence of the  $^{63}\text{Cu}$  Nuclear Magnetic Resonance in The  $(\text{Tl}_{0.5}\text{Pb}_{0.5})\text{Sr}_2(\text{Ca}_{1-y}\text{Y}_y)\text{Cu}_2\text{O}_{7-\delta}$  System *Physica C* **220** 93 (1994)
- (4) **G.P. Dai**, B. Ctortecka, D.P. Tunstall, M. Jones, and P.P. Edwards,  $^{63}\text{Cu}$  NMR Study in the  $\text{Nd}_2\text{CuO}_{4-x}\text{F}_x$  System. submitted to *Solid State Communication* **91** 205 (1994).

- (5) **G.P.Dai**, D.P.Tunstall, R.-S.Liu, P.P.Edwards, The Pb Knight Shift, And Pb And Cu T<sub>2</sub>'s, Across The Compositional Range in The (Tl<sub>0.5</sub>Pb<sub>0.5</sub>) Sr<sub>2</sub>(Ca<sub>1-y</sub>Y<sub>y</sub>) Cu<sub>2</sub>O<sub>7-δ</sub> System (in process)
- (6) D.P.Tunstall, **G.P.Dai**, W.J.Webster, A Cu NQR Study Of The Co-Doped YBCO System. (in process)
- (7) **G.P. Dai**, B. Ctordecka , D.P. Tunstall, M. Jones, and P.P. Edwards, Evidence of No Electric Quadrupole Interactions From <sup>63</sup>Cu NMR Study in the Nd<sub>2</sub>CuO<sub>4-x</sub>F<sub>x</sub> System.(in process)
- (8) **G P Dai**, D P Tunstall, and P P Edwards, Copper-63 NMR study of YBa<sub>2</sub>Cu<sub>3</sub>O<sub>6.11</sub>F<sub>1</sub> & YBa<sub>2</sub>Cu<sub>3</sub>O<sub>6.11</sub>F<sub>2</sub> (in process)
- (9) D P Tunstall, J R M Todd, S Arumugam, **G P Dai**, M Dalton and P P Edwards, Titanium nuclear resonance in lithium titanate and its lithium substituted derivatives, Li<sub>1+x</sub>Ti<sub>2-x</sub>O<sub>4</sub> (0≤x≤0.1) (submitted to *Phys. Rev. B*)

## § A.2 Contributions to Scientific Meetings

- (1) **G P Dai**, and D P Tunstall, Cu Nuclear Resonance in the Septenary Cuprates, Solid State NMR New Materials & New Techniques, British Radiofrequency Spectroscopy Group & Royal Society of Chemistry NMR Discussion Group Meeting, University of Warwick, U. K., 5th-7th September, 1990.
- (2) **G P Dai**, and D P Tunstall, An Yttrium and Thallium NMR Study of the (Tl<sub>0.5</sub>Pb<sub>0.5</sub>)Sr<sub>2</sub>(Ca<sub>1-y</sub>Y<sub>y</sub>)Cu<sub>2</sub>O<sub>7-δ</sub> System, 39th Scottish Universities (NATO) Summer School on High Temperature Superconductivity-Materials, Mechanisms & Devices, University of St. Andrews, U. K., 16th-29th June, 1991.

(3) **G. P. Dai**, D. P. Tunstall, W. J. Webster, H. F. Booth, S. Arumugam, R. S. Liu & P. P. Edwards, Yttrium NMR Study of the  $(\text{Tl}_{0.5}\text{Pb}_{0.5})\text{Sr}_2(\text{Ca}_{1-y}\text{Y}_y)\text{Cu}_2\text{O}_{7-\delta}$  System, Beijing International Conference on High  $T_c$  Superconductivity (BHTSC '92), Beijing, China, 25th-29th May 1992. (Oral Presentation by **G. P. Dai**)

(4) **G. P. Dai**, D. P. Tunstall, W. J. Webster, H. F. Booth, S. Arumugam, R. S. Liu & P. P. Edwards, Copper NMR Study of the  $(\text{Tl}_{0.5}\text{Pb}_{0.5})\text{Sr}_2(\text{Ca}_{1-y}\text{Y}_y)\text{Cu}_2\text{O}_{7-\delta}$  System, British Radio-Spectroscopy Group Meeting, April, 1992, Nottingham

(5) **G. P. Dai**, D. P. Tunstall, R. S. Liu & P. P. Edwards,  $^{63}\text{Cu}$  NMR Orientation Dependence Study of the  $(\text{Tl}_{0.5}\text{Pb}_{0.5})\text{Sr}_2(\text{Ca}_{1-y}\text{Y}_y)\text{Cu}_2\text{O}_{7-\delta}$  System, Condensed Matter and Materials Physics, IOP, Sheffield, December 1992

(6) **G.P.Dai**, D.P.Tunstall, R.-S.Liu, P.P.Edwards, The Pb Knight Shift, And Pb And Cu  $T_2$ 's, Across The Compositional Range in The  $(\text{Tl}_{0.5}\text{Pb}_{0.5})\text{Sr}_2(\text{Ca}_{1-y}\text{Y}_y)\text{Cu}_2\text{O}_{7-\delta}$  System, British Radio-Spectroscopy Group Meeting, September, 1993, St. Andrews, Scotland

(7) **G.P. Dai**, B. Ctordecka, D.P. Tunstall, M. Jones, and P.P. Edwards,  $^{63}\text{Cu}$  NMR Study in the  $\text{Nd}_2\text{CuO}_{4-x}\text{F}_x$  System. Condensed Matter and Materials Physics, IOP, Leeds, Dec. 1993